POLITECNICO
MILANO 1863

SCHOOL OF INDUSTRIAL AND INFORMATION ENGINEERING
MASTER OF SCIENCE – AERONAUTICAL ENGINEERING

MID-FIDELITY MODELING OF THE AERO-PROPULSIVE INTERACTION FOR THE INITIAL DESIGN OF DISTRIBUTED PROPULSION AIRCRAFT

Master Thesis

Supervisor:
Prof. Lorenzo TRAINELLI

Co-supervisor:
Prof. Carlo E. D. RIBOLDI

Master of Science thesis of:
Andrea Roberto MORETTI – 940093

Academic Year 2021-2022

Abstract

This thesis presents the development of a mid-fidelity meta-model for the aero-propulsive interaction of distributed propulsion aircraft, which is suitable for preliminary aircraft sizing. The meta-model represents a generic and comprehensive approach able to provide meaningful information concerning aero-propulsive effects in the early phase of the design process. It aims to increment the accuracy of existing sizing routines without compromising their rapidity. The presented approach consists of running several mid-fidelity simulations of the aircraft wing blown by the distributed propulsion to construct multi-dimensional maps of parameters such as lift and drag increments. The sizing routine will subsequently interrogate the dataset without a noticeable increase in the sizing loop computational costs.

Vortex Lattice Method was the mid-fidelity tool selected to perform the numerical campaign. Concerning propeller modeling, the purely VLM approach, which implements the actual blade geometry, proved its superiority over the actuator disk approach, which cannot capture the complete coupling between the wing and the propellers. Apart from validation, carried out against experimental data, further studies analyzed the capability of the purely VLM approach to deal with setups featuring multiple, overlapping, or counter-rotating propellers.

UNIFIER19 configuration C7A-HARW is the reference aircraft selected for this work. The dimensional analysis of a generic force coefficient provided a consistent framework to construct the meta-model dataset. The design space covered by the multi-dimensional maps considers three parameters: the AoA, the propeller tilt, and the advance ratio. The final dataset, made of 216 data points divided into 36 raw data curves, generates nine sets of polars. The reduced approach, developed to lower the computational costs of the numerical campaign, proved its effectiveness by reducing the computational time by about 50% without compromising the accuracy.

The developed meta-model is successfully implemented in TITAN, a preliminary aircraft sizing routine of Politecnico di Milano. The newly implemented features are the computation of High Lift Propellers settings to obtain the desired lift augmentation and the estimation of corrected drag polars that considers the presence of the DEP system. The solution produced by the updated version of TITAN exhibits a Maximum Takeoff Mass increment of 1.7%, mainly related to the previously neglected drag contribution of the HLP nacelles.

Keywords: Vortex Lattice Method, Distributed Electric Propulsion, preliminary aircraft sizing, meta-model, aero-propulsive interaction.

Sintesi

In questa tesi viene presentato lo sviluppo di un meta-modello a media-fedeltà dell'interazione aero-propulsiva propria di velivoli con propulsione elettrica distribuita, adatto all'integrazione in una procedura per il dimensionamento preliminare. Il meta-modello rappresenta un approccio generale e completo in grado di fornire informazioni utili riguardo gli effetti aero-propulsivi nella fase iniziale del processo di progettazione. Esso ha l'obiettivo di incrementare l'accuratezza delle attuali procedure di dimensionamento senza comprometterne la rapidità. L'approccio presentato consiste nello svolgere anticipatamente le simulazioni sulla geometria soffiata, al fine di costruire mappe multidimensionali di parametri come gli incrementi di portanza e resistenza. La procedura di dimensionamento interrogherà semplicemente la base dati senza gravare sul costo computazionale del dimensionamento.

Per lo svolgimento della campagna numerica è stato scelto il metodo Vortex Lattice. Per quanto concerne la modellazione delle eliche, l'approccio VLM puro, che implementa la vera geometria delle pale, si è dimostrato superiore a quello con disco attuatore, che non ha invece saputo catturate l'accoppiamento tra ala ed elica. Oltre alla validazione con dati sperimentali, sono stati effettuati ulteriori studi volti ad analizzare la capacità dell'approccio prescelto di saper trattare geometrie con più eliche, anche sovrapposte o controrotanti.

La configurazione C7A-HARW di UNIFIER19 rappresenta la geometria di riferimento per questo lavoro. L'analisi dimensionale di un generico coefficiente di forza ha permesso di affrontare in maniera coerente la costruzione della base dati. Le coordinate che definiscono lo spazio di progetto sono: l'angolo d'incidenza, il rapporto di funzionamento dell'elica e la sua inclinazione rispetto all'ala. La base dati finale, costituita da 216 punti prova divisi in 36 curve grezze, ha permesso di generare nove set di polari. L'approccio ridotto si è dimostrato efficace nell'abbattere il costo computazionale della campagna numerica di circa il 50% senza comprometterne l'accuratezza.

Le nuove funzionalità implementate in TITAN, ossia la procedura per il dimensionamento preliminare di velivoli del Politecnico di Milano, permettono di calcolare le condizioni operative delle eliche che garantiscono l'aumento di portanza desiderato e di correggere le polari considerando la presenza del sistema DEP. La soluzione prodotta dalla versione aggiornata di TITAN mostra un incremento della massima massa al decollo dell'1.7%, principalmente dovuta al contributo di resistenza delle gondole motore, fino ad ora trascurato.

Parole chiave: Metodo Vortex Lattice, Propulsione Elettrica Distribuita, dimensionamento preliminare di velivoli, meta-modello, interazione aero-propulsiva.

Ringraziamenti

Prima di addentrarsi in questo elaborato, che rappresenta il coronamento di un percorso iniziato ormai più di cinque anni fa, con la consapevolezza che questo traguardo altro non sia che un nuovo inizio, ritengo doveroso ringraziare tutti coloro che mi hanno accompagnato in questo viaggio.

Innanzitutto, grazie al mio relatore, Professor Lorenzo Trainelli, ed al Professor Carlo E. D. Riboldi, non solo per avermi seguito durante l'attività di tesi, ma anche per la passione trasmessami durante i corsi tenuti negli anni precedenti. Un grazie anche a Yasir Khan per il suo supporto ed i suoi preziosi consigli.

A quei colleghi conosciuti negli anni, che oggi chiamo amici, sono grato per i bei momenti trascorsi assieme, che hanno tanto contribuito alla mia crescita, sia come ingegnere che come persona.

Un grazie poi agli amici di sempre ed a tutti i parenti; in particolar modo a mia nonna Agnese, che da quasi 25 anni mi sprona costantemente a dare il meglio, e a tutti gli altri nonni che purtroppo non potranno condividere con me la gioia di questo evento: Sara, Andrea e Roberto.

Un ringraziamento speciale va infine ai miei genitori, Morena e Gabriele, senza il cui instancabile e incondizionato supporto nulla di tutto ciò sarebbe mai stato possibile.

Table of Contents

List of Figures

List of Tables

List of Symbols and Acronyms

Symbols

α	Angle of Attack
α_g	Angle between airfoil reference frame and aircraft reference frame
$\hat{\alpha}_s$	Local stall AoA
α_t	Wing twist
α_0	Zero-lift AoA
$\beta_{3/4}$	Blade pitch at 75%R
Γ	Wing dihedral
δ_f	Flap deflection
$\Delta\alpha_0$	Deviation between numerical and experimental effective α_0
$\Delta\alpha_0^{off}$	Deviation between blown wing α_0^* and unblown wing α_0
ΔC_D	Drag coefficient increment
ΔC_L	Lift coefficient increment
ΔC_{L_α}	Deviation between numerical and experimental effective C_L
$\Delta C_{L_\alpha}^{off}$	Deviation between blown wing $C_{L_\alpha}^*$ and unblown wing C_{L_α}
$\Delta C_{L_{minC_D}}$	Deviation between numerical and experimental $C_{L_{minC_D^*}}^*$
$\Delta C_{L_{minC_D}}^{off}$	Deviation between blown wing $C_{L_{minC_D^*}}^*$ and unblown wing $C_{L_{minC_D}}$
$\Delta C_\ell / C_{\ell_u}$	Sectional lift coefficient relative increment
$\Delta minC_D$	Deviation between numerical and experimental effective $minC_D$
$\Delta minC_D^{off}$	Deviation between blown wing $minC_D^*$ and unblown wing $minC_D$
ΔC_{p_t}	Total pressure coefficient rise downstream the propeller
ΔK	Deviation between numerical and experimental effective K
ΔK^{off}	Deviation between blown wing K^* and unblown wing K

ϵ	Propeller tilt with respect to wing reference frame
$\hat{\epsilon}$	Local propeller tilt
η_p^{DEP}	DEP propulsive efficiency
λ	Wing taper ratio
Λ	Wing sweep
μ	Air dynamic viscosity
ρ	Air density
σ_{DEP}	DEP motors throttle parameter
a	Speed of sound
AR	Aspect ratio
c	Generic wing chord
$\bar{c}$	Mean aerodynamic chord
C_D	Drag coefficient
C_{D_0}	Parassite drag coefficient
C_F	Generic force coefficient
C_{F_x}	Force coefficient along x-wind axis
C_{F_z}	Force coefficient along z-wind axis
C_L	Lift coefficient
C_{L_α}	Lift curve slope
$C_{L_{max}}^{clean}$	Maximum lift coefficient for clean configuration
$C_{L_{minC_D}}$	Lift coefficient associated with the effective $minC_D$
$\widetilde{C_L^w}$	Reference lift coefficient of the wing
C_{L_u}	Unblown wing lift coefficient
C_P	Power coefficient ($P/\rho N^3 d^5$)
C_T	Thrust coefficient ($T/\rho N^2 d^4$)
d	Propeller diameter
D	Drag
e	Oswald factor
F_x	Force along x-wind axis
F_z	Force along z-wind axis
i_w	Wing root incident
J	Advance ratio (V/Nd)

k	Generic coefficient
K	Drag polar concavity
$minC_D$	Minimum drag coefficient
L	Lift
m	Generic coefficient
M	Mach number
M_{LH_2}	Mass of liquid hydrogen
M_{TO}	Maximum Takeoff Mass
n	Generic coefficient
n_p	Number of operating propellers
N	Propeller speed
P	Power
P_a	Available power
P_b	Shaft power
P_r	Required power
R	Propeller radius
Re	Reynolds number
r_h	Hub radius
r_p	Geometrical parameter ($d/\sqrt{S}$)
s_c	Sinnige's setup semispan
S	Wing surface
S_{blown}	Wing blown surface
t/c	Airfoil thickness ratio
T	Thrust
$P_{\%}^{DEP}$	Ratio of DEP available power over total required power
V	Airspeed
X	Generic coordinate along x-body axis
Y	Generic coordinate along y-body axis
$(\cdot)^{DEP}$	Referred to DEP system
$(\cdot)_i$	Referred to the i-th propeller
$(\cdot)_r$	Referred to wing root
$(\cdot)_t$	Referred to wing tip

$(\cdot)^{off}$	Referred to the prop-off case
$(\cdot)^{w}$	Wing contributions
$(\cdot)^{f}$	Fixed group contributions
$(\cdot)^{*}$	Effective quantities

Acronyms

AD	Actuator Disk
AoA	Angle of Attack
API	Application Programming Interface
AR	Aspect Ratio
BEMT	Blade Element Momentum Theory
BLI	Boundary-Layer Ingestion
CAD	Computer-Aided Design
CFD	Computational Fluid Dynamics
CRP	Counter-Rotating Propellers
CS	Certification Specifications
DEP	Distributed Electric Propulsion
DP	Distributed Propulsion
EAS	Essential Air Service
EM	Electric Motor
eVTOL	electric Vertical Take-Off and Landing
Exp	Experimental
GUI	Graphical User Interface
HARW	High Aspect Ratio Wing
HLD	High Lift Device
HLP	High Lift Propeller
IPC	Individual Propeller Contributions
LLM	Lifting Line Method
LLM	Lifting Line Theory
LND	Landing
MAC	Mean Aerodynamic Chord
MCP	Maximum Continuous Power
MM	Meta-Model

MPC	Multiple Propeller Case
MTOM	Maximum TakeOff Mass
MWP	Mid-Wing Propeller
NAC	Nacelle
NZE	Near-Zero-Emission
OEI	One Engine Inoperative
OPC	Overlapping Propeller Case
Patt	Patterson's method
PGS	Power Generation System
PVS	Pipistrel Vertical Solutions
RPM	Revolutions Per Minute
TO	TakeOff
UAV	Unmanned Aerial Vehicle
VLM	Vortex Lattice Method
WTP	Wingtip Propeller

Chapter 1

Introduction and Objective

In recent years, raising concerns about climate change are pushing toward more sustainable means of transport. In the aviation industry, several publicly funded projects, such as the NASA Advanced Air Transport Technology [1] or the European Clean Aviation program [2], are aiming to this target and promote research in this field.

Electric vehicles are a viable solution to reduce noise and air pollution in densely populated urban areas. However, the weight penalty associated with batteries still represents a significant limit to electric aircraft development. In this context, researchers are looking for strategies to counteract such drawbacks, taking advantage of the characteristics of an electric propulsion system compared to a traditional one. Distributed Electric Propulsion (DEP) is an example of this effort: thanks to electric motors scalability, the installed power can be separated into a large number of units, strategically placed to exploit positive aero-propulsive interactions.

1.1 DEP in general

Current DEP concepts implement many different layouts for the propulsion system, for example:

- **Boundary-Layer Ingestion**: ducted fans or pusher propellers generally installed on the tailcone or wing trailing edge; they are capable of lowering aerodynamic drag by extending downstream the laminar region in the boundary layer or reducing kinetic energy losses in the wake using wake filling.
- **Wingtip Propellers**: when spinning in the Inboard-Upward direction, their usage takes advantage of the wingtip vortices. Tractor configuration reduces lift-induced drag counteracting those vortices, while pusher configuration improves the propulsive efficiency increasing the tangential velocity at the propeller blades [3].
- **High Lift Propellers**: propellers installed on the wing leading edge used to produce a nearly uniform blowing spanwise. Increased dynamic pressure reduces stall speed and improves field performance. This configuration is complementary or alternative to conventional high lift devices; it enables high aspect ratio wing designs optimized for the cruise phase.

The present thesis primarily focuses on the most common and studied DEP layout: High Lift Propellers (HLP), extending the developed methodology to Wingtip propellers whenever possible.

Fig. 1.1 illustrates X-57 Maxwell, the DEP technical demonstrator realized by NASA in the context of the Scalable Convergent Electric Propulsion Technology Operations Research (SCEPTOR) project. This aircraft implements both wingtip cruise propellers and foldable blades high lift propellers. Fig. 1.2 represents the all-electric eVTOL concept developed by Lilium GmbH, equipped with BLI ducted fan arrays on both wing and canard.

Fig. 1.1: NASA X-57 Maxwell [4].

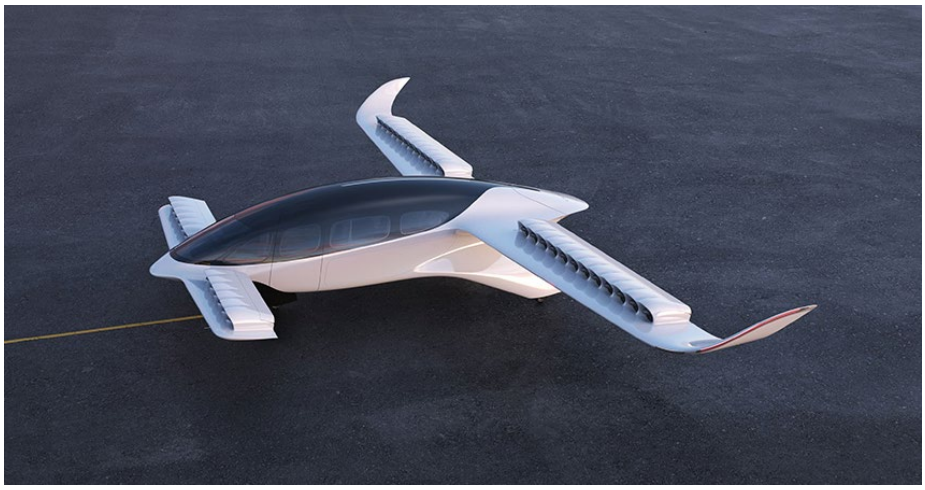

Fig. 1.2: Lilium air-taxi vehicle [5].

Early studies of some DP configurations, theorizing the benefits of interactions between the propellers and the airframe, date back to 1969 [6]. The complexity of effectively downscaling combustion engines, combined with the development of the more performant jet engines, led those projects to be put aside for several decades. Nowadays, however, electric motors may eventually represent DP enabling technology, and vice versa, these exotic designs could finally be capable of closing the performance gap currently existing between conventional and electric propulsion.

1.1.1 Electric motors advantages

The possibility to effectively generate the required power using multiple units instead of a single one without a significant weight penalty (i.e., scalability) is a characteristic of electric motors. Other advantages, well summarized by Patterson in [7], includes but are not limited to:

- Very high efficiencies (above 90%) over a wide range of operating conditions;
- Few moving parts, low vibration levels and noise, high reliability, and simple maintainability;
- No shaft power lapse with altitude or flight speed;
- The digital control signal is easily controllable via an autopilot;
- Compactness (i.e., higher power density compared to conventional engines);
- Synergy with renewable energy technologies can virtually eliminate system-level emissions.

1.1.2 Additional advantages of distributed propulsion

The primary goal of distributed propulsion is exploiting positive interactions between the propulsion system and the airframe, trying to improve the overall vehicle performance. Reducing energy consumption or shortening takeoff and landing distances are typical targets for distributed propulsion concepts.

Other advantages provided by DP, this time not related to performance, includes but are not limited to:

- A more even spanwise distribution of masses and loads on the wing;
- Additional control authority provided by the use of differential thrust;
- Lower impact of the OEI condition due to the high number of installed motors.

1.1.3 DEP aircraft application

Increased reliability, better field performance, and reduced carbon emissions are among the reasons behind DEP rising popularity. At the same time, the continuous technological progress in the electric propulsion field supports the development of novel concepts for a growing number of applications.

Patterson, in his 2016 dissertation [7], reported the following non-exhaustive list of missions that can benefit significantly from all-electric aircraft:

- Conventional general aviation (flight schools, leisure aviation, etc.);
- Essential Air Services (EAS) for small communities within the US;
- Delivery of goods directly to customers using UAVs;
- On-demand air transportation (Urban Air Mobility, air taxi, etc.).

Considering DP and powerplant hybridization, mitigating the disadvantages of an all-electric platform, these aircraft can perform many more tasks, not limited to short-range and short-endurance missions. Replacing larger aircraft in more traditional roles, like narrow-body airliners used for regional passenger or cargo transportation, is the objective of many DEP concepts. As an example of such designs, Fig. 1.3, taken from [8], illustrates the model of a large passenger aircraft featuring DEP in the form of multiple ducted fans.

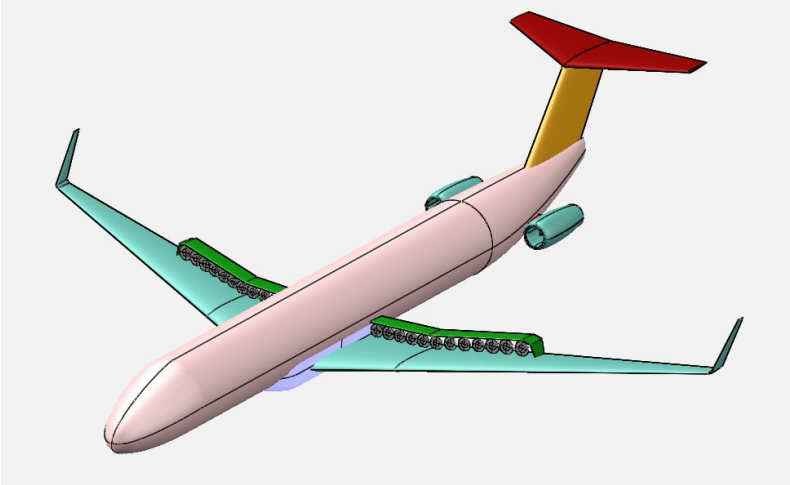

Fig. 1.3: OpenVSP [8] model of a large passenger aircraft concept with distributed electric ducted fans [9].

1.2 Aim and objectives

The target of the present thesis is the development of a meta-model for the aero-propulsive interaction typical of DEP aircraft featuring leading-edge propellers.

The integration in a preliminary aircraft sizing routine is a requirement for this new methodology. Hyperion, the procedure developed at Politecnico di Milano, already implements a fast and reliable approach for DEP modeling based on Patterson's method. The idea is then to create a model suitable for more advanced design phases, like the preliminary sizing of specific components of the aircraft. TITAN, another code developed at Politecnico di Milano, will thus be the framework integrating this novel method.

The sizing procedure will interrogate a multi-dimensional map of the design space to increase the accuracy while preserving the rapidity of a purely algebraic approach. This map, generated in advance using several mid-fidelity simulations, will significantly reduce the computational cost compared to the one required if the mid-fidelity numerical method gets integrated into the sizing loop.

To summarize, the main objectives of this thesis are:

- The **validation of a mid-fidelity method** capable of capturing the aero-propulsive interaction typical of a DEP aircraft.
- The **development of a DEP meta-model** suitable for preliminary aircraft sizing, taking advantage of the previously validated method.

- The **integration of the developed meta-model** within an existing aircraft sizing routine.

1.3 Thesis outline

Chapter 2 presents an overview of methods for aero-propulsive modeling suitable for preliminary sizing of DEP aircraft and validates them by comparing numerical results with experimental data. Chapter 3 extends the validated modeling approach to a multiple propeller case and performs some quick studies regarding overlapping propellers, counter-rotating layout, and WTPs. Chapter 4 briefly illustrates UNIFIER19, the aircraft used in the meta-model derivation, alongside the so-called reduced approach, i.e., a procedure used to lower the computational costs of the simulations. Chapter 5 describes the development of the DEP meta-model, including the preliminary dimensional analysis, the numerical campaign to derive the actual meta-model of the aero-propulsive interaction, and the changes to the current architecture of the sizing routine to integrate the new modeling features. Chapter 6 illustrates the implementation of the previously derived meta-model in TITAN and compares the results produced by the current and the modified sizing procedure. Finally, Chapter 7 drafts the conclusion of this thesis and outlines a few possible future developments of the present work.

Chapter 2

DEP Modeling in Preliminary Design

Optimizations, design space explorations, and sensitivity studies, are all highly demanding tasks in terms of computational cost carried out during preliminary aircraft sizing. Procedures evaluating aerodynamics, stability, and further aspects, need to be run several times (at each iteration, for every configuration, etc.). High-fidelity models are generally too time-consuming to be integrated into sizing loops. Low- or mid-fidelity methods are thus required to complete the early design phase in a reasonable time.

2.1 Available modeling tools

Concerning the aero-propulsive analysis, CFD is the numerical method setting the reference in terms of accuracy. However, its extremely high computational cost makes this technique unsuitable for preliminary aircraft design.

For conventional configuration, fast and well-proven methods are already available. On the other hand, innovative designs, like those implementing DEP, require novel approaches. Strategies implemented so far includes: Lifting Line Method with Actuator disk theory correcting the velocity field seen by the wing, Vortex Lattice Method applied to the baseline wing plus the correction provided by an algebraic model, etc.

2.1.1 Patterson's method

In his 2016 dissertation [7], Patterson proposed this approach to model the aero-propulsive interaction of leading-edge propellers blowing a wing. The method is entirely algebraic and thus provides results almost immediately; moreover, its slightly conservative estimates represent an advantage in the early design phases.

Patterson uses actuator disk theory to predict the velocity field seen by the wing, both in terms of dynamic pressure and AoA. Their values are then the input of the procedure computing sectional lift coefficient relative increment. A correction factor from a surrogate model derived from two-dimensional CFD simulations is finally applied; it allows to take into account further aspects, like the propeller position and size.

The equation below is the expression of the lift coefficient increment of the entire wing, which combines the effects of multiple propellers if present:

$$\Delta C_L = C_{L_u} \sum_i \left(\frac{\Delta C_\ell}{C_{\ell_u}}\right)_i \left(\frac{S_{blown}}{S}\right)_i \tag{2.1}$$

The method cannot model 3D phenomena; therefore, it may produce less accurate results when applied to a low aspect ratio wing or propellers close to the wingtip. Moreover, this approach does not provide a way to estimate the drag coefficient increment.

Starting from Patterson's work, De Vries added a procedure to compute also ΔC_D, as well as ΔC_L [10]. The method is still completely algebraic and thus retains Patterson's rapidity; it also introduces further simplifications, like assuming a uniform wing blowing and a sectional lift coefficient of $2\pi\alpha$.

Many preliminary aircraft sizing routines, including the one developed at Politecnico di Milano (Hyperion), implement Patterson's or De Vries' approach [11] [12], no matter the method used to compute the unblown wing aerodynamic coefficients.

2.1.2 Vortex Lattice Method

VLM is a numerical method suitable for aerodynamic analysis in the early design stages. It can provide reasonably accurate estimates of both lift and lift-induced drag, being at the same time much faster than a CFD simulation. Although, since results computation is not instantaneous, repeating the process at each iteration may be impractical. Integration within a sizing loop will thus require exploiting a different strategy, like performing simulations in advance to generate a multi-dimensional map of the design space subsequently interrogated at each iteration.

Fig. 2.1 illustrates the concept behind the Vortex Lattice Method, representing the multiple horseshoe vortices applied on the discretized lifting surface.

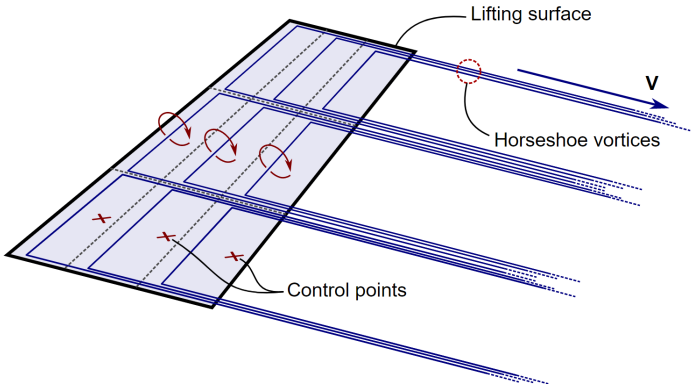

Fig. 2.1: Concept of the VLM discretization [13].

Many authors have chosen VLM to model the aero-propulsive interaction [14], sometimes even developing customized versions [15] [16] and implementing them into their DEP aircraft sizing tools [17].

Two main approaches exist to model propellers in VLM: one relies on the actuator disk theory, while the other simulates the entire system using VLM given the blade geometry. In details:

- **Actuator disk theory** is the most common way to model propellers in low- and medium-fidelity methods. Given the thrust coefficient, it can compute the velocity field behind the propeller, used in turn to estimate the wing performance. The simplicity of this approach is both the key to its rapidity and the reason for its inaccuracy. A simple one-way interaction from the propeller to the wing takes the place of a more complex aero-propulsive coupling.
- The **purely VLM approach** implies the also the propeller geometry is modeled and used to perform time-marching simulations of the entire system. This approach does not require characterizing a priori the propeller performance, i.e., computing its thrust coefficient; setting RPM is sufficient to run the simulations. The penalty associated with this approach is the higher computational cost due to the time-varying solution. On the other hand, the main advantage is the presence of the complete aero-propulsive coupling.

Several open-source codes implement VLM: FastVLM [11], Athena Vortex Lattice [18], and SUAVE [19], are just a few examples. The one used in the present thesis is VSPAero, a NASA-developed procedure integrated into the conceptual design suite OpenVSP [8]. The advantage offered by this software is the presence of a routine dedicated to parasite drag coefficient estimation (C_{D_0}).

2.1.3 Other methods

Other methods are available to model the aero-propulsive interaction typical of DEP aircraft. Two of them, tested in the early stages of this thesis, were later abandoned. The lack of resources, and the relatively low interest to carry on so many different approaches, led to this decision.

The lifting Line Method, combined with actuator disk theory [20], was implemented and later discarded considering its disadvantages compared to VLM. The latter, modeling propeller geometry and setting RPM, can simulate the actual aero-propulsive coupling instead of the simple one-way interaction.

DUST, a code that relies on the vortex particle method developed at Politecnico di Milano [21], was also considered. It does not require information about the propeller performance, just as VLM; geometry and RPM are sufficient. Some problems with drag estimation, combined with the good results provided by other methods, suggested discarding this approach and not investing too much effort in further investigation of the issue.

2.2 Validation process

Before integrating it into a sizing procedure, any novel method requires validation, a process aiming to verify its fidelity, i.e., the ability to produce accurate results. Reliable data, either coming from experiments or high-fidelity numerical simulations, generally represent the reference in this process.

2.2.1 Sinnige's experimental data

In the context of the present thesis, experimental data collected by Sinnige and reported in [22] represents the reference for validation. Two main reasons were

behind this choice: first of all, the entire geometry of the system is known, including the blade pitch and chord distributions; secondly, several other studies, carried out by different authors, use the same setup [14] [23]. The first point represents an advantage for numerical methods implementing actual propeller geometry rather than actuator disks; the latter one, instead, provides further information or a more in-depth look into some aspects.

Fig. 2.2 illustrates Sinnige's setup for the Mid-Wing Propeller, also referred to as Conventional configuration by the author. The experiments, carried out at a freestream velocity of 40 m/s, took place in the Low-Turbulence Tunnel at Delft University of Technology. For further details, the reader can refer to [22].

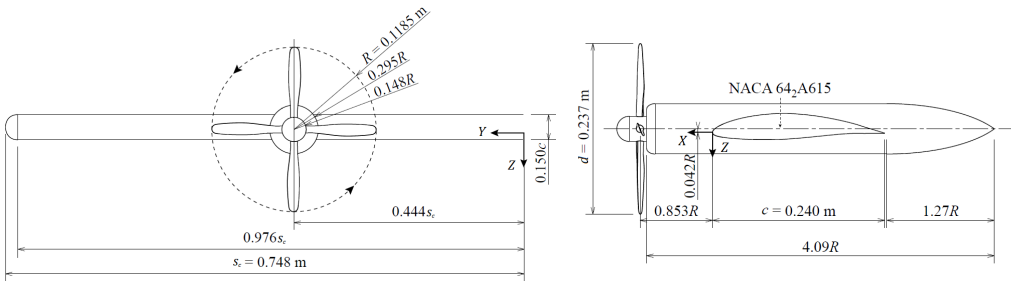

(a) front view (b) side view

Fig. 2.2: Sinnige's experimental setup (MWP) [22].

Thrust direct measurements are not available since the balance, placed at the wing root, measures the forces acting on the entire system; therefore, decoupling between aerodynamic and propulsive contributions is impossible.

Fig. 2.3 presents complete system force coefficients, acquired by Sinnige for multiple electric motor settings, corresponding to advance ratios ranging from 0.7 to 1.0. Prop-off data refers to forces acting on the setup of Fig. 2.2 but with the propeller removed. Grey curves correspond to the results of the Tip-mounted configuration, which despite being the main topic of Sinnige's work, is not relevant in the present discussion.

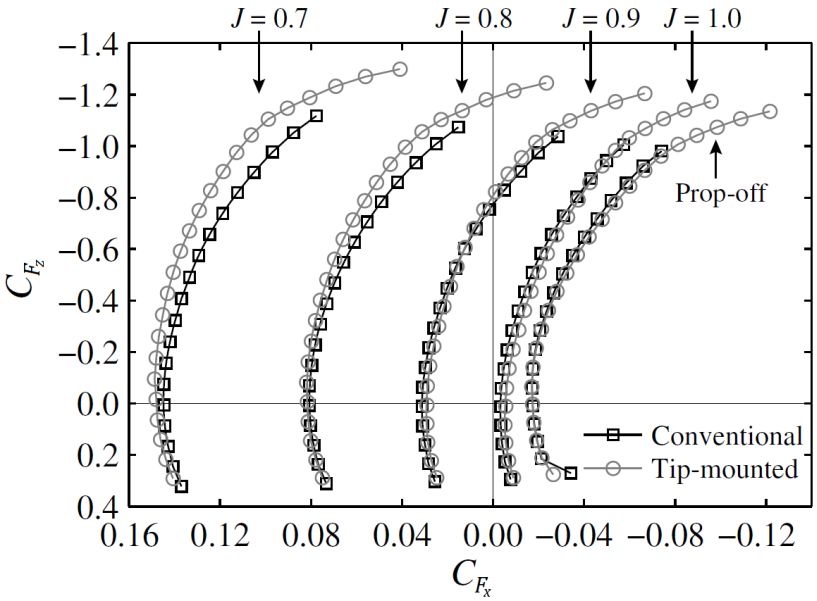

Fig. 2.3: Experimental complete system force coefficients [22].

Experimental data contains the actual aero-propulsive coupling, consisting of the mutual effects between wing and propeller. To quantify this interaction in a structured and consistent way, the net thrust of the sting-mounted propeller setup, collected during a separate experiment, is removed from the forces measured on the complete system as shown in the equations below:

$$L^* = -F_z - T \sin \alpha \tag{2.2}$$

$$D^* = -F_x + T \cos \alpha \tag{2.3}$$

The resulting quantities, named effective lift and effective drag, allow taking into account the extent of the interaction, assigning all its effects to the wing. A reduction of effective drag with respect to the prop-off case, for example, can either be produced by an actual drag reduction or by a net thrust higher than the one measured on the propeller assembly alone.

The net thrust of the sting-mounted propeller setup, so far mentioned multiple times, is the axial force produced by the propeller when mounted on its nacelle. Nacelle drag, measured in advance, allows removing its contribution from the total force acting on the propeller assembly, thus obtaining the net thrust. On the other hand, the nacelle interference with the propeller is still present.

Fig. 2.4 plots thrust coefficient against Angle of Attack for different advance ratios. Those are the curve used to compute the effective experimental polars and their corresponding effective parameters.

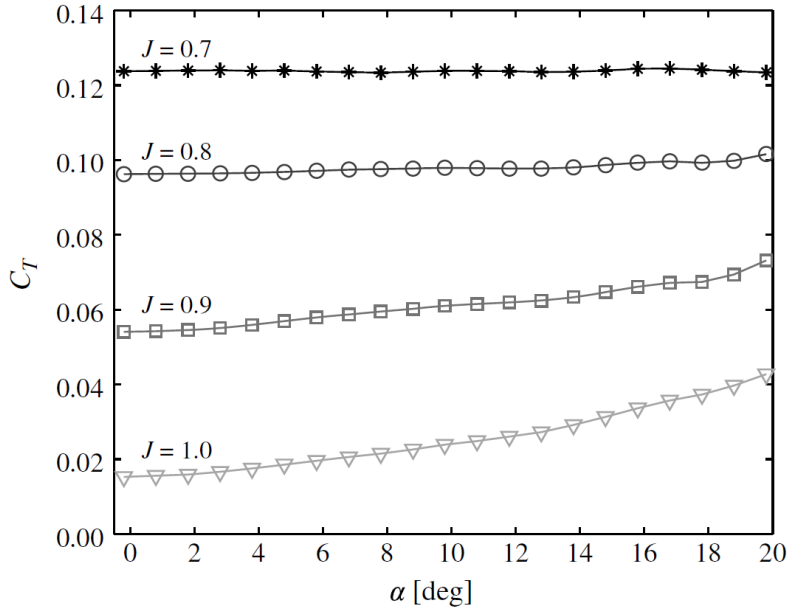

Fig. 2.4: Experimental net thrust of the sting-mounted propeller setup [22].

2.2.2 Implementation of the actuator disk approach

Fig. 2.5 summarizes the so-called actuator disk approach, including thrust removal to compute effective coefficients. At first, all the numerical methods except DUST implemented actuator disk theory. Rapidity was a significant advantage: VLM simulations generally converged in less than 15 iterations (a few seconds on a high-end personal computer). The major drawback was the absence of a complete aero-propulsive coupling, replaced by a one-way

interaction. Since the only available thrust coefficients are those obtained from the experiment on the sting-mounted propeller, models do not include any of the effects the wing induces on the propeller, like blockage or swirl recovery.

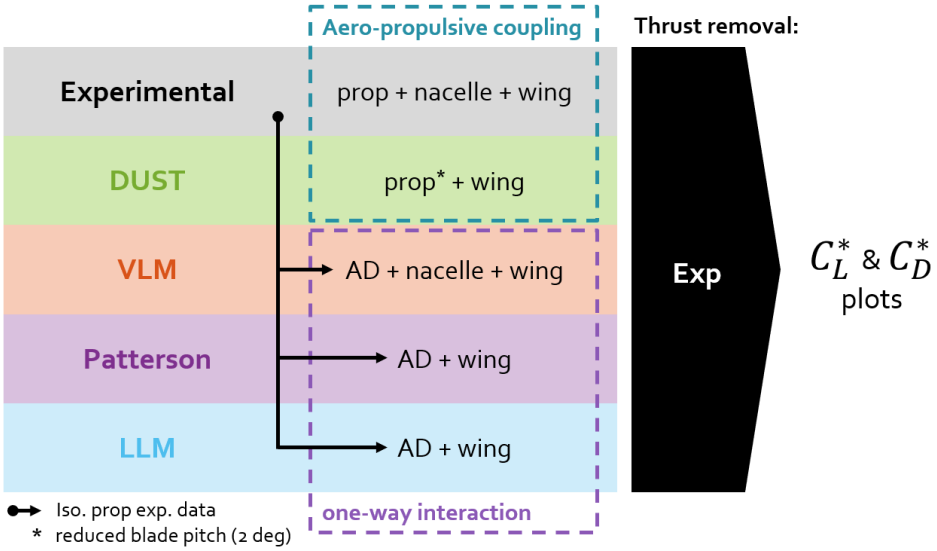

Fig. 2.5: Actuator disk approach.

Fig. 2.6, also taken from Sinnige's work [22], illustrates the radial distribution of the total pressure rise downstream of the propeller. Depending on the advance ratio, the portion of the blades effectively blown by the propeller, i.e., the one with a positive ΔC_{p_t}, starts in a range from 38% to 50% of the propeller radius. Sinnige attributed this behavior to separation phenomena induced by the locally inefficient airfoils close to the root. Increasing hub radius with respect to the geometrically accurate value (15%R) will thus improve the numerical predictions. Tab. 2.1 reports the effective hub radii used in the simulations; since implementing changes on actuator disks is relatively easy, each advance ratio uses its specific value.

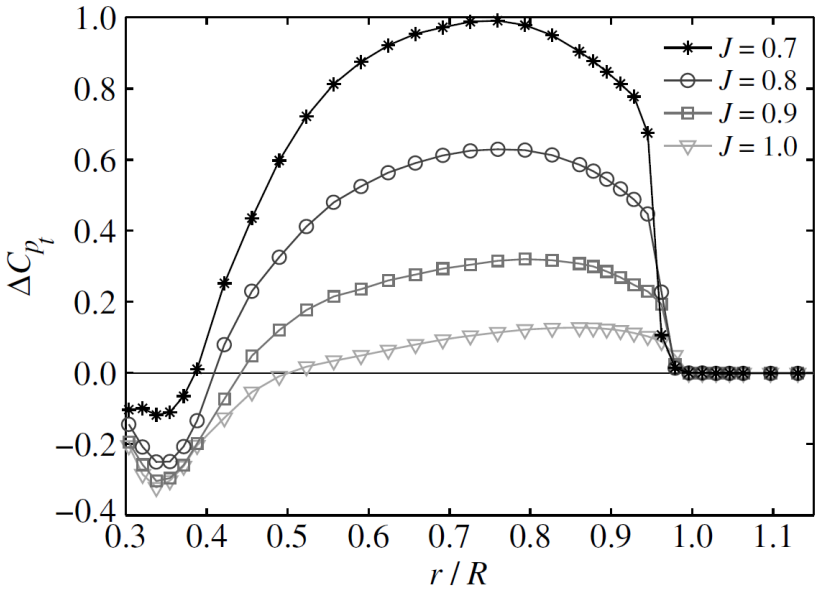

Fig. 2.6: Total pressure coefficient rise at 0.15R downstream the propeller [22].

J	r_h
0.7	38%R
0.8	41%R
0.9	44%R
1.0	50%R

Tab. 2.1: Actuator disk effective hub radius.

2.2.3 Implementation of the purely VLM approach

Fig. 2.7 summarizes the purely VLM approach. This method got its name due to actual propellers replacing actuator disks in the VLM models. Complete system VLM simulations provide the thrust coefficients used as actuator disk settings for the methods still implementing them (LLM and Patterson).

Numerical methods do not rely on experimental data since the sting-mounted propeller thrust coefficient is no longer needed to set up the simulations. Moreover, to fairly compare the results, the net numerical thrust of the propeller-nacelle assembly is removed from the complete system numerical forces; on the other hand, experimental data reduction still relies on the net thrust measured in the wind tunnel.

This method significantly increased the computational costs: to obtain an adequate periodic-state solution, five revolutions divided into 120 time-steps are required (approximately 11 minutes on a high-end personal computer). However, modeling the complete aero-propulsive coupling represents a substantial fidelity improvement.

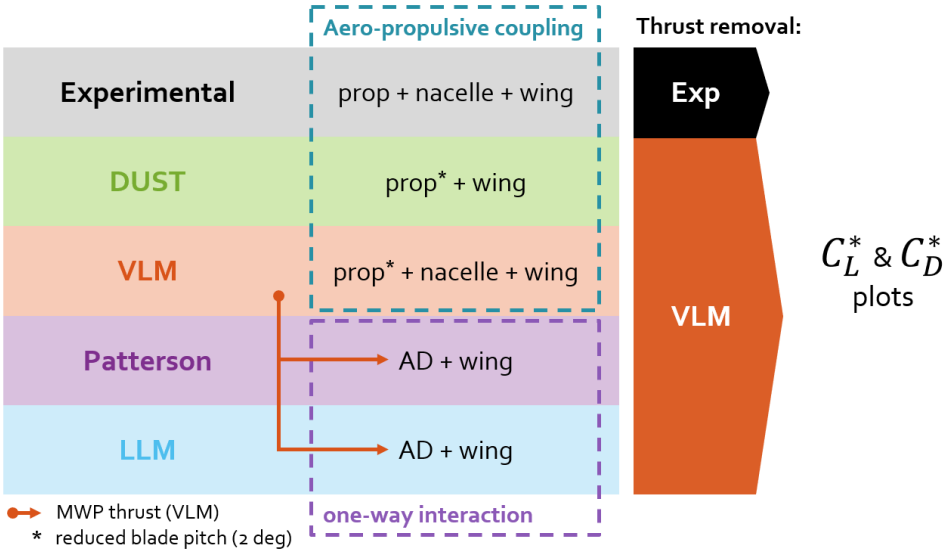

Fig. 2.7: Purely VLM approach.

The purely VLM approach, as already mentioned, requires a detailed model of the propeller geometry. Before adding it to the wing, however, VLM capability to capture real propeller performance needs validation. Fig. 2.8a

illustrates the initial configuration tested: blades are geometrically accurate, and no nacelle is present.

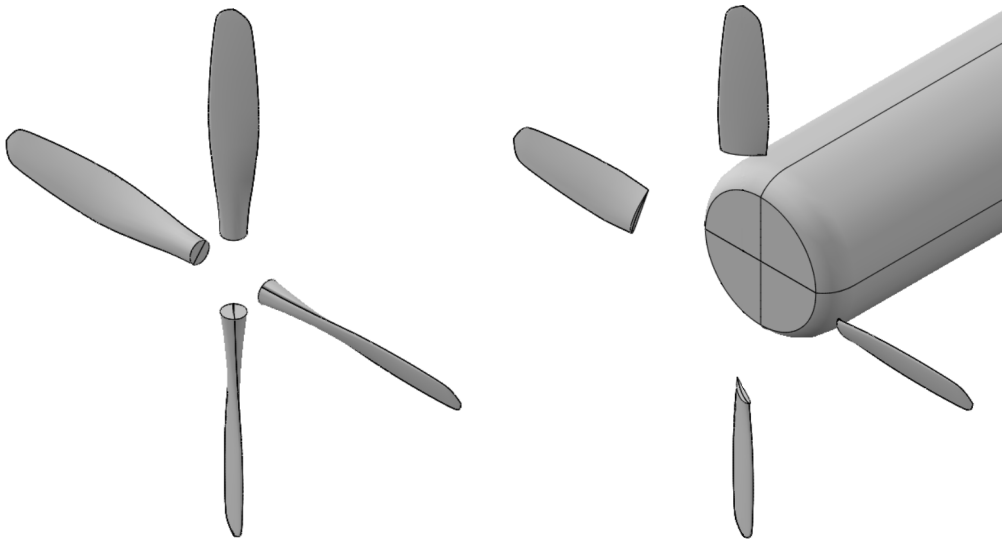

(a) initial geometry (b) final geometry

Fig. 2.8: OpenVSP models of the propeller.

Fig. 2.9a compares the experimental and numerical curves of the thrust coefficient against the advance ratio. The initial configuration, associated with the blue dash-dotted line, clearly overestimates the thrust of the experimental setup. This behavior, also observed in the results of DUST, appears to be a common side effect. Willemsen [24], who used the same setup as Sinnige, attributed the discrepancy to the difficulty of estimating airfoil polars at the low Reynolds numbers typical of a propeller blade, where viscous effects are predominant. The suggested workaround is a reduction of the pitch of the blades; a 2° reduction was sufficient for both VLM and DUST.

Hub radius is another parameter modified during the validation. Since the VLM solver considers only the chamber line of the airfoils, the thick sections close to the blade root are treated just like any other section with an equivalent chamber. In order to exclude these locally inefficient airfoils from the computation, a 45%R increased effective hub radius replaced the geometrically accurate one (15%R). The value of 45% falls right in the middle of the range of Tab. 2.1.

Adding the nacelle was the last change applied to the propeller model; Fig. 2.8b shows the final configuration, i.e., the one obtained by implementing all the changes described so far and eventually added to VLM models of the blown wing. The provided thrust is always a net thrust, computed by removing the drag contribution from the total force. However, the presence of the nacelle models its interference effects, thus contributing to the accuracy of the results.

Returning to Fig. 2.9a, the red dash-dotted line, associated with the final configuration of Fig. 2.8b, shows a definitely better match with the experimental black solid curve. Even for the power coefficient, plotted in Fig. 2.9b against the advance ratio, experimental data are considerably closer to the final configuration VLM results. However, due to a slight underestimation, the matching is not as good as the one observed on C_T.

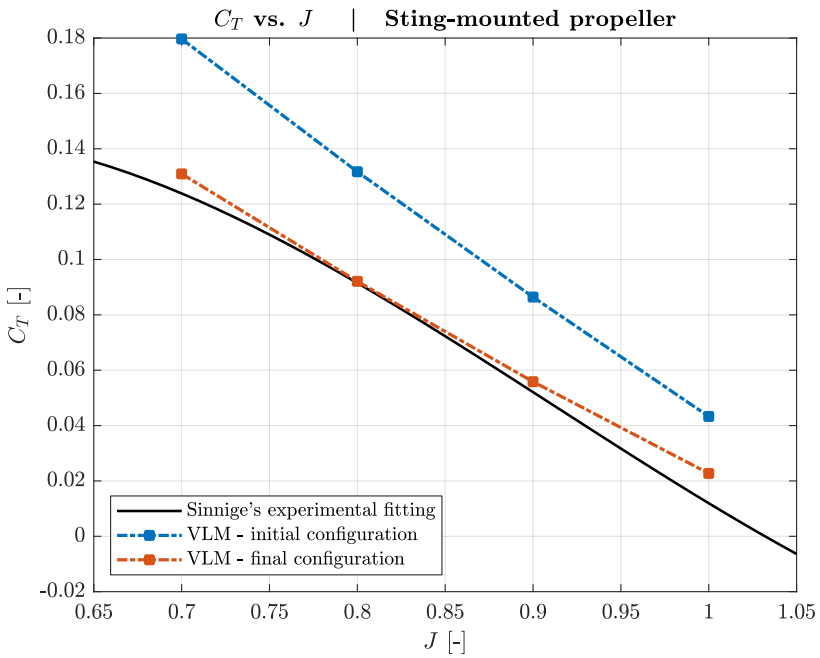

(a) thrust coefficient

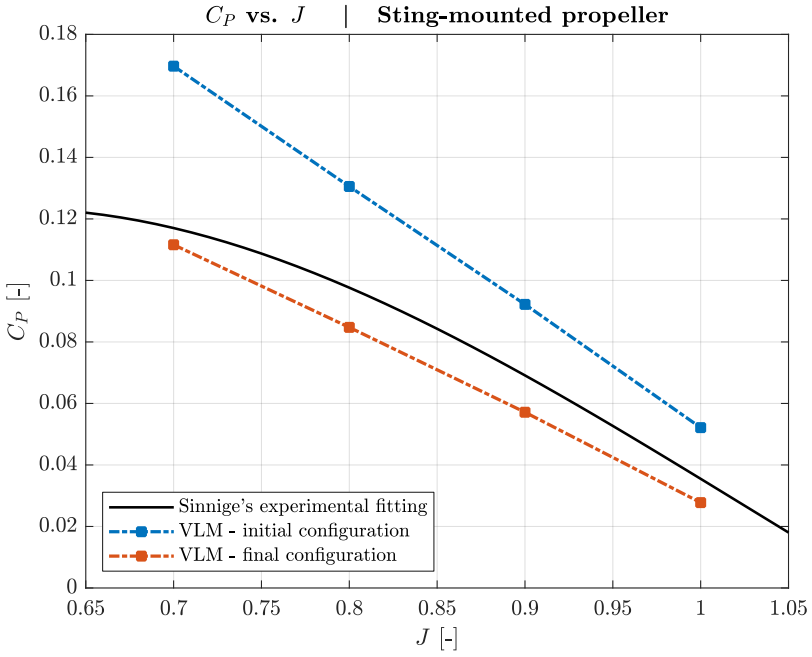

(b) power coefficient

Fig. 2.9: Numerical and experimental sting-mounted propeller performance.

Finally, Fig. 2.10 illustrates the experimental thrust coefficient against AoA of the sting-mounted propeller, already reported in Fig. 2.4, superimposed to corresponding numerical results of the propeller-nacelle assembly. Intermediate advance ratios (0.8 and 0.9) present a closer match between experimental and numerical curves than the one exhibited by extreme values of J (0.7 and 1.0), for which thrust is slightly overpredicted as already noticed in Fig. 2.9a.

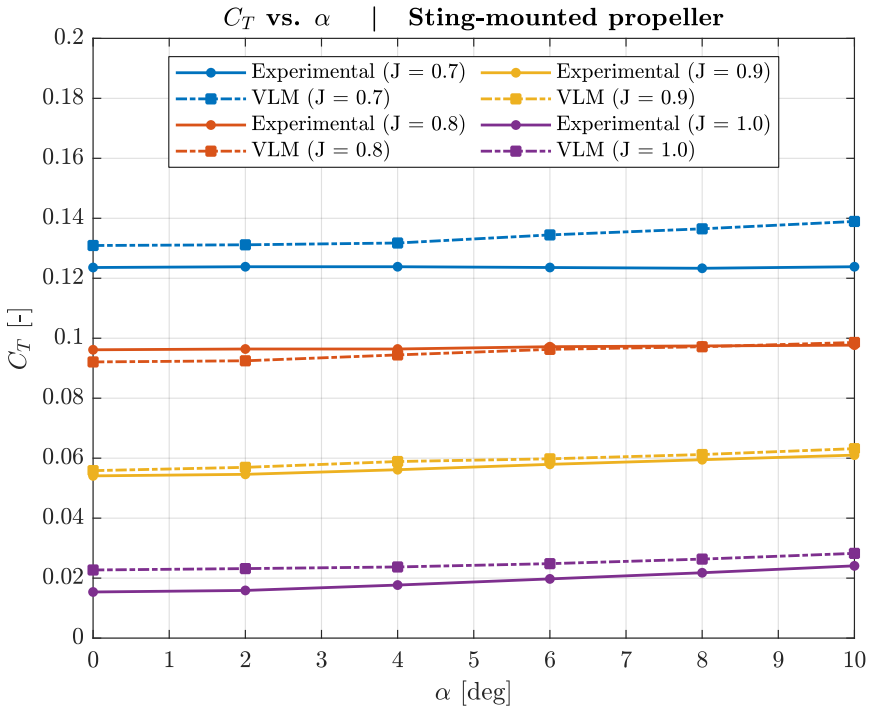

Fig. 2.10: Comparison between experimental and numerical thrust coefficients.

2.2.4 Data processing method

Despite the rapidity offered by the actuator disk approach, illustrated in Fig. 2.5, the ultimate choice falls on the purely VLM approach, summarized in Fig. 2.7. If the former integrates a BEMT procedure, RPM and propeller geometry are sufficient to estimate the coefficients required by the AD; thus, relying on the same inputs, both methods are equally valid in terms of generality. However, since the BEMT considers neither the presence of the wing nor the one of the nacelle, the already simple one-way interaction will be even simpler than using the experimental thrust coefficient, which at least contained the nacelle interference. On the other hand, the purely VLM strategy increases the accuracy of the results, modeling the complete aero-propulsive coupling between wing and propeller.

An example of the actuator disk approach, including DUST and LLM results, will be shown in Section 2.2.6. For the reasons already reported in Section 2.1.3, those two methods were later discarded and thus not treated in the following discussion.

The purely VLM approach, now rearranged by removing DUST and LLM, consists in:

1. RESULT COMPUTATION:

    a. Computing complete system forces using VLM (it requires the model of the entire system and the propeller RPM);

    b. Computing complete system forces using Patterson's method (it requires the propeller net thrust coefficient coming from VLM complete system simulations);

2. DATA REDUCTION:

   a. Removing the net thrust measured on the sting-mounted propeller from the experimental complete system forces;

   b. Computing the net numerical thrust of the propeller-nacelle assembly using VLM;

   c. Removing the net numerical thrust of the propeller-nacelle assembly from complete system forces computed using VLM and Patterson's method;

Data reduction implements the already mentioned Eqs. (2.2) and (2.3) to get the effective lift and drag. Dividing then these effective forces by dynamic pressure q and reference surface S, produces the so-called effective coefficients: C_L^* and C_D^*, eventually used to plot the effective polars.

A well-proven approach, i.e., fitting analytic expressions to the experimental and numerical data points, allows parametrizing the polars and easing the comparisons. The lift coefficient model:

$$C_L^* = C_{L_\alpha}^*(\alpha - \alpha_0^*) \tag{2.4}$$

is linear with respect to the AoA; instead, the drag coefficient model:

$$C_D^* = minC_D^* + K^*\left(C_L^* - C_{L_{minC_D}}^*\right)^2 \tag{2.5}$$

is a quadratic function of the lift coefficient.

Validating VLM ability to predict propeller performance was one of the topics discussed in Section 2.2.2 and Section 2.2.3. A similar procedure, applied to the unblown wing, verifies the numerical method accuracy in estimating experimental lift and drag polars.

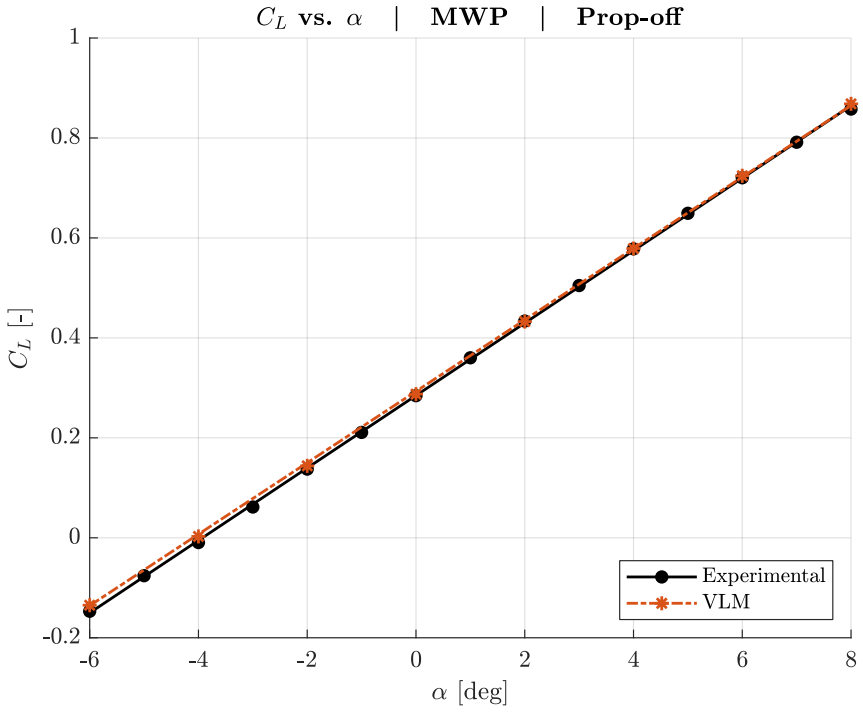

Fig. 2.11: Experimental and numerical lift polars (prop-off).

	$C^*_{L_\alpha}$ [deg $^{-1}$]	ΔC_{L_α} [%]	α^*_0 [deg]	$\Delta\alpha_0$ [deg]
Exp	0.0725	–	−3.9277	–
VLM	0.0715	−1.4	−4.1001	−0.172

Tab. 2.2: Experimental and numerical lift polar parameters (prop-off).

Fig. 2.11 presents both the experimental and the VLM lift coefficient against AoA curves. The numerical prediction is very accurate, as confirmed by the values reported in Tab. 2.2. Discrepancies, both in terms of slope (ΔC_{L_α}) and zero-lift AoA ($\Delta\alpha_0$), are almost negligible.

Fig. 2.12 compares the experimental and the numerical drag polars. Although the matching is not as good as on lift, rarely flown conditions present the most significant variations, such as those at very low or even negative C_L.

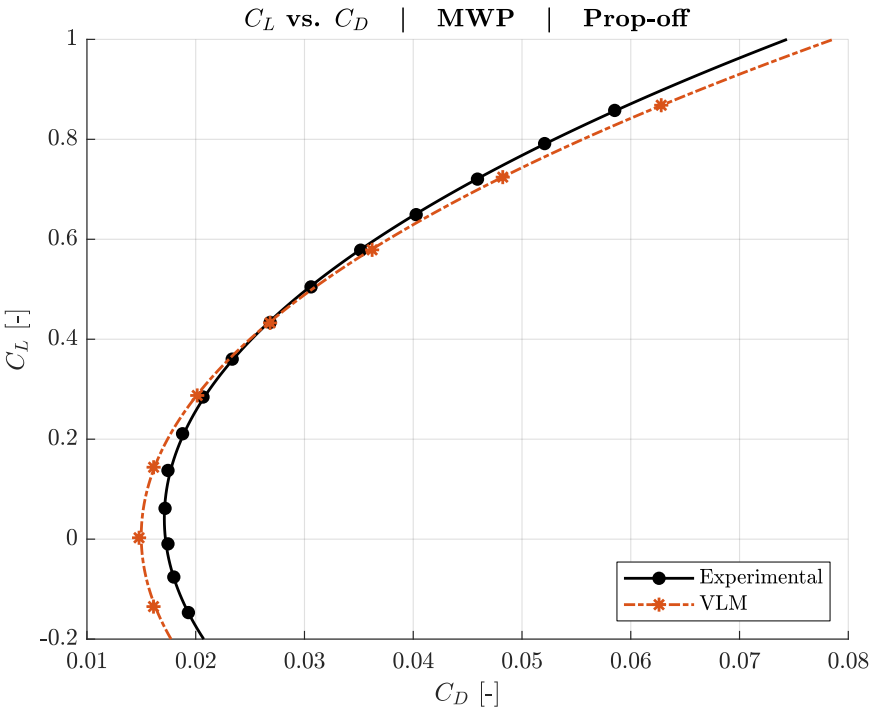

Fig. 2.12: Experimental and numerical drag polars (prop-off).

	$minC^*_D$ [−]	$\Delta minC_D$ [%]	$C^*_{L_{minC^*_D}}$ [−]	$\Delta C_{L_{minC_D}}$ [−]	K^* [−]	ΔK [%]
Exp	0.0171	–	0.0412	–	0.0623	–
VLM	0.0150	−12.3	0.0062	−0.035	0.0644	+3.4

Tab. 2.3: Experimental and numerical drag polar parameters (prop-off).

Tab. 2.3 reports the values of the parameters associated with the unblown wing drag polar. Their comparison quantifies the already noted discrepancies in the region of the minimum drag coefficient, with a 12.3% reduction of the $minC_D^*$. The deviation is very similar to the one observed by Veldhuis in [14], comparing the experimental data collected using the same setup of Sinnige and the results provided by his custom VLM code. The curves of Fig. 2.13a and Fig. 2.13b, taken from Veldhuis' work, respectively resemble those of Fig. 2.11 and Fig. 2.12. In particular, the AoA above which the numerical method starts overpredicting drag is the same in both the present thesis and [14].

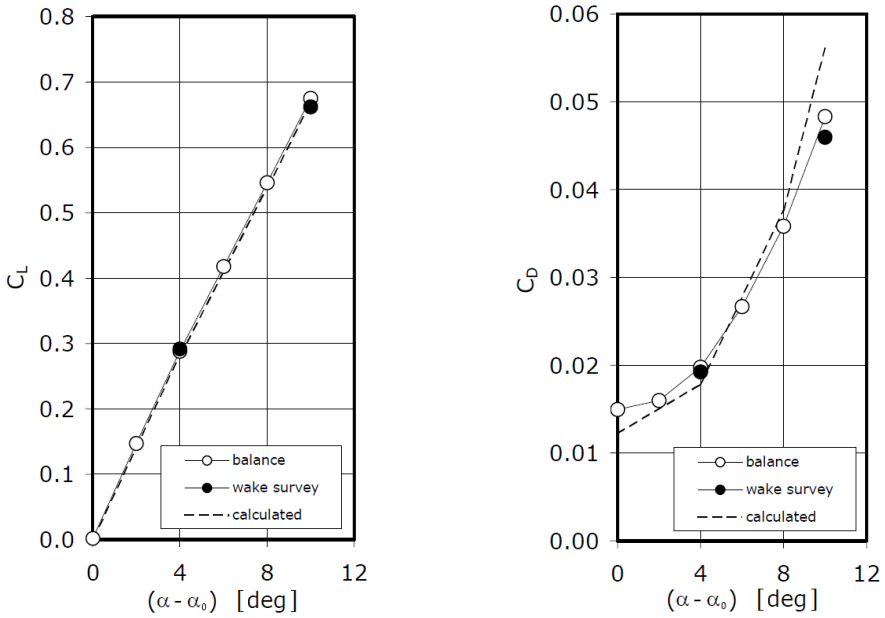

(a) lift polar (b) drag polar

Fig. 2.13: Veldhuis lift and drag polars [14].

It is worth recalling that in the prop-off case, the propeller is not mounted on the experimental setup and is not present in the VSPAero model. Therefore, since there is no thrust to remove, the effective lift and drag coincide with the complete system forces.

2.2.5 Analysis of blown wing numerical results

The following paragraphs extensively illustrate the numerical results of the blown wing, computed for all the four advance ratios used by Sinnige, and compare them with the experimental data. Plots represent data points alongside the analytic polars fitting them. Tables contain the parameters of the curves and the deviations between the numerical values and their experimental counterparts, used as references.

In addition, tables also compare the blown configurations parameters with those of the unblown wing, using formulas like the one reported below:

$$\Delta C_{L_\alpha}^{off} = C_{L_\alpha}^* - C_{L_\alpha}^{off} \tag{2.6}$$

Since the prop-off polars showed an intrinsic error, illustrated above, introduced by VLM even on a less complicated setup than the complete system one, the numerical unblown wing represents the unblown reference for VLM, trying to exclude those intrinsic discrepancies.

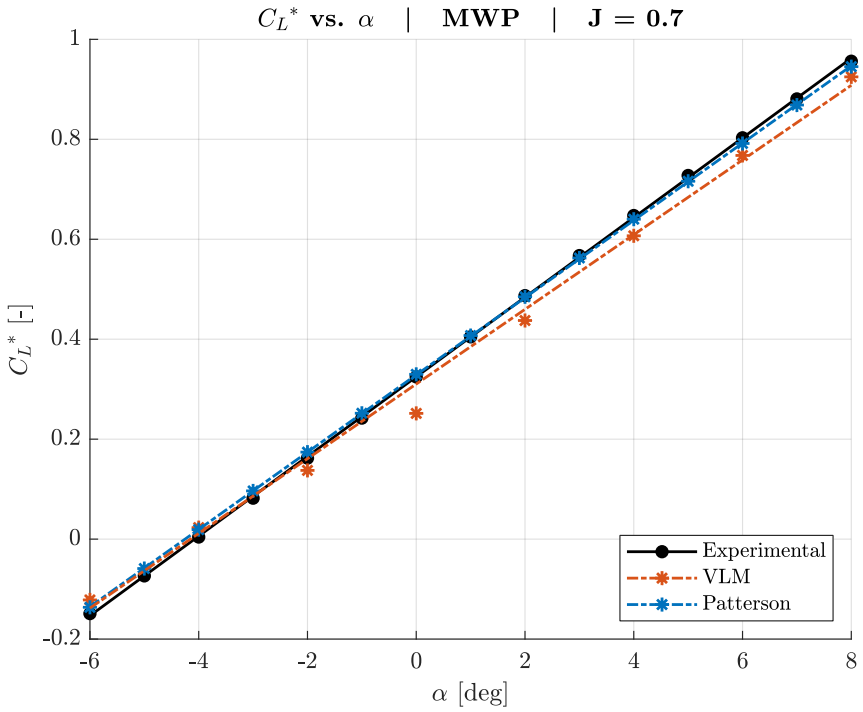

Fig. 2.14: Experimental and numerical lift polars ($J = 0.7$).

Fig. 2.14 illustrates the experimental and the numerical lift coefficient against AoA curves for the lowest advance ratio, i.e., 0.7. Patterson's results are closer to experimental data, as confirmed by the lower slope deviation in Tab. 2.4a: –3.0% instead of the –6.3% observed on VLM. The latter also presents some biased data points at low α. With respect to the unblown wing, both slope and zero-lift AoA change as expected: ΔC_{L_α} is positive and $\Delta\alpha_0$ is negative, as reported in Tab. 2.4b.

	$C^*_{L_\alpha}$ [deg $^{-1}$]	ΔC_{L_α} [%]	α_0^* [deg]	$\Delta\alpha_0$ [deg]
Exp	0.0797	–	–4.0765	–
VLM	0.0747	–6.3	–4.1534	–0.077
Patt	0.0773	–3.0	–4.2502	–0.176

(a) comparison among blown wing results

	$C^*_{L_\alpha}$ [deg $^{-1}$]	$\Delta C^{off}_{L_\alpha}$ [%]	α_0^* [deg]	$\Delta\alpha_0^{off}$ [deg]
Exp	0.0797	+9.9	–4.0765	–0.149
VLM	0.0747	+4.5	–4.1534	–0.053
Patt	0.0773	+6.6	–4.2502	–0.324

(b) comparison between blown and unblown wing results

Tab. 2.4: Experimental and numerical lift polar parameters ($J = 0.7$).

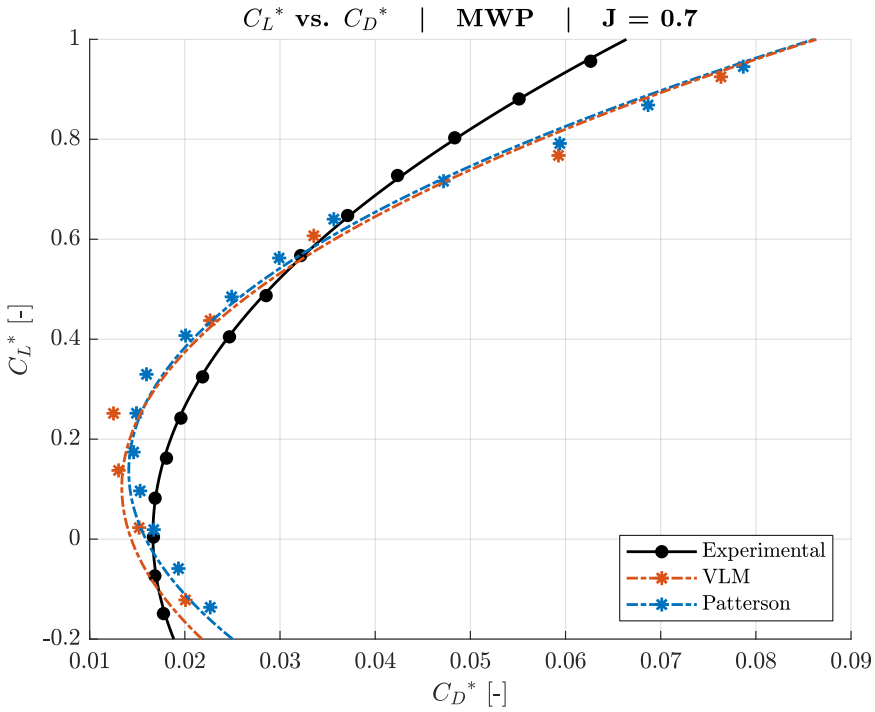

Fig. 2.15: Experimental and numerical drag polars ($J = 0.7$).

Fig. 2.15 illustrates the drag polars of the blown wing, with the propeller RPM set to obtain an advance ratio of 0.7.

	$minC_D^*$ [–]	$\Delta minC_D$ [%]	$C^*_{L_{minC_D^*}}$ [–]	$\Delta C_{L_{minC_D}}$ [–]	K^* [–]	ΔK [%]
Exp	0.0166	–	0.0084	–	0.0506	–
VLM	0.0134	−19.3	0.1044	+0.096	0.0910	+79.8
Patt	0.0141	−15.1	0.1362	+0.128	0.0965	+90.7

(a) comparison among blown wing results

	$minC_D^*$ [–]	$\Delta minC_D^{off}$ [%]	$C^*_{L_{minC_D^*}}$ [–]	$\Delta C^{off}_{L_{minC_D}}$ [–]	K^* [–]	ΔK^{off} [%]
Exp	0.0166	−2.9	0.0084	−0.033	0.0506	−18.8
VLM	0.0134	−10.7	0.1044	+0.098	0.0910	+41.3
Patt	0.0141	−17.5	0.1362	+0.095	0.0965	+54.9

(b) comparison between blown and unblown wing results

Tab. 2.5: Experimental and numerical drag polar parameters ($J = 0.7$).

In Tab. 2.5a, concavity and minimum drag show significant deviations between numerical and experimental curves. Since the discrepancies are present in the results of both numerical methods, inadequate complete system thrust estimation is the most probable cause. To further support this

explanation, Patterson's aerodynamic model produces a strictly positive increment of drag, the negative $\Delta minC_D^{off}$, in Tab. 2.5b, is thus necessarily the result of thrust discrepancies. More details are in Section 2.2.6.

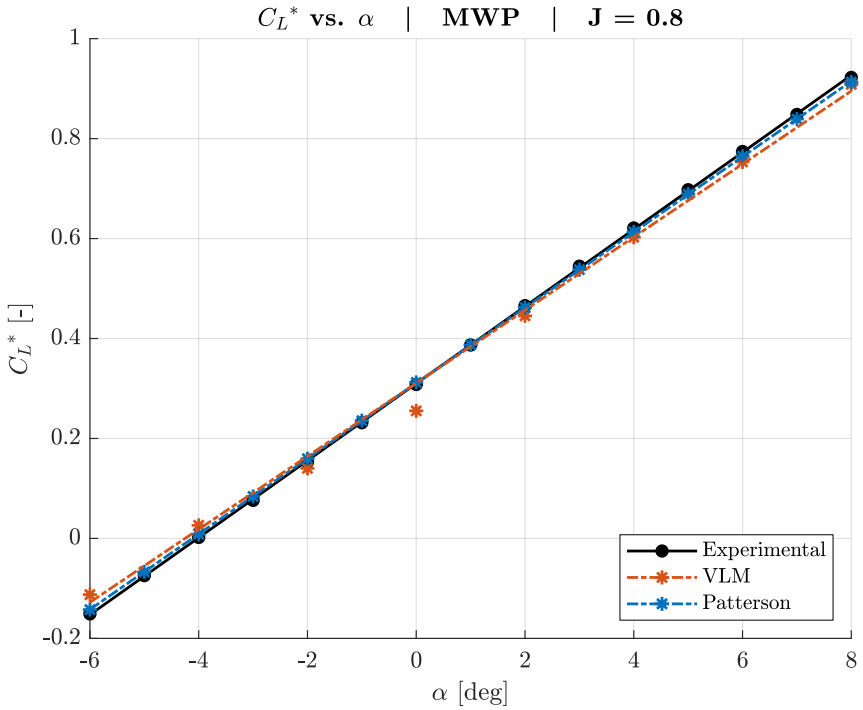

Fig. 2.16: Experimental and numerical lift polars ($J = 0.8$).

Fig. 2.16 and Tab. 2.6 present the lift polars associated with an advance ratio of 0.8. The behavior is similar to the one observed on the lowest J, with a slightly better match between numerical and experimental parameters (Tab. 2.6a).

	$C^*_{L_\alpha}$ [deg $^{-1}$]	ΔC_{L_α} [%]	α_0^* [deg]	$\Delta\alpha_0$ [deg]
Exp	0.0771	–	−4.0207	–
VLM	0.0731	−5.2	−4.2506	−0.230
Patt	0.0755	−2.1	−4.1183	−0.097

(a) comparison among blown wing results

	$C^*_{L_\alpha}$ [deg $^{-1}$]	$\Delta C^{off}_{L_\alpha}$ [%]	α_0^* [deg]	$\Delta\alpha_0^{off}$ [deg]
Exp	0.0771	+6.3	−4.0207	−0.093
VLM	0.0731	+2.2	−4.2506	−0.151
Patt	0.0755	+4.1	−4.1183	−0.190

(b) comparison between blown and unblown wing results

Tab. 2.6: Experimental and numerical lift polar parameters ($J = 0.8$).

Blowing effects, like the slope increment in Tab. 2.6b, are more contained at this advance ratio due to a lower C_T.

The drag polars of Fig. 2.17 and Tab. 2.7 does not present significant variations with respect to their counterparts with $J = 0.7$. As already noted looking at the deltas of the lift against AoA curves, the trends of the discrepancies remain the same while their magnitudes decrease.

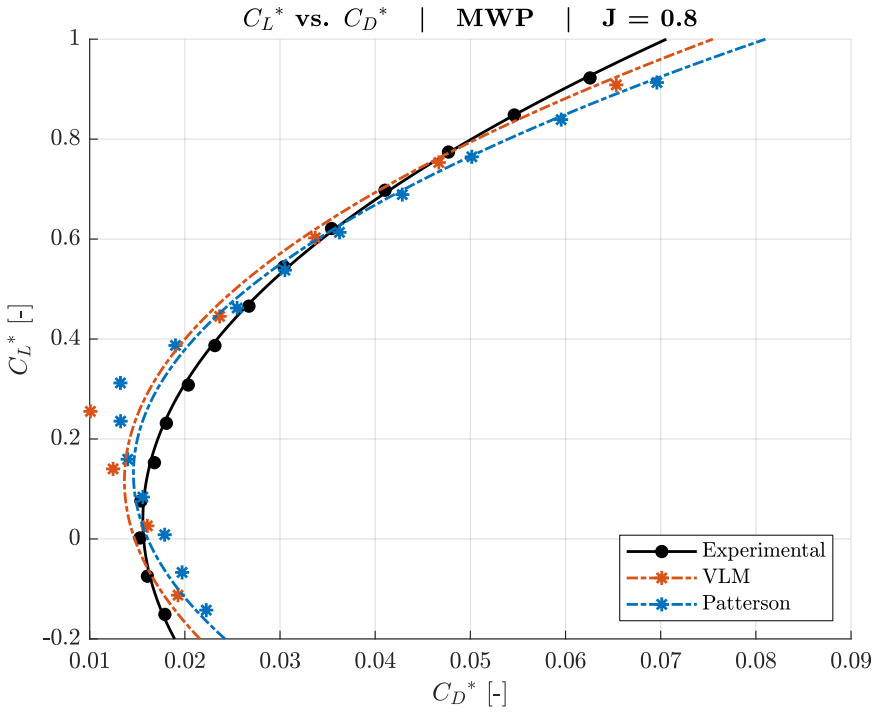

Fig. 2.17: Experimental and numerical drag polars ($J = 0.8$).

	$minC_D^*$ [–]	$\Delta minC_D$ [%]	$C^*_{L_{minC_D^*}}$ [–]	$\Delta C_{L_{minC_D}}$ [–]	K^* [–]	ΔK [%]
Exp	0.0156	–	0.0373	–	0.0594	–
VLM	0.0136	−12.8	0.1165	+0.079	0.0792	+33.3
Patt	0.0146	−6.4	0.1309	+0.094	0.0879	+48.0

(a) comparison among blown wing results

	$minC_D^*$ [–]	$\Delta minC_D^{off}$ [%]	$C^*_{L_{minC_D^*}}$ [–]	$\Delta C^{off}_{L_{minC_D}}$ [–]	K^* [–]	ΔK^{off} [%]
Exp	0.0156	−8.8	0.0373	−0.004	0.0594	−4.7
VLM	0.0136	−9.3	0.1165	+0.110	0.0792	+23.0
Patt	0.0146	−14.6	0.1309	+0.090	0.0879	+41.1

(b) comparison between blown and unblown wing results

Tab. 2.7: Experimental and numerical drag polar parameters ($J = 0.8$).

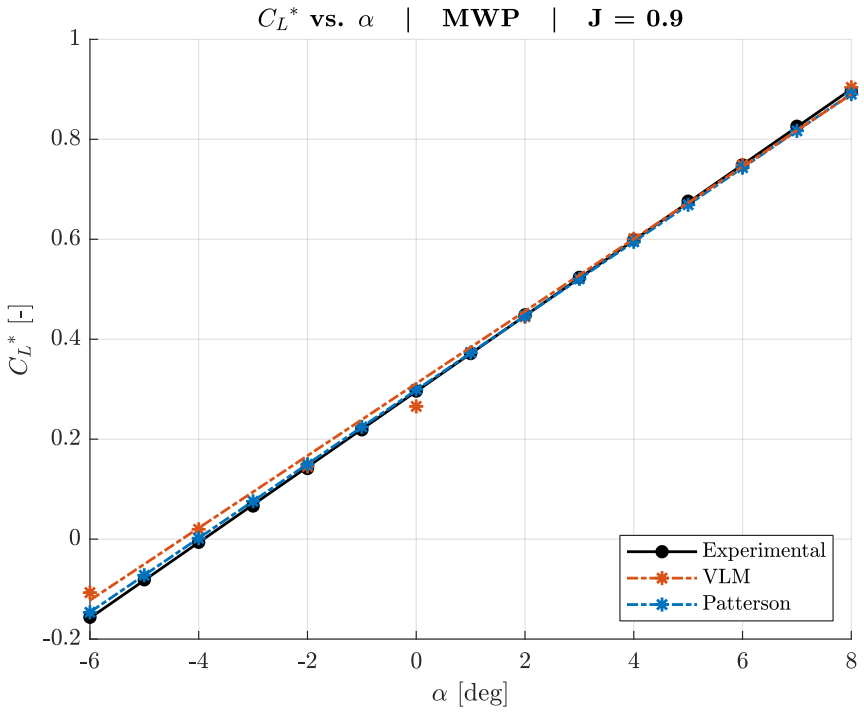

Fig. 2.18: Experimental and numerical lift polars ($J = 0.9$).

Fig. 2.18 illustrates the lift polars for $J = 0.9$, the corresponding parameters are in Tab. 2.8. The slope discrepancies in Tab. 2.8a are lower than in the previous cases, while $\Delta\alpha_0$ is more negative; therefore, the region were the analytic curves intersect and show the best agreements moves towards higher AoA. Within the considered range of α, VLM tendency at $J = 0.9$ is thus to overpredict lift, instead of underestimating it as for the lower advance ratios.

	$C^*_{L_\alpha}$ [deg $^{-1}$]	ΔC_{L_α} [%]	α_0^* [deg]	$\Delta\alpha_0$ [deg]
Exp	0.0756	–	−3.9114	–
VLM	0.0723	−4.4	−4.3082	−0.397
Patt	0.0741	−2.0	−4.0270	−0.116

(a) comparison among blown wing results

	$C^*_{L_\alpha}$ [deg $^{-1}$]	$\Delta C^{off}_{L_\alpha}$ [%]	α_0^* [deg]	$\Delta\alpha_0^{off}$ [deg]
Exp	0.0756	+4.3	−3.9114	+0.016
VLM	0.0723	+1.1	−4.3082	−0.208
Patt	0.0741	+2.2	−4.0270	−0.100

(b) comparison between blown and unblown wing results

Tab. 2.8: Experimental and numerical lift polar parameters ($J = 0.9$).

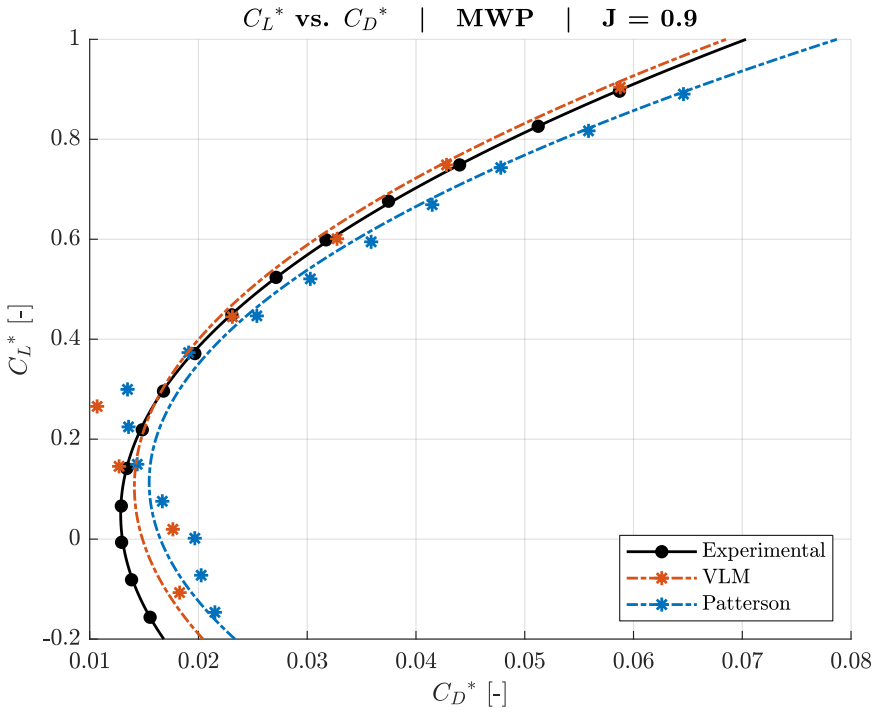

Fig. 2.19: Experimental and numerical drag polars ($J = 0.9$).

Fig. 2.19 highlights the very close match between VLM and experimental drag polars for C_L^* greater than 0.2. Patterson's results remain more conservative, as confirmed by the values of both $minC_D^*$ and K^* reported in Tab. 2.9a: 20.3% and 26.4% higher than their experimental counterparts.

	$minC_D^*$ [–]	$\Delta minC_D$ [%]	$C^*_{L_{minC_D^*}}$ [–]	$\Delta C_{L_{minC_D}}$ [–]	K^* [–]	ΔK [%]
Exp	0.0128	–	0.0496	–	0.0636	–
VLM	0.0141	+10.2	0.1048	+0.055	0.0679	+6.8
Patt	0.0154	+20.3	0.1133	+0.064	0.0804	+26.4

(a) comparison among blown wing results

	$minC_D^*$ [–]	$\Delta minC_D^{off}$ [%]	$C^*_{L_{minC_D^*}}$ [–]	$\Delta C^{off}_{L_{minC_D}}$ [–]	K^* [–]	ΔK^{off} [%]
Exp	0.0128	–25.1	0.0496	+0.008	0.0636	+2.1
VLM	0.0141	–6.0	0.1048	+0.099	0.0679	+5.4
Patt	0.0154	–9.9	0.1133	+0.072	0.0804	+29.1

(b) comparison between blown and unblown wing results

Tab. 2.9: Experimental and numerical drag polar parameters ($J = 0.9$).

Tab. 2.9b shows a significant reduction of the minimum drag coefficient between experimental blown and unblown wings (–25.1%). Due to the close

match between numerical and experimental thrust at $J = 0.9$, shown in Section 2.2.3, data reduction unlikely caused this deviation, which is, instead, probably related to the actual thrust increase on the complete system setup.

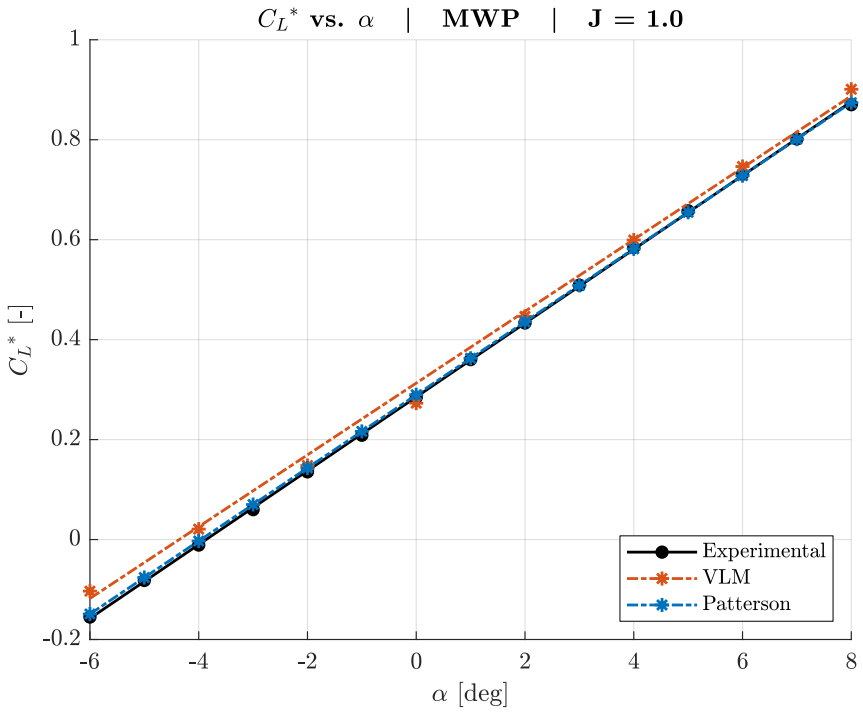

Fig. 2.20: Experimental and numerical lift polars ($J = 1.0$).

Fig. 2.20 compares the lift against AoA curves associated with the highest advance ratio considered by Sinnige.

	$C^*_{L_\alpha}$ [deg $^{-1}$]	ΔC_{L_α} [%]	α^*_0 [deg]	$\Delta\alpha_0$ [deg]
Exp	0.0738	–	−3.8639	–
VLM	0.0718	−2.7	−4.3589	−0.495
Patt	0.0731	−0.9	−3.9605	−0.097

(a) comparison among blown wing results

	$C^*_{L_\alpha}$ [deg $^{-1}$]	$\Delta C^{off}_{L_\alpha}$ [%]	α^*_0 [deg]	$\Delta\alpha^{off}_0$ [deg]
Exp	0.0738	+1.8	−3.8639	+0.064
VLM	0.0718	+0.4	−4.3589	−0.259
Patt	0.0731	+0.8	−3.9605	−0.033

(b) comparison between blown and unblown wing results

Tab. 2.10: Experimental and numerical lift polar parameters ($J = 1.0$).

Despite the reduced slope discrepancies reported in Tab. 2.10a, the larger $\Delta\alpha_0$ induces a slightly lift overestimation over the entire range of α.

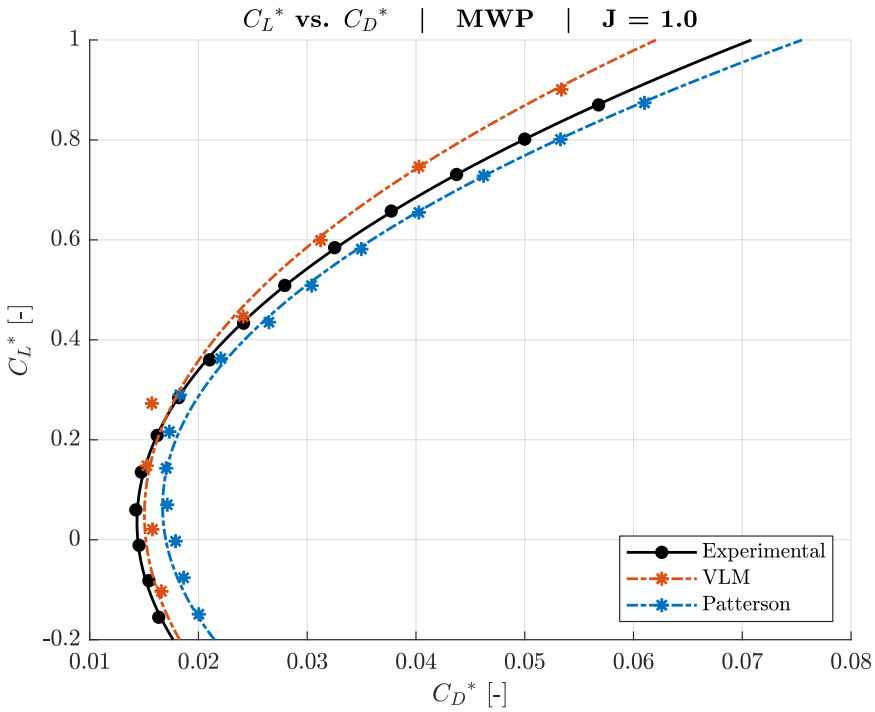

Fig. 2.21: Experimental and numerical drag polars ($J = 1.0$).

	$minC_D^*$ [–]	$\Delta minC_D$ [%]	$C^*_{L_{minC_D^*}}$ [–]	$\Delta C_{L_{minC_D}}$ [–]	K^* [–]	ΔK [%]
Exp	0.0143	–	0.0343	–	0.0606	–
VLM	0.0150	+4.9	0.0493	+0.015	0.0520	−14.2
Patt	0.0167	+16.8	0.0659	+0.032	0.0674	+11.2

(a) comparison among blown wing results

	$minC_D^*$ [–]	$\Delta minC_D^{off}$ [%]	$C^*_{L_{minC_D^*}}$ [–]	$\Delta C^{off}_{L_{minC_D}}$ [–]	K^* [–]	ΔK^{off} [%]
Exp	0.0143	−16.4	0.0343	−0.007	0.0606	−2.7
VLM	0.0150	0.0	0.0493	0.043	0.0520	−19.3
Patt	0.0167	−2.3	0.0659	0.025	0.0674	+8.2

(b) comparison between blown and unblown wing results

Tab. 2.11: Experimental and numerical drag polar parameters ($J = 1.0$).

Fig. 2.21 and Tab. 2.11 present the drag polars for the advance ratio of 1.0. All the considerations drafted for $J = 0.9$ still applies to this case; however, the

lower $\Delta C_{L_{minC_D}}$ in Tab. 2.11a, confirms the better drag matching at low C_L^* seen in Fig. 2.21.

Also for the blown cases, the deviations highlighted in the results are comparable with those observed by Veldhuis [14].

2.2.6 Additional analysis

Fig. 2.22 helps to understand the reason behind the significant deviations of minimum drag coefficient and concavity between experimental and numerical polars, especially for $J = 0.7$. In the purely VLM approach, modeling the actual aero-propulsive interaction, the complete system numerical forces contain the wing-mounted propeller net thrust. The data reduction, however, relies on the propeller-nacelle assembly net thrust. The two quantities, respectively represented by the dashed and the dash-dotted lines in Fig. 2.22, clearly exhibit opposite trends with respect to AoA. This behavior tends to reduce the effective drag at low α with respect to the actual wing drag, simultaneously increasing the one at higher AoA; the final effect is thus the reduction of $minC_D^*$ and the increase of K^* in numerical polars.

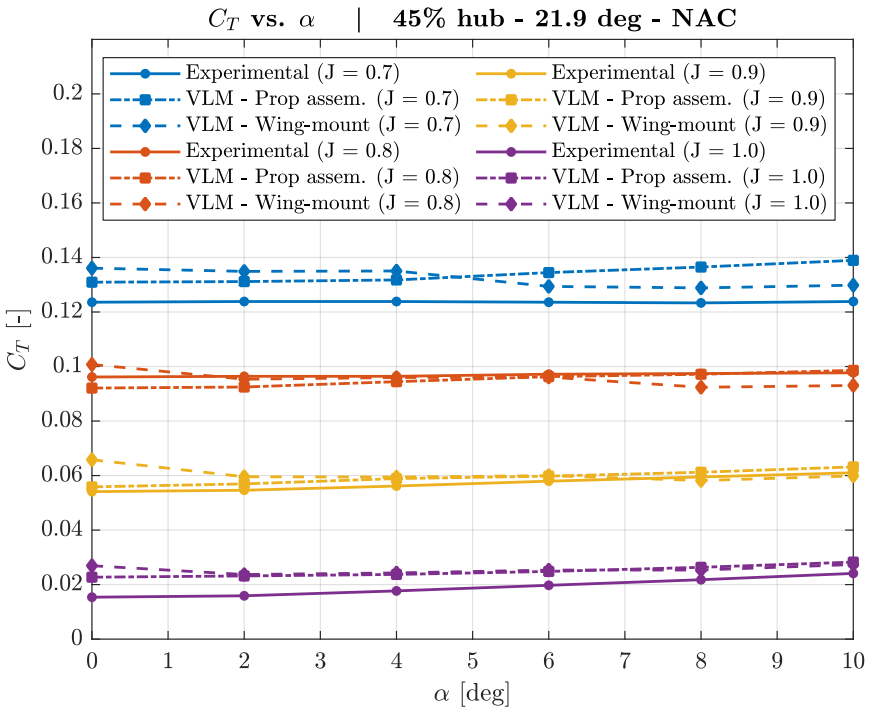

Fig. 2.22: Comparison among experimental sting-mounted net thrust, VLM propeller-nacelle assembly net thrust, and VLM wing-mounted propeller net thrust.

Fig. 2.23 reports an example of the actuator disk approach results, as mentioned at the beginning of this section. The depicted effective drag polars include those computed with the two methods later discarded: LLM and DUST. The considered advance ratio is 0.9, while the AoA ranges from 0° to 6°.

Setting up DUST simulations was not part of this thesis; a visiting Ph.D. student, working on the code and already using Sinnige's data as a reference for his work, kindly provided them in a ready-to-use form. The lack of

resources to solve drag estimation issues, which emerged in the early phases and are visible in Fig. 2.23, led to abandon this approach.

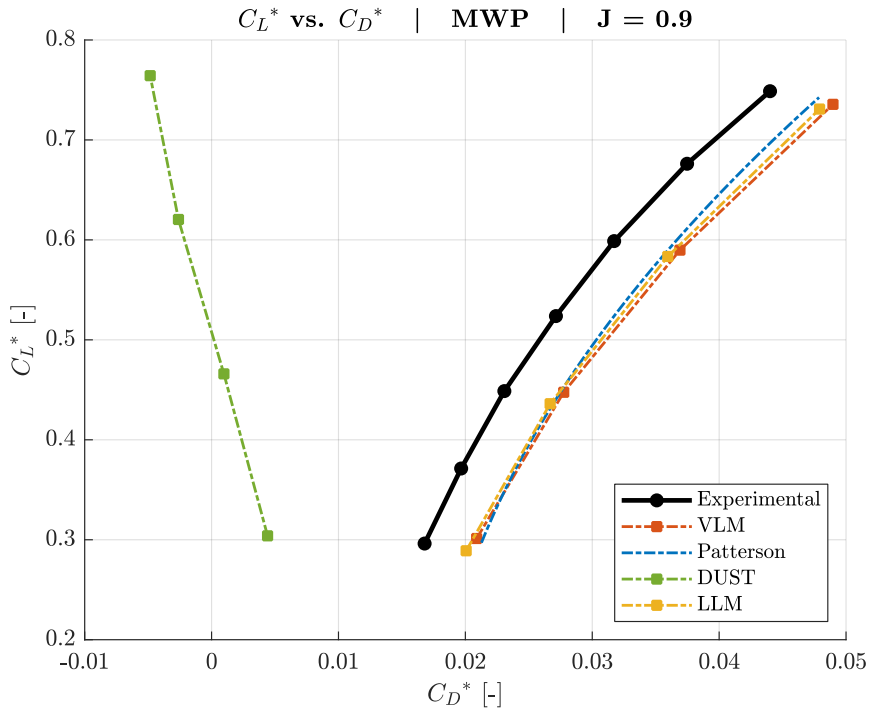

Fig. 2.23: Experimental and numerical drag polars computed using actuator disk approach ($J = 0.9$).

The numerical methods relying on actuator disk theory, i.e., all except DUST, produce polars that exhibit a very close match. No analytic approximation is necessary since the curves are already very smooth. This regularity comes directly from the smoothness of the experimental net thrust measured by Sinnige on the sting-mounted propeller, subsequently used to set up the simulation and reduce the complete system data.

As already pointed out several times, this approach completely neglects the effects induced by the wing on the propeller. In particular, while the numerical results contain the sting-mounted propeller thrust, the complete system forces measured by Sinnige include the actual net thrust of the wing-mounted propeller. Since the actuator disk approach prescribes the same procedure to reduce all the data, no matter their source, the deviation present in the complete system forces directly propagates to the effective coefficients. The result is thus a clear bias between experimental and numerical curves observed in Fig. 2.23.

The results of an additional study, shown in Fig. 2.24, further support the decision to use the purely VLM approach, thus including the complete aero-propulsive interaction in the numerical data. The blockage effect induced by the wing reduces the effective advance ratio seen by the propeller, slightly increasing the thrust coefficient. The experimental data, which contain the wing-mounted propeller thrust, will thus always exhibit a lower effective drag than the numerical polars computed with the actuator disk approach, which instead uses the sting-mounted propeller thrust. Assuming the discrepancies between experimental data and VLM results are entirely related to thrust, Fig. 2.24 shows the values that applied to the actuator disks will have made the

two polars coincide. The large deviations observed on the advance ratios 0.9 and 1.0 highlight how relevant the wing effect on the propeller may be in some cases.

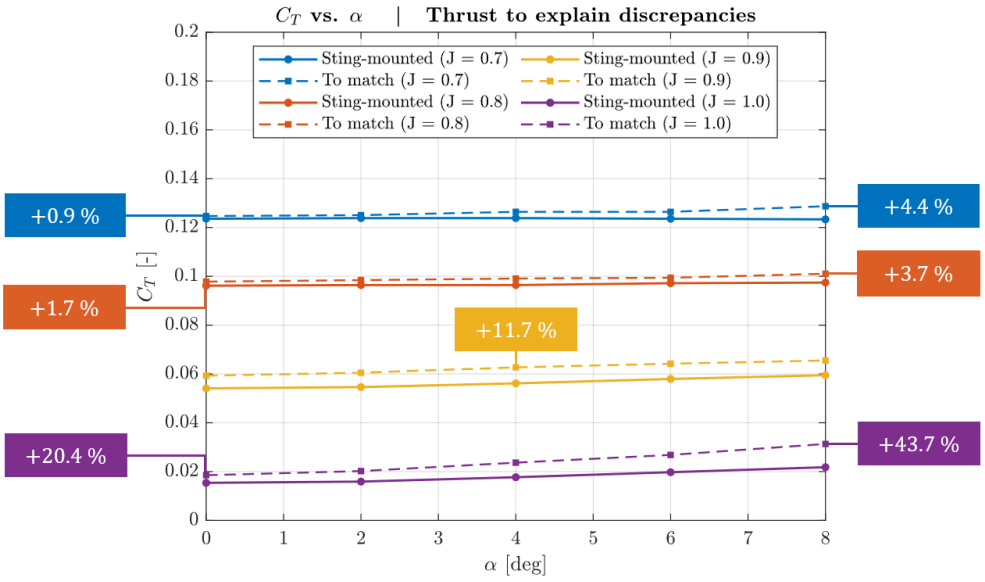

Fig. 2.24: Thrust required to explain the drag discrepancies between VLM results (actuator disk approach) and experimental data.

Appendix A.1 provides additional considerations about the OpenVSP model; for the plots of complete system dimensional forces, the reader may instead refer to Appendix A.2.

Chapter 3

Meta-Model Preliminary Studies

This chapter aims to perform some analyses in preparation for the aero-propulsive meta-model derivation, gaining at the same time more confidence in the selected numerical method. In detail, it extends the previously validated VLM approach to a case featuring multiple propellers and subsequently studies the effects of a partial propellers overlap. Other studies concerning counter-rotating propellers or WTPs are also present.

3.1 Multiple propeller case

Sinnige carried out his experiments on a semi-span wing blown by a single propeller. Before developing a meta-model for Distributed Electric Propulsion, which intrinsically implies the presence of several propellers, it is worth analyzing a multiple propeller case (MPC).

Patterson's method weights the sectional increments of lift and drag produced by each propeller by the corresponding blown surface. Adding identical propellers to a straight and untapered wing will thus lead to a linear increment of blowing effects with the number of operating propellers (n_p).

The present section evaluates how VLM models this proportionality and extends the results to the Wingtip propellers case.

3.1.1 Setup of the simulations

Fig. 3.1 shows the setup used for this study and Tab. 3.1 reports all the details of its geometry alongside the propeller operative conditions. The wing is a stretched version of Sinnige's one: it retains the same chord and airfoil while exhibiting a larger span. Up to 10 evenly spaced propellers are present along the wing leading edge, including two on the wingtip. Tab. 3.2 reports the spanwise position of each couple of propellers, marked with different colors in Fig. 3.1. The solid red line represents the y-axis datum. The propellers are those modeled in OpenVSP for the validation phase. Starting from Sinnige's geometry, they implement all the changes described in Section 2.2.3 to match the experimental net thrust. Nacelles are not present in the model since this analysis does not involve comparing numerical results with experimental data; the additional components will thus increase the computational cost without improving any matching. All the propellers rotate with the inboard blades going up, i.e., in the opposite direction of wingtip vortices.

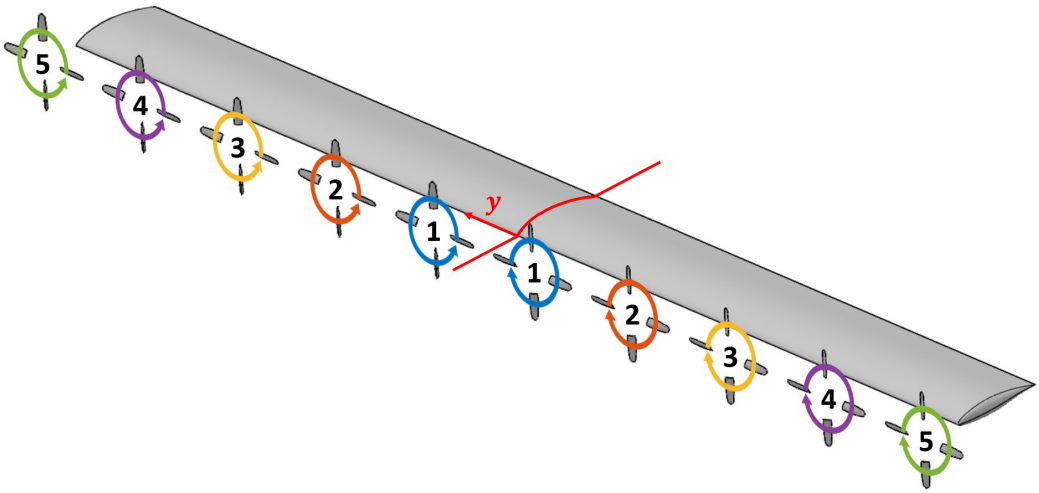

Fig. 3.1: OpenVSP model of the setup used to analyze the multiple propeller case.

Wing	b	2.700 m
	c	0.240 m
	S	0.648 m^2
	AR	11.25
	Λ	0°
	Airfoil	NACA 64_2A615
Propeller	d	0.237 m
	r_h	0.053 m
	$\beta_{3/4}$	21.9°
	N	14466.5 RPM
	J	0.7

Tab. 3.1: Operative conditions and geometry of the wing and the propellers used to analyze the MPC.

ID	$\|Y\|$
1	0.150 m
2	0.450 m
3	0.750 m
4	1.050 m
5	1.350 m

Tab. 3.2: Spanwise position of propeller couples.

3.1.2 Results and analysis

VLM results are available for the isolated wing and five increasingly blown layouts, obtained progressively adding couples of propellers, starting from the 2-prop case, where only the two closer to the wing root are present, up to the 10-prop configuration, which also includes those installed on the wingtips.

Fig. 3.2 shows a portion of the lift coefficient against AoA curves of the five blown configurations. The purely VLM approach tends to underestimate lift at low angles of attack, as already noted during validation. This behavior is not physical and finds no confirmation in experimental data like Sinnige's ones. Apart from those points, the analytic polars approximate well the other results; therefore, all the subsequent evaluations rely on those ideal curves. The limited range of α depicted in Fig. 3.2 is just to improve the plot readability. The analytic expressions fit data points ranging from –8° to +10°.

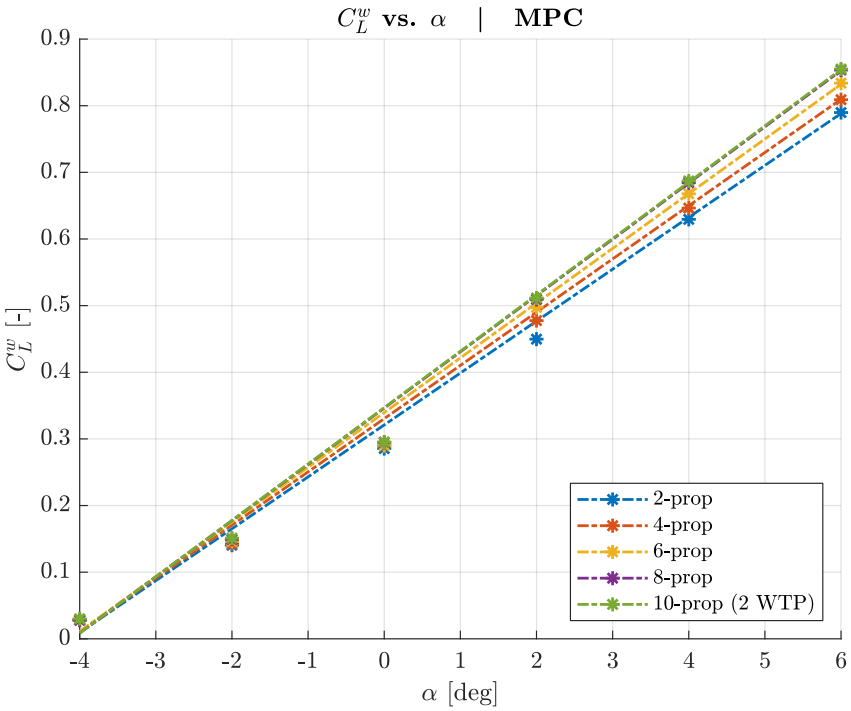

Fig. 3.2: Lift polar of the multiple propeller case wing.

Fig. 3.2 does not report the isolated wing curve. Lift appears higher in this case than in some of the blown ones. The issue is likely related to VSPAero, which uses a steady or an unsteady approach whether or not the propellers are present. However, the regularity of the lift increment produced by each couple of propellers allows extrapolating the unblown wing polars. Further details are available in Section 3.1.3.

The present analysis does not require the reduction procedure described in Section 2.2.4 since no experimental data are available to perform a comparison. Numerical methods allow analyzing each component of the setup individually; this study thus looks exclusively at the forces acting on the wing to derive Patterson-like coefficient deviations. This method partially neglects the complete aero-propulsive coupling, the modeling of which represents the main advantage of the purely VLM approach. Despite not being adequate to derive

the final meta-model, this simplification is sufficient for the present section, which aims to further familiarize with the numerical method.

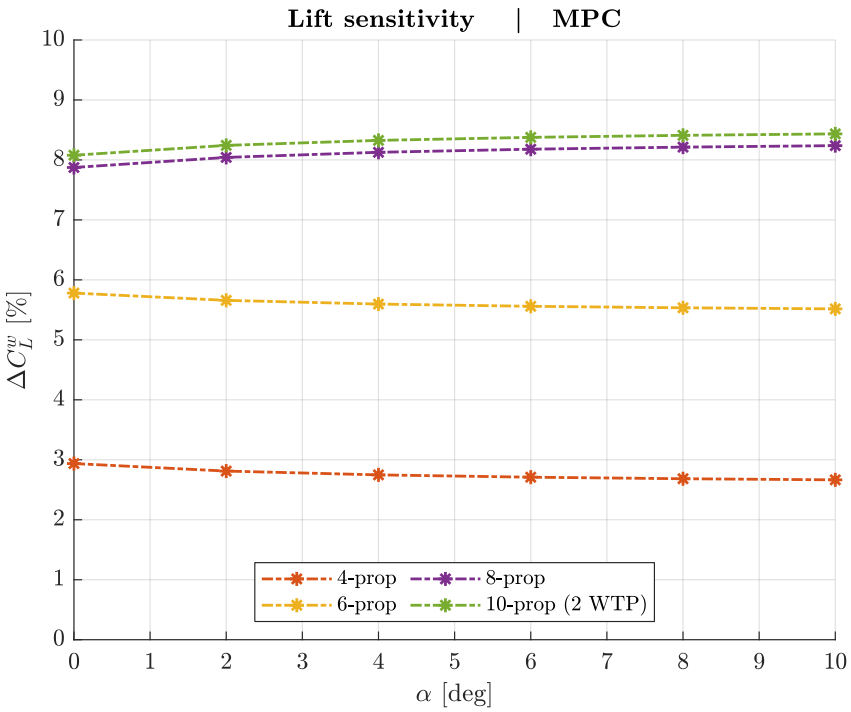

Fig. 3.3: Wing lift relative increment against AoA.

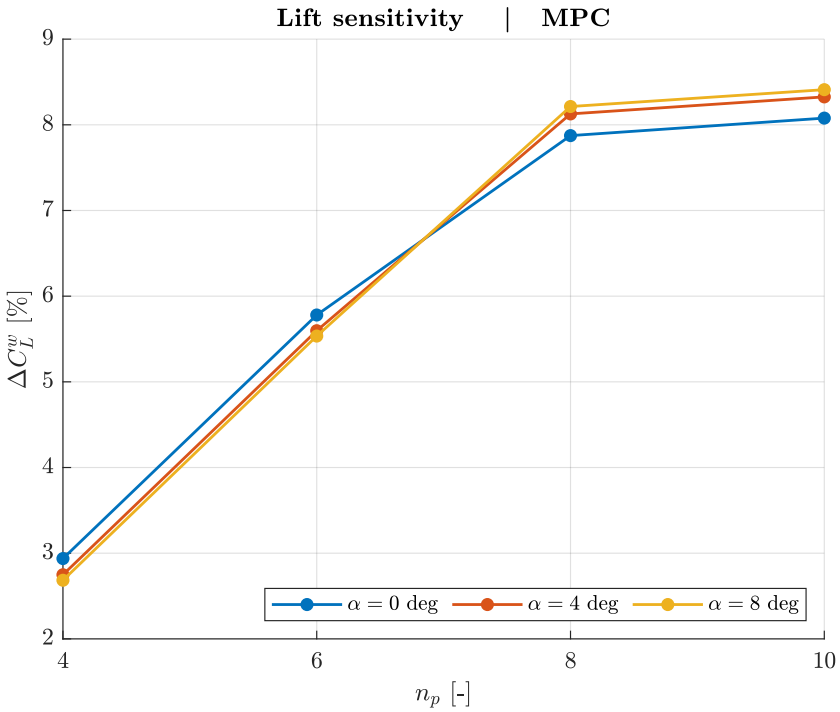

Fig. 3.4: Wing lift relative increment against the number of propellers at different angles of attack.

Fig. 3.3, which shows the wing lift relative increment at each AoA with respect to the 2-prop case, helps quantify the blowing effects already visible in Fig. 3.2. Fig. 3.4, instead, shows the lift relative increment at three different angles of attack while changing the number of propellers.

Both figures highlight a relative increment approximately constant with AoA, i.e., an absolute increment proportional to lift. Up to the 8-prop case, lift regularly increases approximately 2.70% for every added couple of propellers. The WTPs, instead, do not produce any significant variation, i.e., +0.20%. A reduced contribution was forecastable since each WTP only blows half of the span blown by other propellers. Moreover, being relatively small ($d \sim c$), they blow just the very outermost portion of the wing span, the one that provides only a minor contribution to the total lift. If the overall effects appear somehow limited, it is worth recalling that the considered propellers are not specific for DEP applications, and their blowing effectiveness is thus questionable.

In Fig. 3.3, ΔC_L^w appears to converge towards constant values at high angles of attack; this is confirmed by Fig. 3.4, where the red curve exhibits a better match with the yellow one than with the blue. Numerical reasons are likely behind these slight deviations at low AoA: the relative increments computed using a progressively smaller reference amplify absolute discrepancies, which are actually negligible. At –4°, close to the zero-lift AoA, in a portion of the plot not shown in Fig. 3.3, significantly large deviations are present for the same exact reason.

The expression that defines the relative lift increment is the following:

$$\Delta C_L^w = \frac{C_L^w - \widetilde{C_L^w}}{\left|\widetilde{C_L^w}\right|} \tag{3.1}$$

The quantity marked with the tilde is the reference value, represented in this study by the 2-prop case lift coefficient. An analogous expression exists for the drag increment.

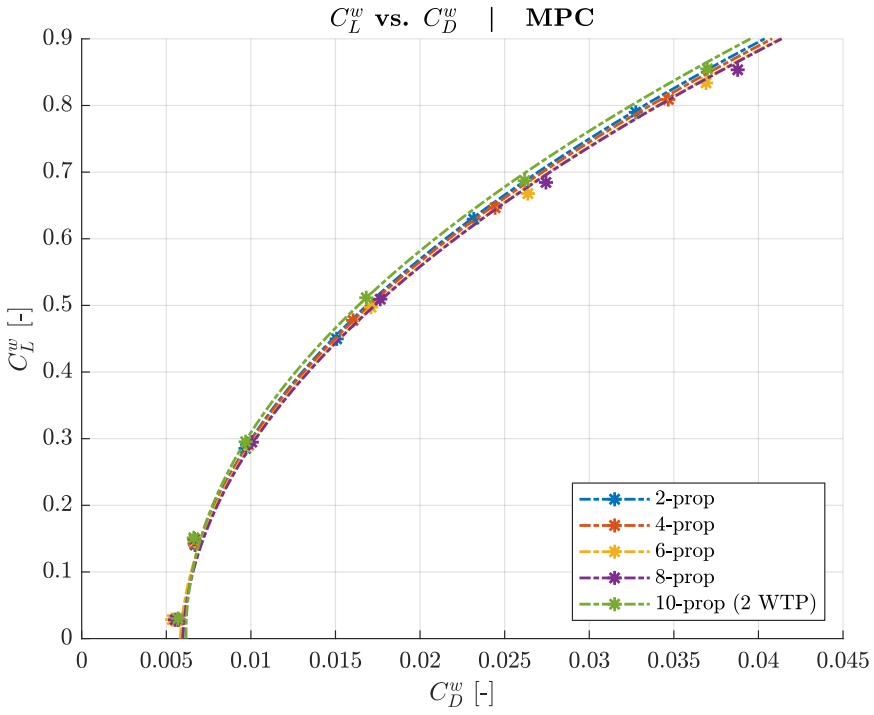

Fig. 3.5: Drag polar of the multiple propeller case wing.

Fig. 3.5 shows a portion of the drag polars of the five blown cases, corresponding to an AoA ranging from –4° to +6°. As for lift: analytic curves are still used instead of the real ones, drag coefficient still refers to the wing contribution, and unblown drag polar is still not present due to its inadequate correlation with the blown ones.

Fig. 3.6 shows the values of the drag polars parameters against the number of propellers; the axis on the right of the plots expresses the same parameters in terms of relative variations with respect to the 2-prop case. Both minimum drag and concavity do not exhibit any specific trend, and variations are almost negligible, i.e., limited to a few percent. On the other hand, the lift coefficient associated with minimum drag shows considerable variations, ranging from –88% to +140%. In particular, it decreases adding more propellers but finally raises significantly with WTPs. Therefore, as clearly visible in Fig. 3.5, for a given C_L^w, the case including WTPs exhibits the lowest corresponding C_D^w.

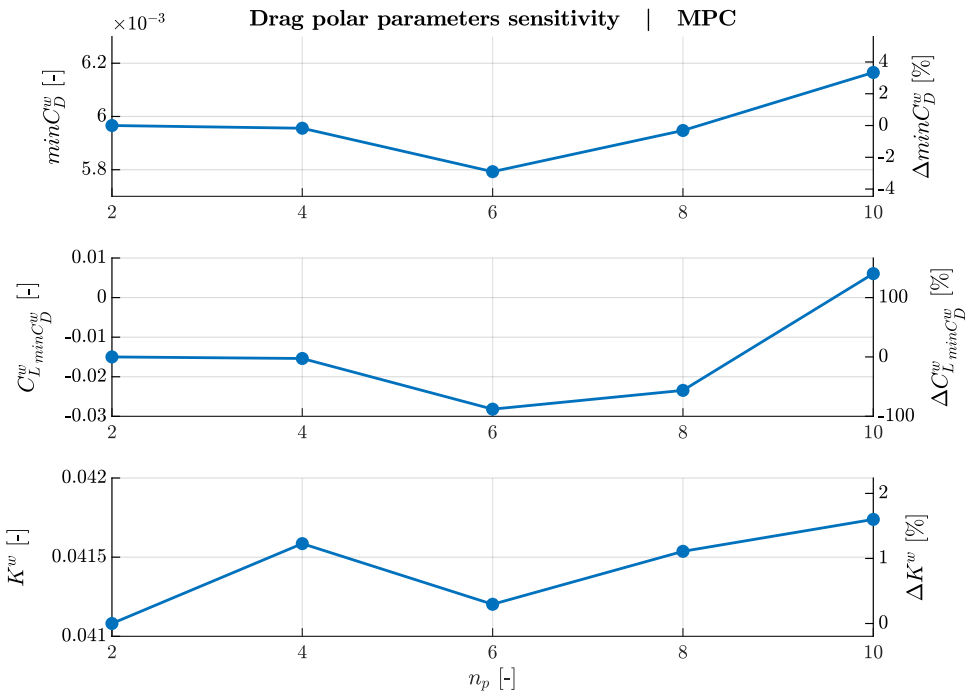

Fig. 3.6: Drag polars parameters against the number of propellers.

Fig. 3.7 illustrates the relative drag increment at each AoA with respect to the 2-prop case. Contrary to what happens to lift, the drag increment is not constant with the angle of attack. Up to the 8-prop layout, drag regularly increases with the number of propellers. On the other hand, the 10-prop configuration, which includes WTPs, exhibits a sharp drag reduction with respect to the 8-prop case.

The quadratic approximation of the relative drag increment produced by each couple of additional propellers, except the WTPs, has the following expression:

$$\Delta C_D^w = -0.00031\alpha^2 + 0.0056\alpha + 0.033 \qquad (3.2)$$

The increment induced by WTPs, shown instead by the equation below, is negative and thus represents a decrement of the wing drag.

$$\Delta C_D^w = +0.00023\alpha^2 - 0.00017\alpha - 0.059 \quad (3.3)$$

Appendix B.1 provides additional information about the derivation of a model for coefficient deviations.

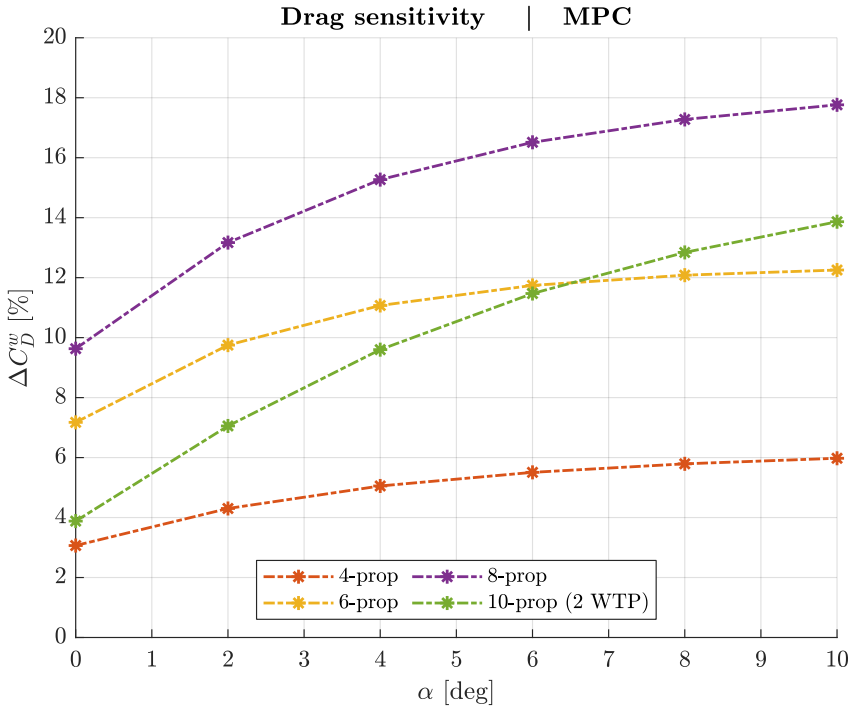

Fig. 3.7: Wing drag relative increment against AoA.

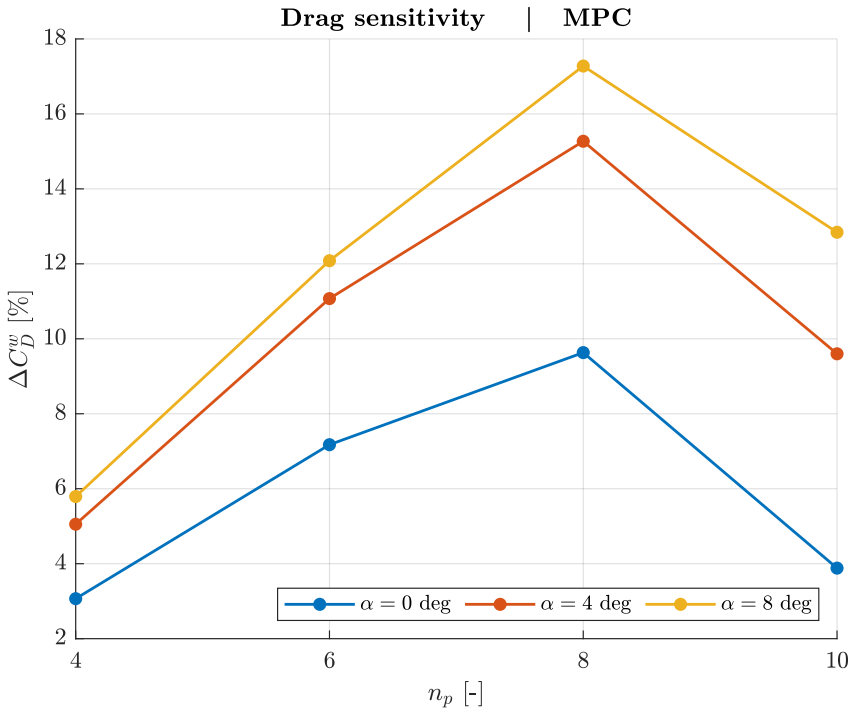

Fig. 3.8: Wing drag relative increment against the number of propellers at different angles of attack.

Fig. 3.8 highlights the approximately regular drag increase with the number of propellers followed by the significant drop related to the addition of the WTPs. The three non-coincident lines confirm that, as already noted, the relative variations change with AoA.

In conclusion, lift and drag increments are almost linear with the number of propellers, at least up to the 8-prop layout. The overall effect of a certain number of propellers is thus nothing more than the same number of times the contribution of a single one. This result can significantly reduce the computational cost required to analyze configurations featuring several identical DEP propellers, especially in the context of an extensive numerical campaign. This result is not fully general since the setup considered in this study presents neither twist nor taper. However, analyzing a limited set of configurations, possibly with a few propellers, may still be sufficient to derive a model for the single propeller contribution, even on more complex geometries. Moreover, it is possible to extend some conclusions drafted in this study to more sophisticated cases. From a broader perspective, for example, the MPC analysis showed that the spanwise position of the propeller has negligible effects on the increments of the coefficients.

Fig. 3.9 and Fig. 3.10 show the extended versions of the lift and drag polars, with the AoA ranging from –8° to +10°, better highlighting some of the aspects noted above. The lift curve slope in Fig. 3.9, for example, increases with the number of operating propellers while the zero-lift AoA remains almost unchanged. The effect of blowing is thus the reduction of the lift coefficient at angles of attack lower than α_0.

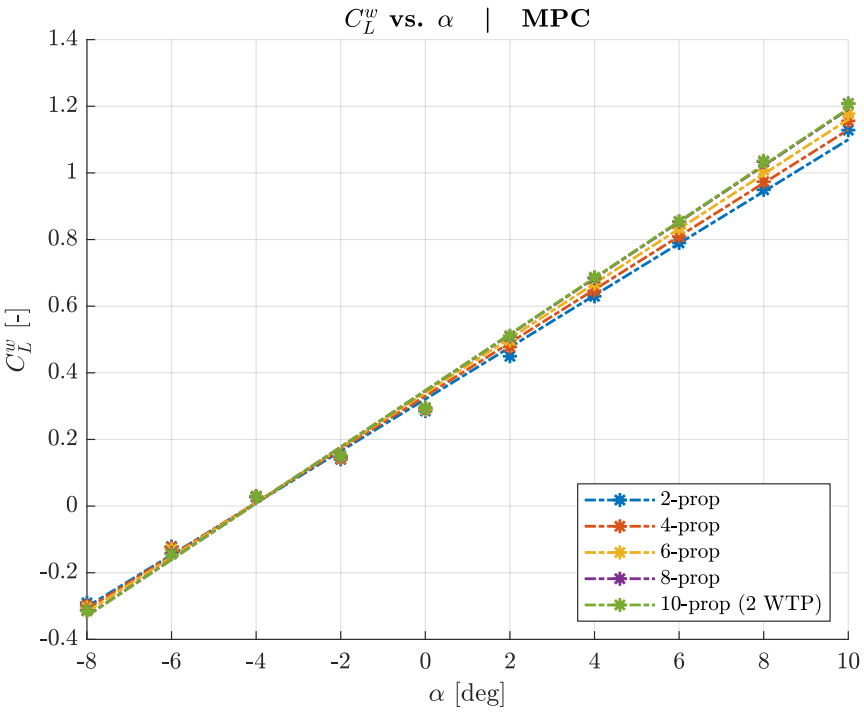

Fig. 3.9: Extended lift polar of the multiple propeller case wing.

Fig. 3.10 qualitatively shows what Fig. 3.6 already quantified more precisely: the blowing effects on polar concavity and minimum drag coefficient are negligible, while WTPs produce a sharp reduction in $C^w_{LminC_D^w}$.

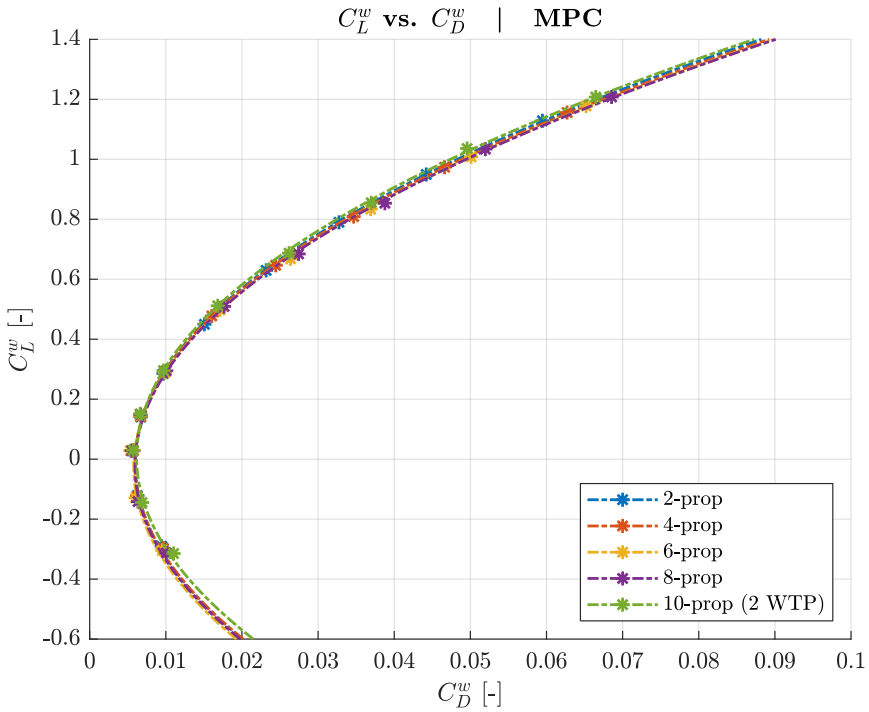

Fig. 3.10: Extended drag polar of the multiple propeller case wing.

3.1.3 Extrapolation of the unblown wing polar

Given the regularity of the increments of both lift and drag coefficients, it is possible to extrapolate the polars of the unblown wing starting from the deviations computed in Section 3.1.2.

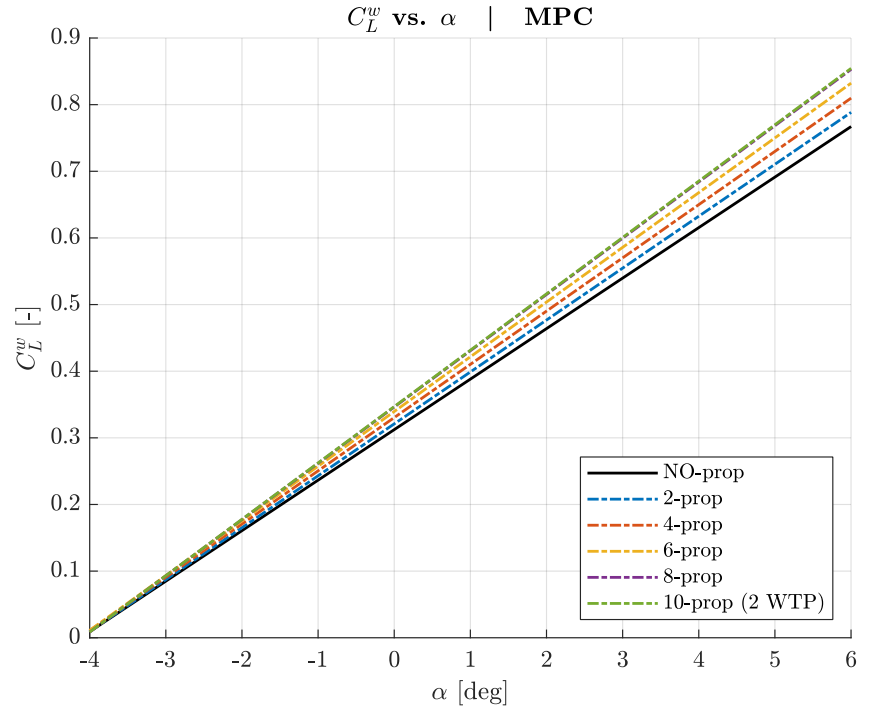

Fig. 3.11: Lift polar of the multiple propeller case wing (including the unblown configuration).

Fig. 3.11 and Fig. 3.12 illustrate the lift and drag analytic polars of the MPC, obtained subtracting from the curves of the 2-prop case the previously identified increments.

It is now possible to redefine the models of ΔC_L^w and ΔC_D^w using these newly computed baseline references, thus obtaining a Patterson-like approach that provides deviations from the unblown configuration coefficients. Any preliminary sizing routine with a reliable and well-proven method for the aerodynamic analysis of the unblown wing can then integrate this plug-in procedure and compute the blown wings coefficients. The following equations are the expressions of the lift and drag relative increments produced by each couple of propellers (excluding the WTPs):

$$\Delta C_L^w = +0.0278 \tag{3.4}$$

$$\Delta C_D^w = -0.00035\alpha^2 + 0.0063\alpha + 0.033 \tag{3.5}$$

The equations below are instead the expressions of the lift and drag relative increments produced by the wingtip propellers:

$$\Delta C_L^w = +0.0020 \tag{3.6}$$

$$\Delta C_D^w = +0.00027\alpha^2 - 0.00058\alpha - 0.061 \tag{3.7}$$

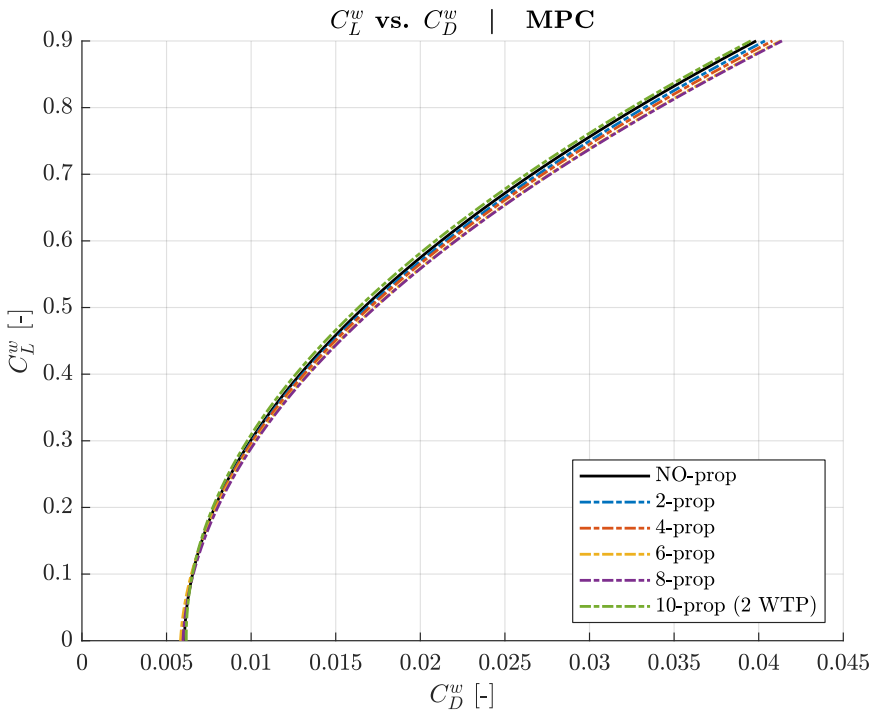

Fig. 3.12: Drag polar of the multiple propeller case wing (including the unblown configuration).

3.2 Overlapping propeller case

DEP propellers ideally have to blow the entire wing surface to maximize lift augmentation. Many distributed propulsion concepts thus feature a dense distribution of propellers, sometimes even partially overlapping with each

other. The present section aims to evaluate the effect of the propeller overlapping using the previously validated purely VLM approach.

The analysis of the multiple propeller case quantified the lift and the drag coefficient increments produced by each couple of additional propellers. The actual values of these increments are specific to the setup geometry and the propeller operational conditions. The effects of the wing taper and twist are somehow predictable since they directly impact the parameters of the constitutive equations of both lift and drag. On the other hand, the effects of other factors, such as the spacing between the propellers, require additional investigation. Varying the distance that separates the propellers, and thus their slipstreams, the increments previously quantified in the MPC study may change, even if they remain linear with the number of propellers.

3.2.1 Propeller proximity analysis

The MPC setup, described in Section 3.1.1, presents evenly spaced propellers, mounted every 0.300 m and covering the entire wingspan. Given the propeller diameter of 0.237 m, the clearance between each propeller is 0.063 m, i.e., 53% of the propeller radius.

The present study uses a modified version of the 4-prop layout; this setup minimizes the computational cost, featuring only two propellers on each wing, the minimum required to perform such analysis. Moving the inboard and the outboard propellers 0.025 m towards each other, the gap between the two reduces to 0.013 m, i.e., 11% of the propeller radius, almost a fifth of the original clearance.

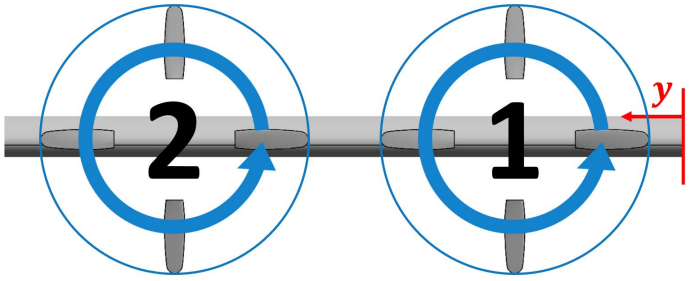

(a) nominal clearance

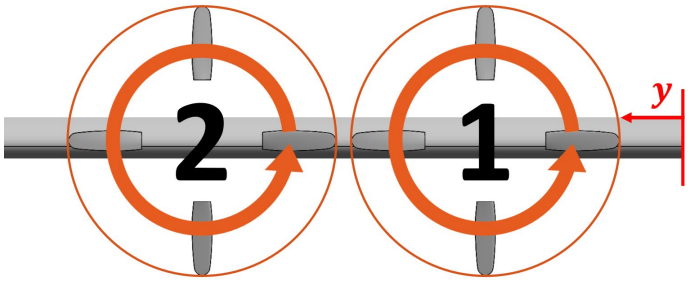

(b) reduced clearance

Fig. 3.13: 4-prop setups with nominal and reduced clearance.

Fig. 3.13 compares the two setups: the original one, with the nominal separation between the propellers, and the modified one, featuring the reduced clearance. To better show the difference between the layouts, the figure only depicts the portion of the wing where the propellers are present, i.e., the one

from the plane of symmetry to $Y = 0.600$ m. As in the MPC, the propellers spin in the inboard-up direction.

Tab. 3.3 specify the spanwise position of the two couples of propellers in the considered layouts. As already stated, both propellers move 0.025 m towards each other to reduce the gap.

Clearance	$\lvert Y_1 \rvert$	$\lvert Y_2 \rvert$
53%R	0.150 m	0.175 m
11%R	0.450 m	0.425 m

Tab. 3.3: Spanwise position of propeller couples (proximity analysis).

Fig. 3.14 compares the lift polars of the original 4-prop configuration and the modified setup. Despite the reduced clearance, the discrepancies are negligible, and the two curves in the plot appear coincident. Concerning the data points individually and excluding those at near-zero lift, the deviations are relatively random and remain within the ±0.4% range, with an average value of just –0.07%. The analytic polar filters well the randomicity of the data points and thus presents almost no deviation.

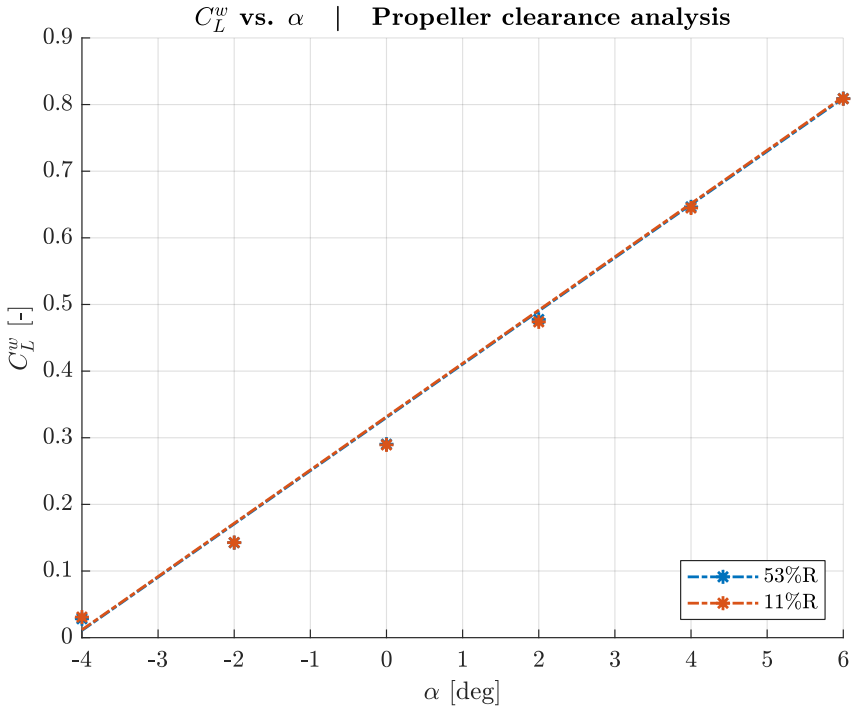

Fig. 3.14: Lift polar with both nominal and reduced propeller clearance.

Fig. 3.15 shows the drag polars of the original 4-prop configuration and the modified setup. The deviations, also for drag, are random and almost negligible. The relative discrepancies and their average value are higher than those computed on the lift; this, however, is in line with a reference that is an order of magnitude lower. The analytic curves show no significant discrepancies and appear nearly coincident, even when zooming on a limited portion of the plot, like in Fig. 3.15.

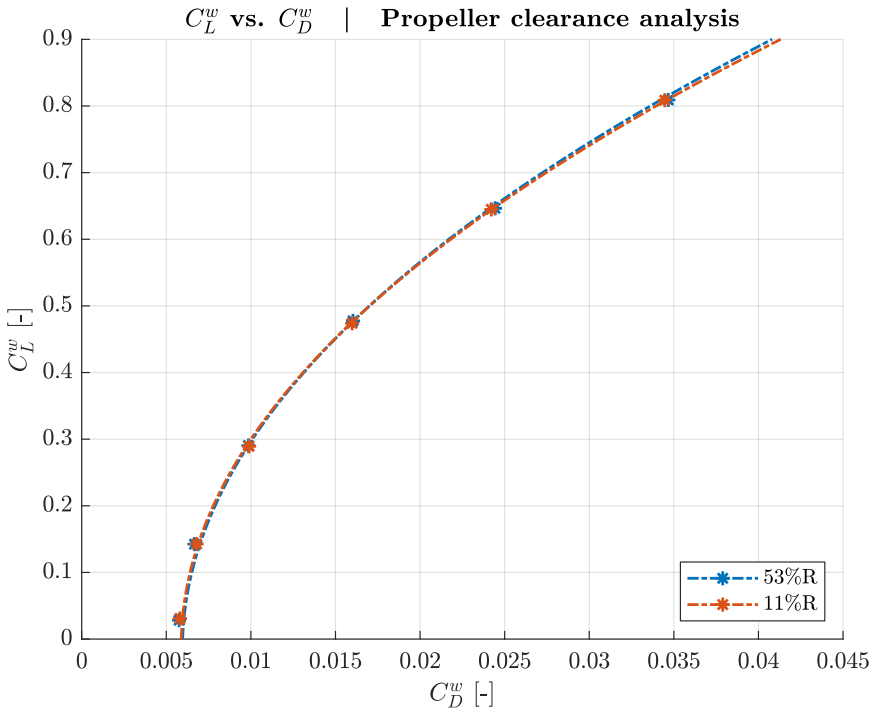

Fig. 3.15: Drag polar with both nominal and reduced propeller clearance.

3.2.2 Propeller overlapping analysis

The 4-prop layout of the MPC is not adequate to perform this analysis. Since the propellers share the same axial position, i.e., $X_1 = X_2$, proceeding as in Section 3.2.1 will eventually result in the two propeller disks intersecting. The present simulations thus rely on a new setup featuring four staggered propellers, two on each wing.

This study aims to understand the effect on lift and drag of a partial propeller overlapping, progressively moving the outboard propellers toward the inboard ones, which instead remain fixed. The inboard couple is at 0.250 m from the plane of symmetry, while the outboard one moves from $Y = 0.546$ m (50%R clearance layout) to $Y = 0.428$ m (50%R overlap layout). On the other hand, the axial position of the two couples remains the same for all the considered configurations: 0.104 m upwind of the wing leading edge for the inboard propellers, and 0.050 m for the outboard ones. Tab. 3.4 specifies both the axial and spanwise position of the two propeller couples for all the three configurations considered in this test.

Case	X_1	$\lvert Y_1 \rvert$	X_2	$\lvert Y_2 \rvert$
50%R clearance	0.104 m	0.250 m	0.050 m	0.546 m
0%R clearance	0.104 m	0.250 m	0.050 m	0.487 m
50% overlap	0.104 m	0.250 m	0.050 m	0.428 m

Tab. 3.4: Axial and spanwise position of propeller couples (overlapping analysis).

Fig. 3.16 depicts the top-view of a portion of the setup used in this study, more precisely in the 50%R overlap case, from the plane of symmetry to $Y = 0.678$ m. The picture gives an idea of the propellers position and blown surfaces, highlighting the region where their slipstreams overlap.

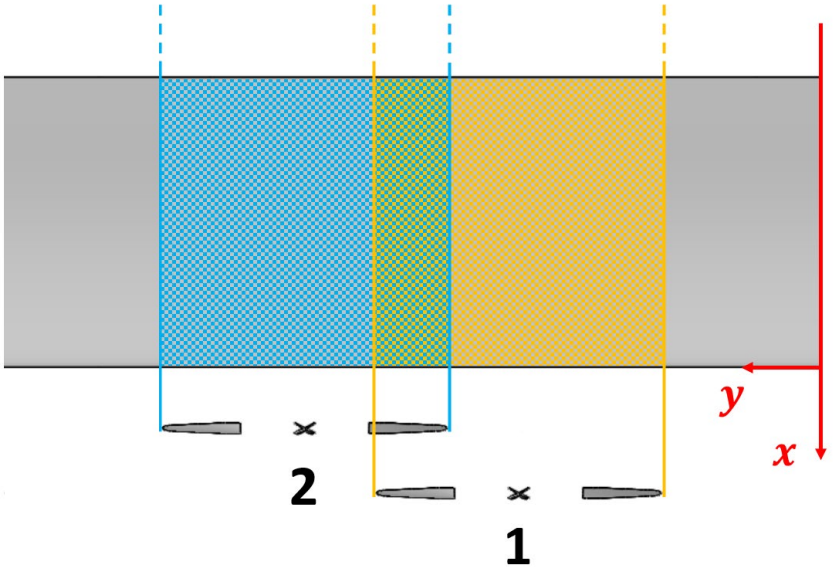

Fig. 3.16: Top-view of a wing portion of the OPC setup.

Whenever two propellers overlap, the reduced blown surface has a negative impact on the lift increment; on the other hand, the increased dynamic pressure in the region blown by both propellers raises the local lift. The two effects counteract each other and produce a negligible total effect, well explained by the three almost coincident analytical curves of Fig. 3.17.

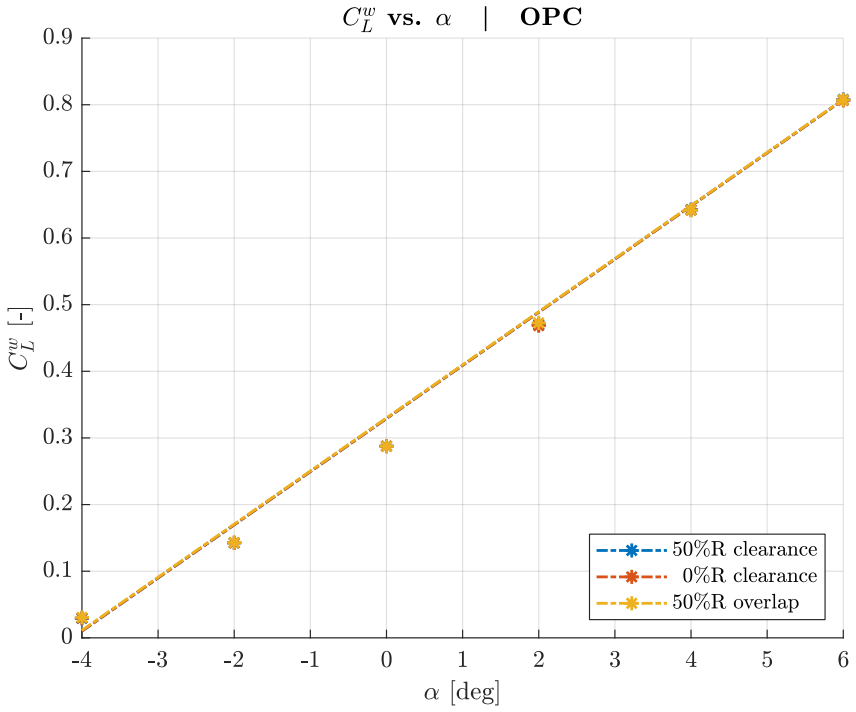

Fig. 3.17: Lift polar of the overlapping propeller case wing.

Fig. 3.18 shows the relative deviations of the lift coefficient with respect to the 50%R clearance configuration, representing the reference case. Removing the gap between the propeller does not affect the lift relative increment, and even a significant overlapping produces almost negligible deviations compared to the total lift increase produced by the four well-spaced propellers (5.56%).

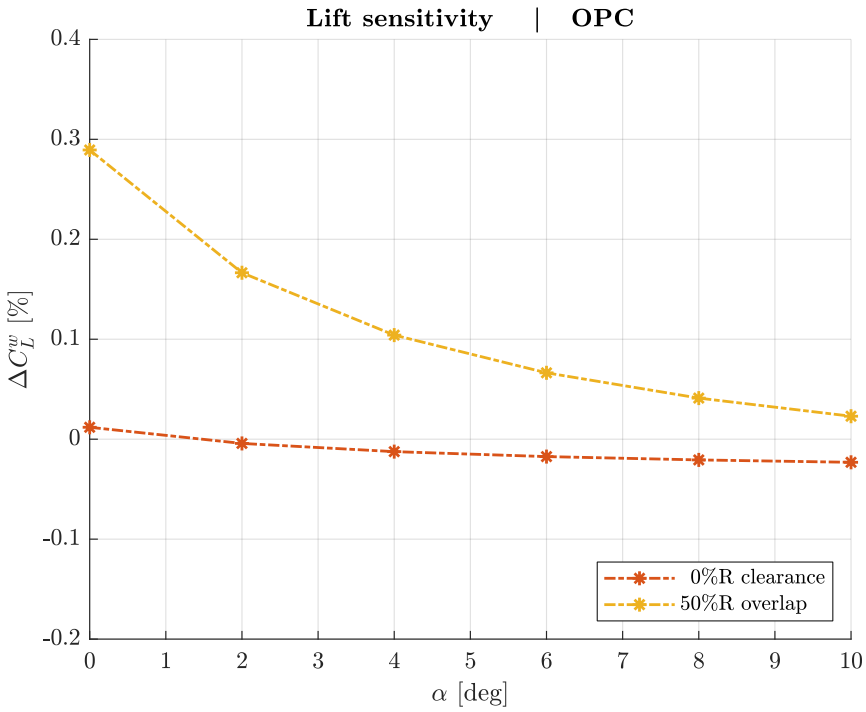

Fig. 3.18: Wing lift relative increment against AoA (OPC).

According to the present study, even if the wing is already entirely blown, an additional couple of propellers will further augment its lift. To maintain the propellers evenly spaced spanwise, they will partially overlap. Although the blown surface will not change, the dynamic pressure will increase on the wing portions behind where the propellers overlap. The penalty is a slight reduction, 0.4% on average, of the thrust coefficient with respect to the case without overlapping.

In conclusion, the contribution to the total lift of a new couple of propellers is still the one computed in the MPC, no matter if they partially overlap. Moreover, the present analysis cleared the purely VLM approach from possible numerical issues related to overlapping propellers. However, since no experimental data are available for validation, extending these results to cases featuring large overlapping regions may lead to inaccurate estimates of the lift coefficient increment.

Fig. 3.19 illustrates the drag polars of the three considered configurations. The overlapping effects are almost negligible even on the drag coefficient; the analytic curve of the case featuring the 50%R overlap is coincident with the one exhibiting the 50%R gap. The case without either clearance or overlap shows a slight deviation towards lower drag. Since the proximity analysis of Section 3.2.1 did not highlight any significant drag deviation when reducing the distance between the propellers, the discrepancy is thus likely related to some minor numerical issues occurring when the propeller slipstream touch.

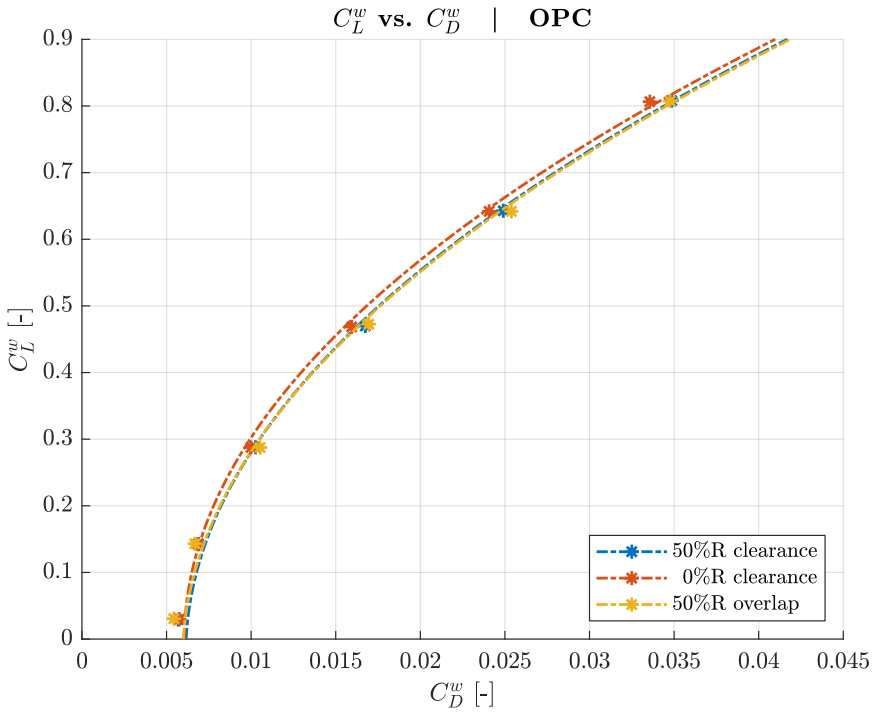

Fig. 3.19: Drag polar of the overlapping propeller case wing.

Fig. 3.20 presents the drag coefficient relative deviations with respect to the case with a 50%R clearance between the propellers. The red curve, associated with the zero-gap configuration, exhibits the already described large discrepancy. The yellow line shows instead the small drag increment produced by the layout with the overlapping propellers.

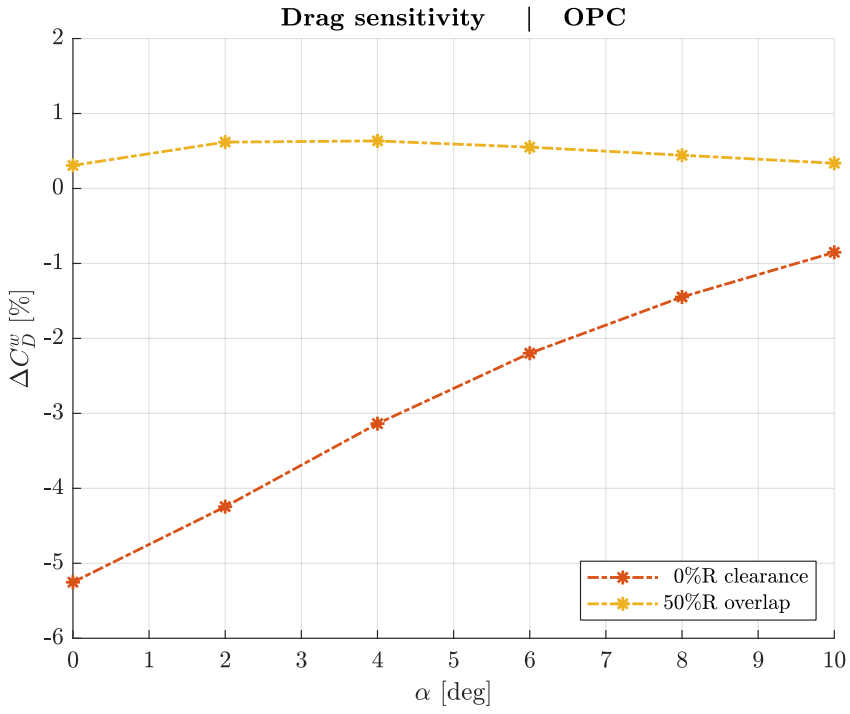

Fig. 3.20: Wing drag relative increment against AoA (OPC).

The slightly increased lift and drag coefficients, in the 50%R overlap case, are the results of the increased dynamic pressure, the effects of which successfully overcome those of the reduced blown surface.

In conclusion, no significant overlapping effects emerge from this study; the lift and drag increments computed on the MPC setup are thus valid also when a moderate propeller overlapping is present.

3.3 Additional studies

This section investigates some additional aspects related to the multiple propeller case. First of all, it better quantifies the effects of WTPs, the use of which to reduce induced drag may be interesting also in the cruise phase. Secondly, it analyses a case in which adjacent propellers spin in the opposite direction, trying to assess the benefits of such configuration.

3.3.1 Wingtip propellers

As shown in Section 3.1.2, WTPs exhibit almost negligible effects in terms of lift augmentation compared to the other HLPs. Their ability to counteract the wingtip vortices, on the other hand, has proven effective in reducing the lift-induced drag, to the point that some DEP concepts, including NASA X-57 Maxwell [4], take advantage of this phenomenon operating WTPs even during the cruise phase.

To better understand the effects of WTPs, especially their benefits when spinning in the opposite direction of wingtip vortices, Fig. 3.21 and Fig. 3.22 compare the polars of the original 2-prop configuration, which operates only the two innermost propellers, with those of a setup featuring only the two WTPs. Tab. 3.5 reports the values of all the parameters that describe the analytic polars.

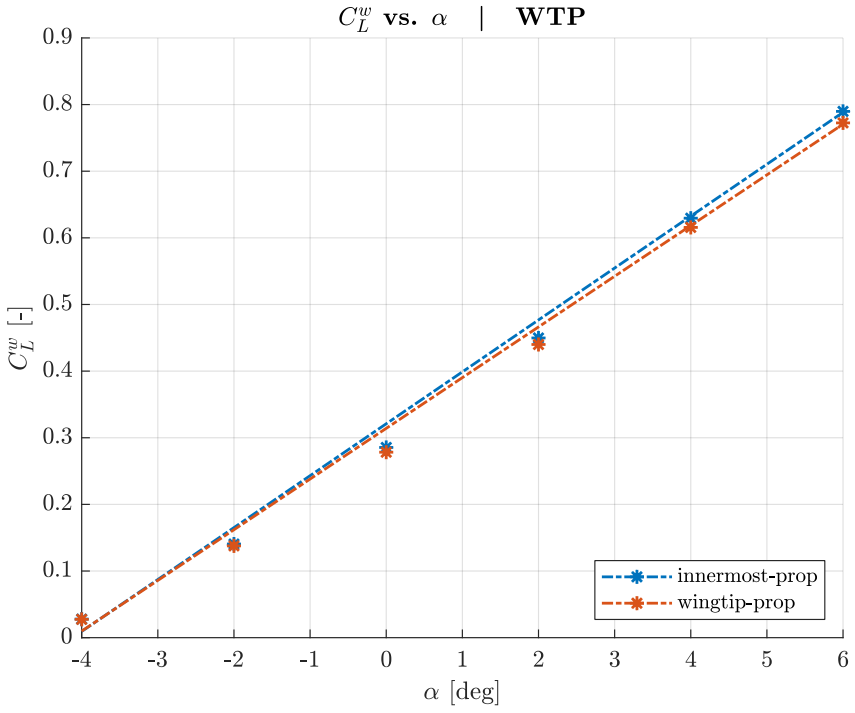

Fig. 3.21: Lift polar of the WTP case wing.

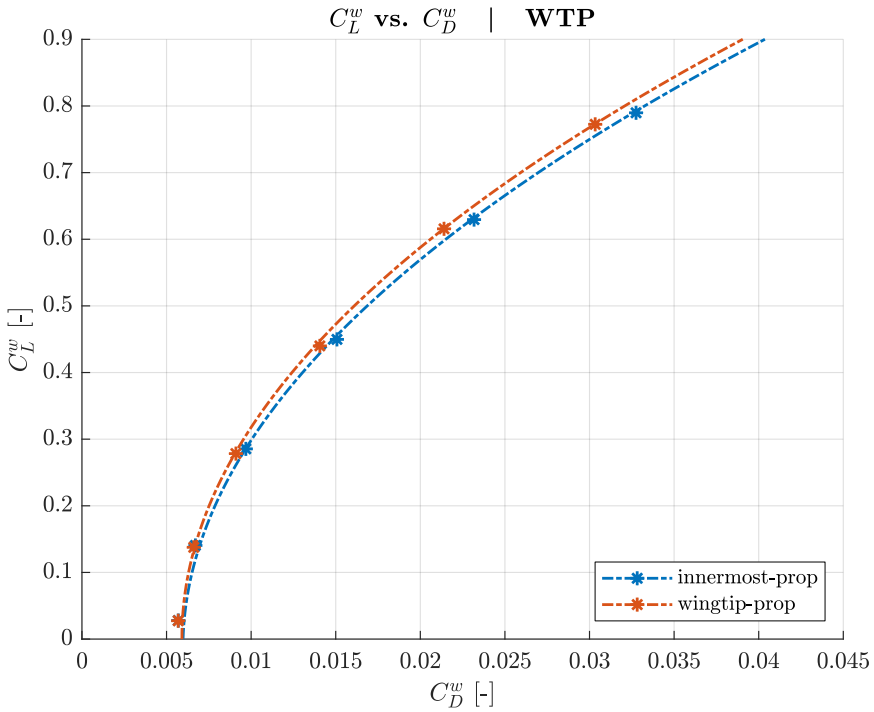

Fig. 3.22: Drag polar of the WTP case wing.

As already observed in Section 3.1.2, the blowing effects do not produce any significant variation in zero-lift AoA, minimum drag coefficient, and drag polar concavity. The most substantial deviations are those on the lift curve slope and the lift coefficient associated with the minimum drag. Consequently, the discrepancies between the original 2-prop configuration and the WTP case are more appreciable on these two parameters.

	$C_{L_\alpha}^w$ [deg $^{-1}$]	α_0^w [deg]
innermost-prop	0.0779	−4.1203
wingtip-prop	0.0761 (−2.3%)	−4.1294 (−0.2%)

(a) lift polar parameters

	$minC_D^w$ [−]	$C_{L_{minC_D^w}}^w$ [−]	K^w [−]
innermost-prop	0.0066	−0.0150	0.0411
wingtip-prop	0.0059 (−11%)	0.0024 (+116%)	0.0411 (+0%)

(b) drag polar parameters

Tab. 3.5: Polar parameters of the WTP and the original 2-prop case.

In Fig. 3.21, the lift curve of the WTP layout is relatively less steep, as confirmed by the C_{L_α} value in Tab. 3.5a, about 2.3% lower than the one observed in the 2-prop case. Fig. 3.22 shows a WTP polar slightly shifted towards higher

C_L with respect to the wing mounting the two propellers in the innermost position. The sharp increase of the lift coefficient associated with minimum drag in Tab. 3.5b confirms the latter observation.

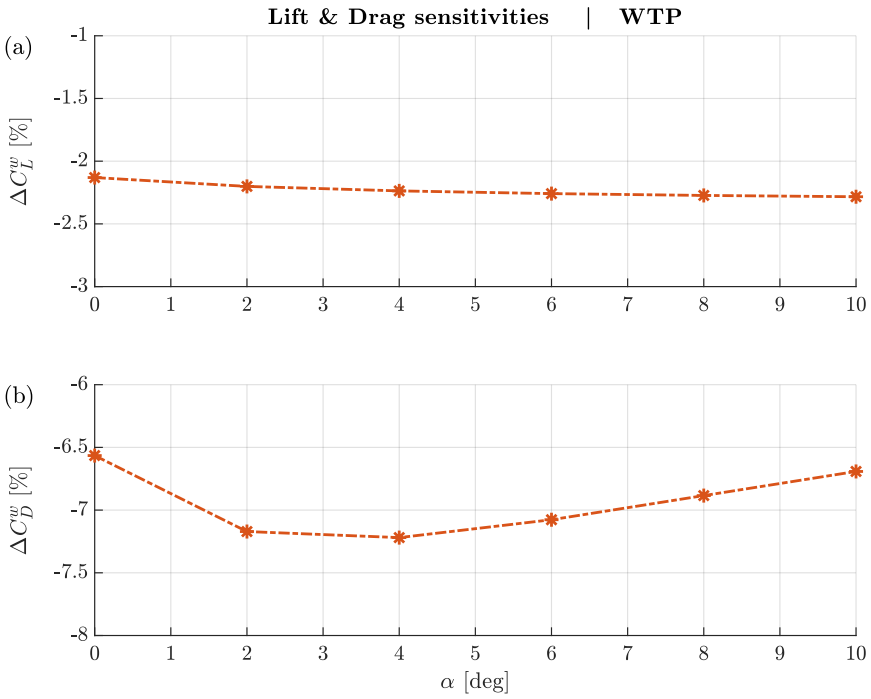

Fig. 3.23: Wing lift and drag relative deviations against AoA (WTP).

Fig. 3.23 presents the relative deviations of lift and drag coefficient at different angles of attack. The original 2-prop case still represents the reference to compute the discrepancies. Fig. 3.23a shows that the lift coefficient of the setup mounting the WTPs is, on average, 2.23% lower than the reference one. This data is in line with those gathered and analyzed in Section 3.1.2, which quantified the lift increments produced by non-WTP and by WTP propeller couples in a +2.70% and a +0.20% with respect to the 2-prop configuration. Fig. 3.23b highlights the main benefit offered by WTPs, a significant reduction in drag: –6.93% on average. Approximating the drag discrepancy as a quadratic function of the AoA, as done in Section 3.1.2, its expression is the following:

$$\Delta C_D^w = +0.00022\alpha^2 - 0.0022\alpha - 0.066 \tag{3.8}$$

Although the matching is good, for a better result, especially on a wider range of angles of attack, one may consider using a more complex model. Appendix B.1, for example, presents a 2nd-degree rational function of α as the ideal model for drag relative discrepancy.

3.3.2 Counter-rotating propellers

Some twin-engine aircraft operate counter-rotating propellers that balance effects like torque and P-factor spinning in opposite directions. Airbus A400M [25], a large military transport aircraft equipped with four turboprops engines, two on each wing, brings this concept to another level: even the two propellers mounted on the same wing spin in opposite directions. Gearboxes, necessary to invert the propeller spin rotation while keeping the engine design unique,

imply additional weight, costs, and complexity. The gain in terms of aerodynamics must be significant to justify this choice; further analysis of the MPC setup may thus be worthful. Moreover, considering that inverting the spin direction of a propeller connected to an electric motor does not require any gearbox, even smaller gains may be beneficial.

The layout used for this test is the 10-prop configuration. In the MPC simulations, the propellers placed on the right wing already spin in the opposite direction of those mounted on the left one. The present section compares this original configuration, with all the propellers on the same wing spinning in the same direction, with a novel case, where all the propellers spin in the opposite direction of the adjacent ones. Co-rotating and counter-rotating are the labels respectively attributed to the two configurations.

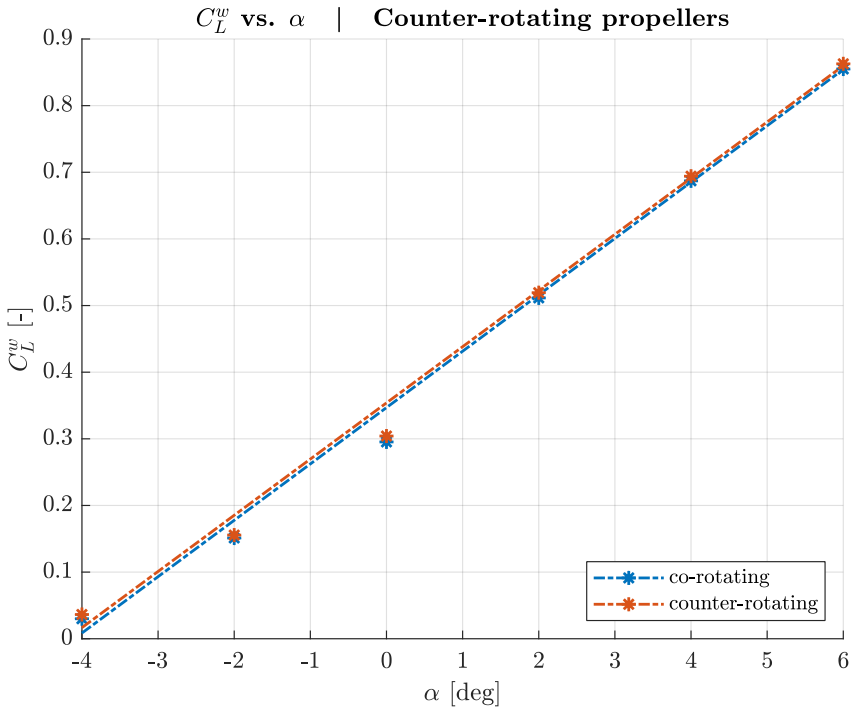

Fig. 3.24: Lift polar of the CRP case wing.

Fig. 3.24 and Fig. 3.25 present the lift and drag polars of both the co-rotating and the counter-rotating case. The lift coefficient slightly increases thanks to the counter-rotating configuration, especially at low angles of attack. The deviation, however, is marginal, ranging from +0.0092 to +0.0044. Moreover, it does not follow the usual behavior noticed in the previous studies, i.e., an almost constant α_0^w and an increasingly steep slope. The curve actually slightly shifts toward higher C_L, with an almost constan slope and a slighly lower α_0^w. Tab. 3.6a reports the values of all the lift curve parameters.

The main benefit of the counter-rotating layout is the drag reduction, appreciable in Fig. 3.25 and quantified by the values in Tab. 3.6b. Despite the slightly higher K^w (+2.4%), the lower minimum drag coefficient (–6.5%) combined with the higher $C_{L_{minc_D^w}}^w$ are able to reduce C_D, especially at low α.

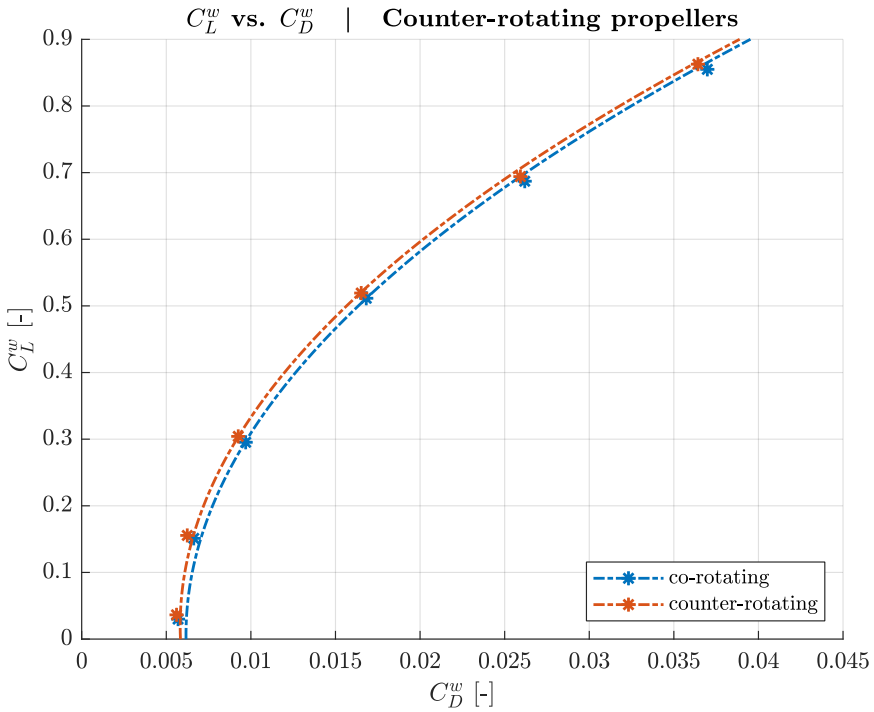

Fig. 3.25: Drag polar of the CRP case wing.

	$C_{L_\alpha}^w$ [deg $^{-1}$]	α_0^w [deg]
co-rotating	0.0846	−4.1012
counter-rotating	0.0843 (−0.4%)	−4.1975 (−2.3%)

(a) lift polar parameters

	$minC_D^w$ [−]	$C_{L_{minC_D^w}}^w$ [−]	K^w [−]
co-rotating	0.0062	0.0060	0.0417
counter-rotating	0.0058 (−6.5%)	0.0200 (+233%)	0.0427 (+2.4%)

(b) drag polar parameters

Tab. 3.6: Polar parameters of the CRP and the original 10-prop case.

Fig. 3.26 illustrates the lift and drag relative discrepancies at different angles of attack; it compares the coefficients of the counter-rotating layout with those of the standard co-rotating one. The small reference values at low AoA amplify the relative deviations; however, the benefits of operating propellers in the counter-rotating configuration remain marginal. Nevertheless, since inverting the direction in which an electric motor spins does not imply any significant drawback, implementing a counter-rotating layout may further exploit the advantages of wing blowing. Finally, it is worth recalling that the considered

propellers are not optimized for DEP; a specific design for lift augmentation may lead to more significant advantages.

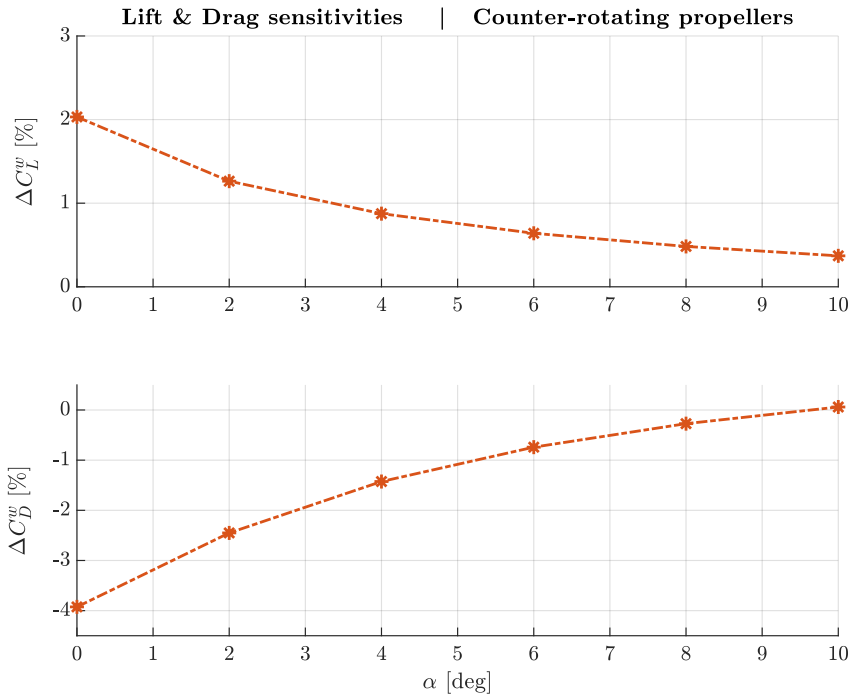

Fig. 3.26: Wing lift and drag relative deviations against AoA (CRP).

Repeating the study with the actuator disk approach leads to the following results, reported in Fig. 3.27 and Fig. 3.28.

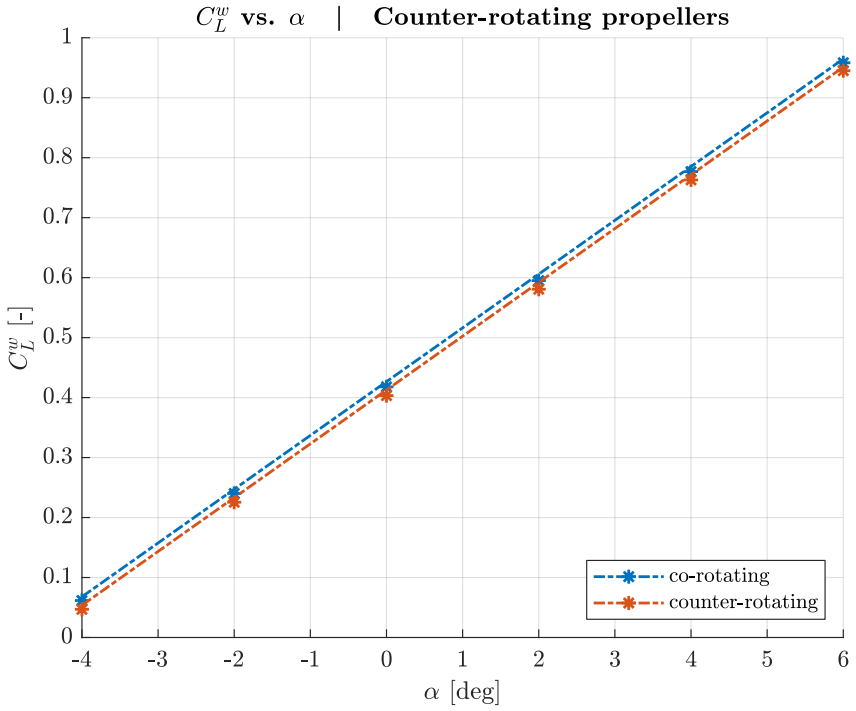

Fig. 3.27: Lift polar of the CRP-AD case wing.

The actuator disk model implemented in VSPAero does not simply compute the variation of the axial velocity induced by the propeller but can predict the entire 3D velocity field behind it. Considering parameters such as the RPM and the direction of the rotation makes it suitable to evaluate the counter-rotating layout.

The two curves in Fig. 3.27 are not coincident, with the one associated with the co-rotating setup slightly above the other one. This method is thus not able to see the advantages of the counter-rotating configuration captured by the purely VLM approach; it instead presents the co-rotating layout as the most beneficial. The lift coefficient reduction associated with the counter-rotating setup is almost uniform throughout the considered angles of attack, the average variation is –0.014. Fig. 3.28 compares the two drag polars. A significant deviation is present, once again almost uniform across the considered AoA range. The drag coefficient of the counter-rotating layout is on average 0.0018 larger than its co-rotating counterpart.

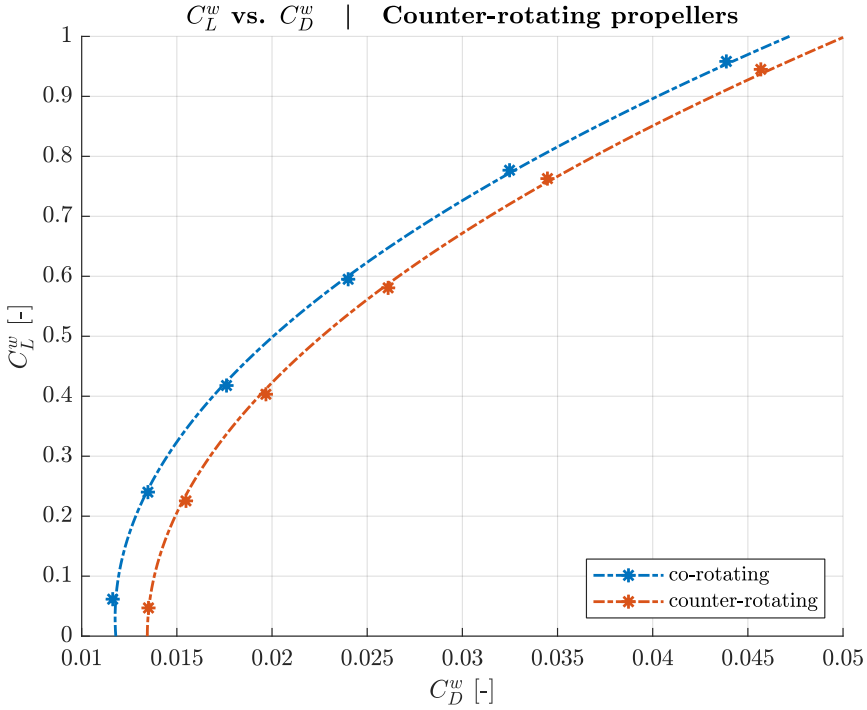

Fig. 3.28: Drag polar of the CRP-AD case wing.

The inability of the actuator disk approach to capture the advantages of the counter-rotating configurations is an additional reason supporting the purely VLM approach as the preferred method for the following part of this work, thus including the development of the meta-model.

Chapter 4

UNIFIER19

This chapter focuses on UNIFIER19, the aircraft selected for the meta-model derivation. Being seized at Politecnico di Milano using TITAN, many data are available, including some OpenVSP models, making it the ideal candidate for this work. The detailed description of the geometry of configuration C7A-HARW follows a brief presentation of the overall project. This chapter also presents an approach that exploits some results of Chapter 3, aiming to reduce the computational costs of the subsequent numerical campaign for the meta-model derivation.

4.1 Aircraft description

As stated on the project website [26], CS-23 Amdt. 5 enabled the development and certification of novel aircraft concepts, including a 19-passenger hybrid-electric commuter. UNIFIER19 is a community-friendly miniliner that goes beyond the mere replacement of existing commuters with a cleaner alternative: it aims at providing an innovative near-zero-emission (NZE) air mobility solution for our communities.

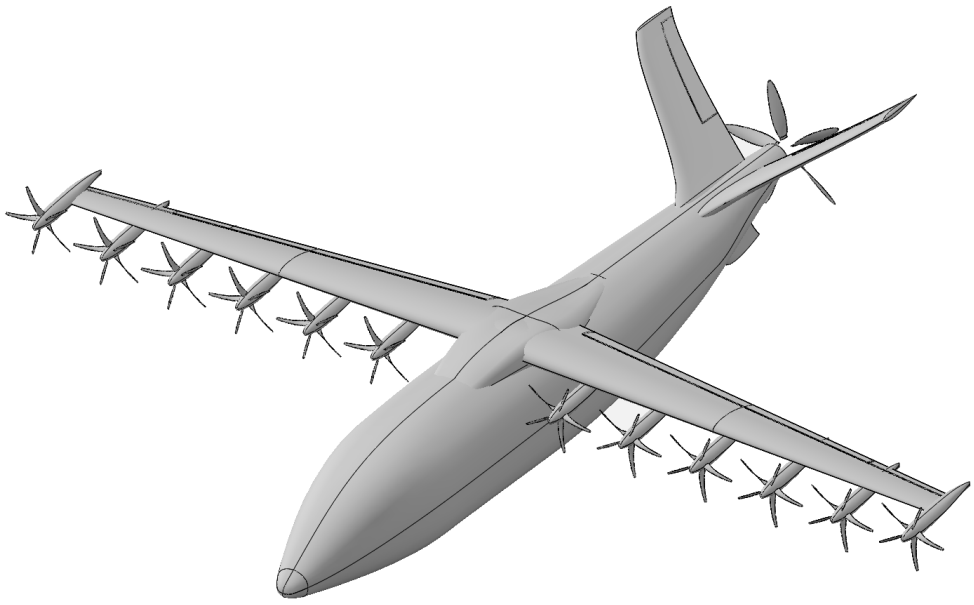

Fig. 4.1: OpenVSP model of the configuration C7A-HARW [27].

Pipistrel Vertical Solution [27], partner and project coordinator of UNIFIER19, provided all the geometric models shown in this chapter already implemented in OpenVSP.

Fig. 4.1 illustrates a partially modified version of the configuration C7A presented in [28] and selected as the more promising design among the several configurations initially considered. HARW stands for High Aspect Ratio Wing; the most significant change with respect to the original C7A is the optimized wing, with the aspect ratio raised from 9 to 14.

Compared to the relatively simple layout of the MPC, the wing of UNIFIER19 is more complex and realistic; despite being still straight, it features a pronounced taper, slightly negative dihedral and twist, and a thickness ratio variable spanwise. All the geometric details are in Tab. 4.1.

b	20.11 m
$\bar{c}$	1.54 m
S	28.90 m^2
AR	14
Λ	0°
λ	0.37
Γ	−2°
α_t	−3°
i_w	3°
Airfoil	LS(1)-0413 MOD
$(t/c)_r$	0.195
$(t/c)_t$	0.129

Tab. 4.1: Wing geometry of configuration C7A-HARW.

Tab. 4.2 reports the main geometric parameters of the 5-bladed DEP propellers. The odd number of blades is beneficial for lowering noise originating from propeller wake-wing interaction [28].

d	1.60 m
r_h	0.163 m
$\beta_{3/4}$	31.5°
ϵ	−5°

Tab. 4.2: DEP propeller geometry of configuration C7A-HARW.

The changes to the geometry of the Sinnige's propellers, namely the increase of the hub radius and the reduction of the blade pitch described in Section 2.2.3, were necessary to match the numerical results with the experimental data. The large propeller considered from now on, however, does not suffer either of the problems related to the small ones used by Sinnige, like the locally inefficient

airfoils at the root or the significant viscous effects at low Reynolds numbers. Moreover, no experimental data are available for this case. Such variations, therefore, are not applied to the propellers of UNIFIER19.

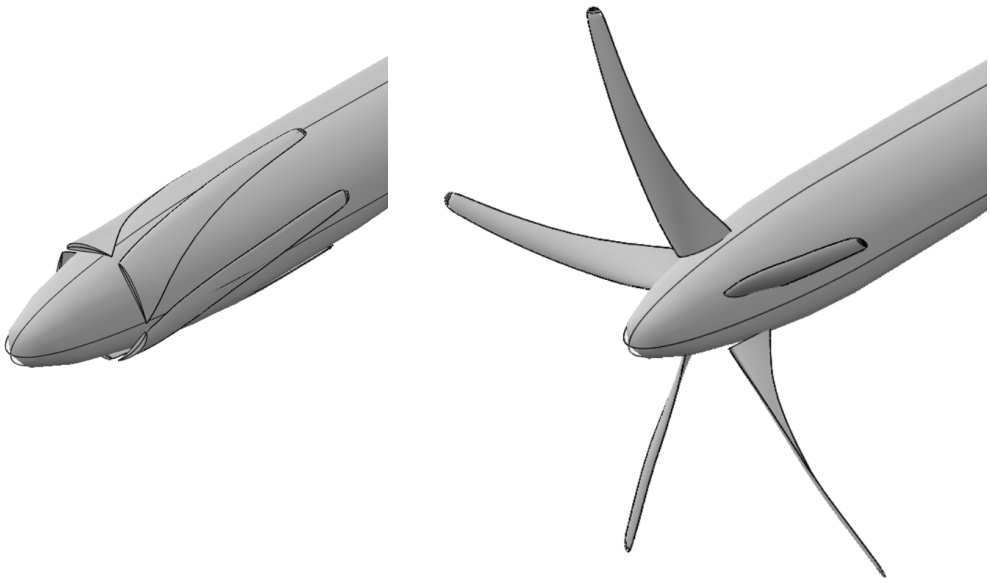

(a) folded blades (b) unfolded blades

Fig. 4.2: Detail of the DEP propellers featuring foldable blades used in the numerical simulations.

Since the DEP system is off during cruise, blades can fold over the nacelle reducing the drag when the HLPs are not operating. Fig. 4.2 highlights the DEP propellers geometry in the folded and unfolded configuration.

The DEP system of configuration C7A-HARW consists of 12 identical propellers, evenly distributed spanwise and installed on the wing leading edge. The separation between propellers is set to zero to maximize the blown surface while avoiding overlap. Tab. 4.3 reports the position of all the six couples of propellers, including the WTPs.

ID	X	$\lvert Y \rvert$	Z
1	−6.56 m	2.05 m	−1.63 m
2	−6.62 m	3.65 m	−1.61 m
3	−6.67 m	5.25 m	−1.58 m
4	−6.73 m	6.85 m	−1.55 m
5	−6.78 m	8.45 m	−1.52 m
6	−6.82 m	10.05 m	−1.64 m

Tab. 4.3: Position of DEP propeller couples.

4.2 Computational cost reduction

The cost of running an extensive numerical campaign in the preliminary design phase may be detrimental, especially when the computational resources are somewhat limited.

The presence of several propellers, typical of a DEP layout, significantly increases the duration of the simulations relying on the purely VLM approach. In Section 3.1.2, the regularity of both lift and drag increments with the number of propellers suggests that a limited set of simulations, carried out running only a few propellers, can provide meaningful information about the entirely blown setup. This section aims to present the approach required to deal with relatively complex geometry, such as the one of UNIFIER19.

4.2.1 Reduced approach concept

The untwisted rectangular wing considered for the MPC study, extensively described in Section 3.1.1, is a highly ideal setup seldom used by real aircraft, intentionally chosen for its simplicity. In that case, excluding the WTPs, all the propeller contributions to the lift and drag increments were almost identical, no matter their spanwise position. This behavior was somehow predictable since all the parameters describing the setup geometry remain constant spanwise, and thus the propellers were blowing identical sections of the wing. In principle, two simulations are sufficient to determine the total DEP system lift and drag increments at a specific flight condition: the contributions of the WTPs require a separate simulation, while those of all the inboard propellers are obtainable from the one of a generic mid-wing propeller. An additional simulation, mounting at least two couples of propellers, allows also extrapolating the unblown wing coefficients, as shown in Section 3.1.3.

Such a simplified approach is not suitable for more complex geometries, like the one featured by UNIFIER19, where the spanwise variable geometry reflects in a spanwise variable lift and drag distributions, even when considering high AR and staying away from the wingtips.

	Root	**Tip**
c	2.100 m	0.777 m
α_g	3°	0°
t/c	0.195	0.129

Tab. 4.4: C7A-HARW main geometric parameters at wing root and tip.

Tab. 4.4 shows the values at the wing tip and root of the geometric parameters varying linearly along the span. To a first approximation, it is possible to assume that even the lift and drag increments are linear with the spanwise position of the propeller, as well as the local lift and drag of the considered unblown section.

Fig. 4.3 shows the lift coefficient of the fixed group, i.e., of the entire geometry except for the propellers, as a function of the spanwise position of the propeller. The considered setup is the one of UNIFIER19 configuration C7A-HARW, but with only one couple of propellers installed; the selected angle of attack is 4°. The figure proves the hypothesis formulated above: the

contribution of the inboard propeller couples is almost linear with their spanwise position. The effects of the WTPs, on the other hand, are significantly lower, as already noted in the MPC study.

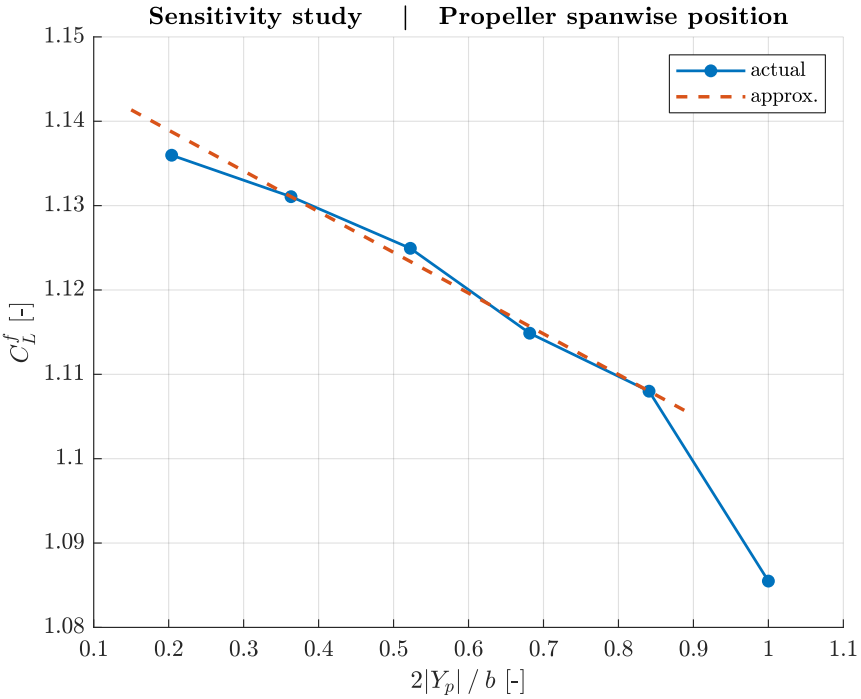

Fig. 4.3: Lift coefficient sensitivity to propeller spanwise position for UNIFIER19 configuration C7A-HARW.

Thanks to the linearity, it should be possible to extrapolate the unblown wing polar and derive a model for the lift and drag increments produced by the inboard propellers using only three simulations for each flight condition. Note that the MPC, where the increments were constant with the spanwise position, only required two simulations. A fourth simulation will finally estimate the contributions of the WTPs.

Removing the unblown wing coefficients, computed separately, from the blown simulations results may be sufficient to obtain the increments induced by the propellers. However, to exclude possible sources of discrepancies, like those that led to opting for the unblown polars extrapolation in the MPC, the lift and drag increments computation relies entirely on the blown layout numerical results. The third simulation, including both the inboard propellers used in the first two simulations, is thus required. Moreover, the extrapolation of the unblown polar will help to assess the accuracy of the reduced approach.

Defining the total lift coefficient as the sum of the unblown wing contribution and the DEP-related increments, it is then possible to write down the following system of linear equations:

$$\begin{cases} C_{L_u}^f + \Delta C_{L_2}^f = C_{L_2}^f & (4.1) \\ C_{L_u}^f + \Delta C_{L_5}^f = C_{L_5}^f & (4.2) \\ C_{L_u}^f + \Delta C_{L_2}^f + \Delta C_{L_5}^f = C_{L_{2\&5}}^f & (4.3) \end{cases}$$

The example above uses the second and the fifth propeller couple, where the first is the closest to the symmetry plane and the sixth is the one at the

wingtip. Excluding the WTPs, any other pair of propellers is adequate for the purpose. Concerning the superposition of the effects of the two couples of propellers in Eq. (4.3), the preliminary studies presented in Chapter 3, which did not highlight any significant interaction between the propeller slipstreams, justify this choice.

Rewriting the system above in the typical matrix form

$$\mathbf{Ax} = \mathbf{b} \tag{4.4}$$

leads to

$$\begin{bmatrix} 1 & 1 & 0 \\ 1 & 0 & 1 \\ 1 & 1 & 1 \end{bmatrix} \begin{bmatrix} C_{L_u}^f \\ \Delta C_{L_2}^f \\ \Delta C_{L_5}^f \end{bmatrix} = \begin{bmatrix} C_{L_2}^f \\ C_{L_5}^f \\ C_{L_{2\&5}}^f \end{bmatrix} \tag{4.5}$$

Finally, inverting the matrix as follows, it is possible to obtain the unblown wing lift coefficient and the lift coefficient increments related to the two considered propellers, from which extracting the linear trend for the other inboard ones.

$$\mathbf{x} = \mathbf{A^{-1}b} \tag{4.6}$$

The procedure applied to compute the drag increments, not reported here for brevity, is analogous to the one used for lift.

In order to compute the contributions of the WTPs, it is sufficient to subtract from the results of their dedicated simulations the $C_{L_u}^f$ just obtained from Eq. (4.6). Although been considered due to the possible further computational cost reduction, the extrapolation of the WTP increments from the inboard propellers model is not feasible. The 1.4% increment, computed at the considered AoA, is in line with the 2.8% predicted by the model, taking into account the reduced blown surface, which is actually half of the one blown by an inboard propeller. Unluckily, the same does not apply to drag in general or lift at other angles of attack, such as those used to create the polars in Section 4.2.2, where the WTPs contributions are always lower than expected, as observed in Chapter 3 concerning the MPC. In that case, however, due to the small propellers and their highly ineffective blowing, the WTPs contributions were even almost negligible. In the end, there is no way to avoid dedicated simulations of the WTPs.

4.2.2 Results and evaluation

The present section shows some results of the reduced approach proposed to lower the computational cost of the numerical campaign by at least 50÷60%. Applying the procedure described in Section 4.2.1 on four different sets of simulations, spanning a range of four angles of attack, allows generating the polars evaluated in the following.

The term *reduced*, in this section, refers to all the results of the previously described reduced approach; the curves in the plots referred to just as *blown* or *unblown* are those obtained from simulations of the actual unblown or completely blown layout.

The considered setup is still the same presented in Section 4.1, exhibiting no flap deflection. The airspeed and the propeller RPM values are those of [28]

concerning the original configuration C7A. Tab. 4.5 shows in detail all the conditions for the test.

V	39.4 m/s
N	1500
J	0.985
ρ	1.225
Re	3.99e+06
M	0.114
δ_f	0°

Tab. 4.5: Test conditions.

Fig. 4.4 shows the lift coefficient against AoA curves of UNIFIER19 configuration C7A-HARW. The solid lines, the blue one and the red one, are obtained applying the reduced approach. The *unblown (reduced)* lift coefficient comes from Eq. (4.6); the *blown (reduced)* one, instead, is the sum between the *unblown (reduced)* one and the increments either computed directly or extrapolated from the linear trend. The yellow and the purple dashed lines represent the references for this analysis: the former results from a steady VLM simulation of the aircraft without any propeller; the latter, on the other hand, comes from the simulation of the actual geometry of configuration C7A-HARW, with all the 12 propellers running. Finally, the green dashed line comes from a simulation based on the AD approach rather than on the purely VLM approach.

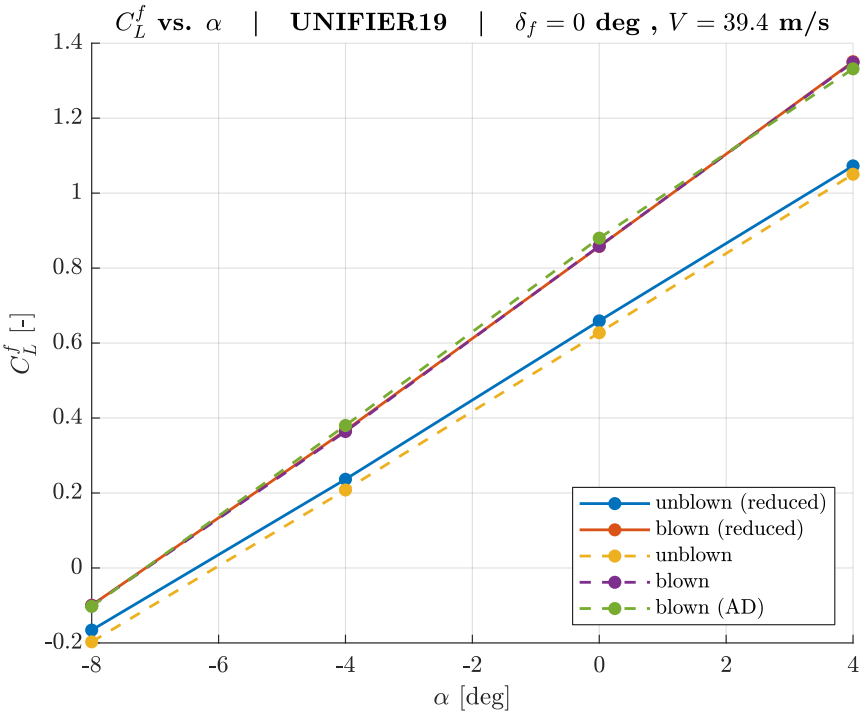

Fig. 4.4: Lift polar of UNIFIER19 configuration C7A-HARW.

The comparison of the three blown curves shows a very close match, especially between the reduced one and that associated with the actual completely blown geometry. The matching between the unblown curves is satisfactory too. Despite not being the main target of the reduced approach, the estimation of the unblown polar allows assessing the method capability to capture the overall physics of the blowing. The reduced method marginally overpredicts the unblown setup lift, and thus it slightly underestimates the lift coefficient increments produced by the DEP system. Since a relatively conservative estimate is appreciable in the early design stages, no correction is necessary. Finally, at least for what concerns lift, the slightly increased accuracy of the purely VLM approach with respect to the AD approach does not seem worth its additional complexity and computational costs.

Fig. 4.5 illustrates the drag polars of UNIFIER19 configuration C7A-HARW. Modeling the entire aircraft geometry, rather than just the wing as in the previous studies, leads to the relatively large drag coefficient observed in these plots, even at low C_L^f. The reduced approach curves are still very close to their reference counterparts. The discrepancy between the blown and unblown polars of approximately 0.01 and almost constant with C_L^f, is compatible with the increased parasite drag of the 12 additional nacelles, which VSPAero estimates in 0.00928. Unlike for lift, in this case, the higher accuracy of the purely VLM approach repays well the increased computational costs associated with it; moreover, the AD approach, already discarded in the validation phase, appears highly conservative.

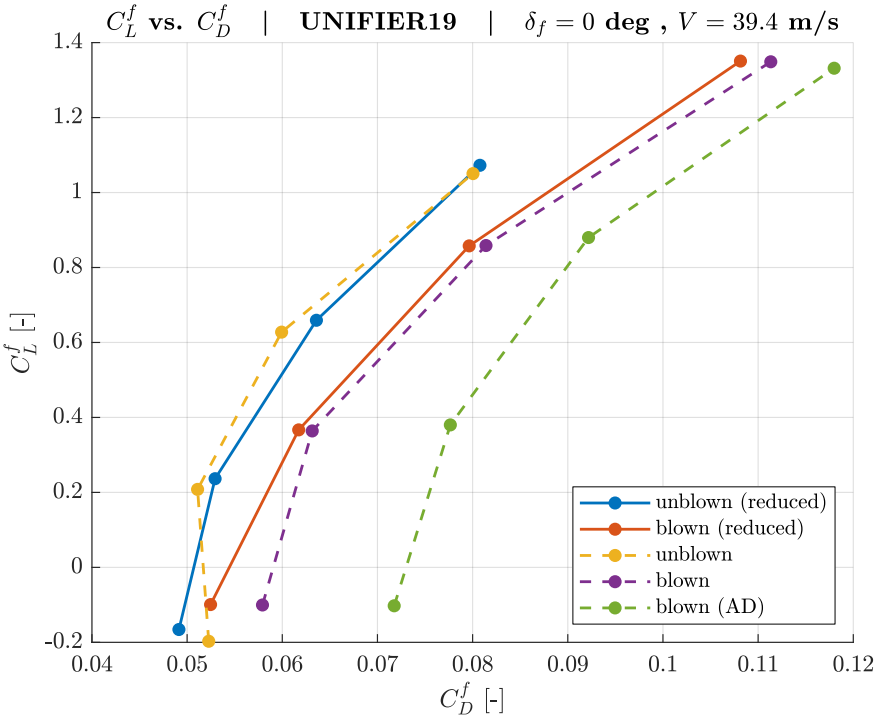

Fig. 4.5: Drag polar of UNIFIER19 configuration C7A-HARW.

A possible drawback of the reduced approach is its tendency to underestimate the drag increments. Although a highly conservative method may easily lead to suboptimal solutions, excessively optimistic estimates are

not desirable in the early design phases. In order to circumvent the issue, it is possible to introduce a penalty that raises drag towards higher values.

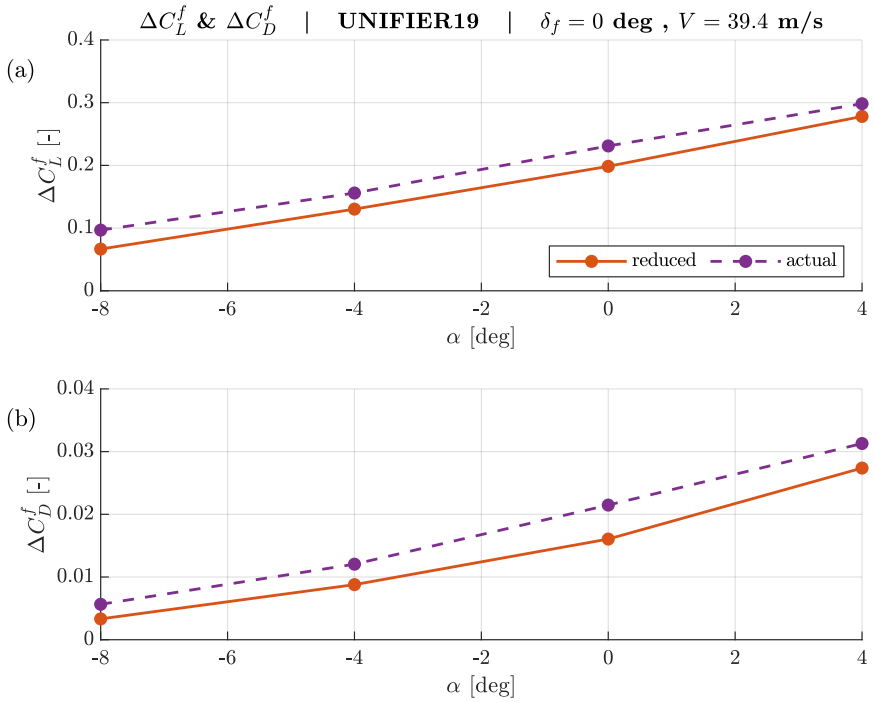

Fig. 4.6: Comparison between reduced and actual lift and drag increments of UNIFIER19 configuration C7A-HARW.

Fig. 4.6 shows the lift and drag increments induced by the DEP system, computed with the reduced approach and the simulations of the actual unblown and completely blown layouts. The discrepancies are almost constant with the AoA. The drag increment estimate, shown in Fig. 4.6b, can be made conservative by introducing a penalty of at least +0.0037. Concerning lift, on the other hand, the reduced approach results shown in Fig. 4.6a can be made less conservative with a ΔC_L^f increment of up to 0.0272.

Chapter 5

Development of the DEP Meta-Model

The present chapter represents the core of this thesis. It describes the process that ultimately led to the implementation in TITAN of a meta-model for the aero-propulsive interaction of a DEP system, starting from the construction of the data set, carried out through a dedicated numerical campaign.

This work aims to provide a viable method to integrate the overall DEP aero-propulsive modeling in a preliminary design tool. Depending on the complexity and generality that the meta-model desires to achieve, however, the required data points may be more or less numerous, severely impacting the computational costs. A modular approach represents thus a requirement to address possible time constraints, both in the development phase and in future operative scenarios. Independent methods using independent data sets enable both the incremental development of the code, eventually assigning the actual implementation to future works, and the creation of a sizing procedure with adaptive accuracy, depending on the extent of the available data set.

5.1 Construction of the data set

The data set represents the heart of the proposed meta-model, storing all the data collected during the numerical campaign. TITAN interrogates this database during the iterations of the sizing loop, obtaining the required results without the need to run multiple VLM simulations in real-time.

5.1.1 Dimensional analysis

Identifying the dependencies between the considered variables is the first step in the development of a meta-model. The expression of a generic aero-propulsive force acting on a blown wing is the following:

$$F = F(\rho, a, \mu, V, \alpha, S, \epsilon, d, N) \tag{5.1}$$

where the force F is assumed to depend on the air density ρ, the speed of sound a, the air viscosity μ, the airspeed V, the angle of attack α, the wing surface S, the propeller tilt angle with respect to the wing reference chord ϵ, the propeller diameter d, and the propeller RPM N.

According to the Buckingham π theorem, it is possible to rewrite the relation between n dimensional quantities involving k physical dimensions as the

relationship between m dimensionless groups, where $m = n - k$. Concerning Eq. (5.1), which involves eight dimensional quantities and three physical dimensions (mass, length, and time), it should be possible to identify five dimensionless groups, also called π-groups, to rewrite the problem in a different form.

The first π-group is the well-known force coefficient, conventionally used to express forces in a dimensionless form:

$$\pi_1 = \frac{F}{\rho V^2 S} = \frac{C_F}{2} \tag{5.2}$$

The second and the third π-group are still two well-known quantities, i.e., the Mach number and the Reynolds number:

$$\pi_2 = \frac{V}{a} = \mathrm{M} \tag{5.3}$$

$$\pi_3 = \frac{\rho V \sqrt{S}}{\mu} \sim \mathrm{Re} \tag{5.4}$$

Since TITAN operates at a constant aspect ratio, i.e., the one specified in the input files, the reference length $\sqrt{S}$ is proportional to the wing MAC; thus, the proposed π_3 is proportional to the conventionally defined Reynolds number computed using the chord.

The fourth dimensionless group is the ratio between the propeller diameter and the square root of the wing surface:

$$\pi_4 = \frac{d}{\sqrt{S}} = r_p \tag{5.5}$$

They respectively represent the reference lengths of the propeller and the wing, conventionally used in the definitions of their corresponding force coefficients, such as C_T or C_L.

The last π-group is a rearranged advance ratio:

$$\pi_5 = \frac{V}{N\sqrt{S}} = J r_p \tag{5.6}$$

Its definition, resulting from the Buckingham π theorem, contains $\sqrt{S}$ as reference length and is equivalent to the product between J and the previously defined dimensionless group r_p. The traditional advance ratio is thus a legitimate option to replace π_5.

Finally, the dimensionless form of Eq. (5.1) is the following:

$$C_F = C_F(\mathrm{M}, \mathrm{Re}, r_p, J, \alpha, \epsilon) \tag{5.7}$$

where the force coefficient C_F is a function of the Mach number M, the Reynolds number Re, the geometrical parameter r_p, the advance ratio J, and the two already dimensionless quantities α and ϵ.

Reducing the number of parameters is beneficial, especially in view of an extensive experimental or numerical campaign, since it will significantly reduce the number of test points. In the considered case, for example, the construction of a multi-dimensional map of the force coefficient, selecting three values for each parameter, requires 27 times fewer simulations than a map of the dimensional force.

5.1.2 Design of the numerical campaign

The analysis discussed in Section 5.1.1 pointed out seven dimensionless parameters to rewrite the generic aero-propulsive force expression of Eq. (5.1), which initially involves ten quantities.

To further reduce the design space, it is possible to fix the value of some of those new parameters, like the Mach number, the Reynolds number, and the geometrical parameter r_p. Considering that High Lift Propellers operate in a relatively narrow range of conditions, Mach and Reynolds are set to those of a typical low speed and low altitude scenario, with an airspeed of 40 m/s, at the mean sea level in standard ISA atmosphere. Regarding the geometrical parameter r_p, its value does not change throughout the design loop since the Hyperion input file fixes both the number of HLPs and the wing aspect ratio; said so, there is no point in including multiple r_p values in the numerical campaign. Tab. 5.1 reports then the selected values for those three parameters.

M	0.114
Re	3.99e+6
r_p	0.2976

Tab. 5.1: Parameters that remain fixed throughout the numerical campaign.

Concerning the remaining four quantities: the force coefficient C_F is the dependent variable of Eq. (5.7), and determining its value is the objective of the numerical campaign; the other three parameters (α, ϵ, and J) are thus the independent variables, and changing their values allows to generate the multi-dimensional map ultimately integrated into TITAN.

Case ID	ϵ	J
MM.tm12.J08	−12°	0.8
MM.tm12.J12	−12°	1.2
MM.tm12.J16	−12°	1.6
MM.tm6.J08	−6°	0.8
MM.tm6.J12	−6°	1.2
MM.tm6.J16	−6°	1.6
MM.t0.J08	0°	0.8
MM.t0.J12	0°	1.2
MM.t0.J16	0°	1.6

Tab. 5.2: List of numerical campaign cases.

Tab. 5.2 illustrates the cases considered for the present numerical campaign, with the tilt angle varying between –12° and 0°, and the advance ratio spanning from 0.8 to 1.6. The nine scenarios are all the possible combinations of ϵ and J obtainable by selecting three values for each parameter; both reference [28] and UNIFIER19 OpenVSP model provided meaningful information to assume two

plausible ranges. Finally, to properly construct the lift and drag polars, the AoA needs to be changed. Each of the nine cases reported in Tab. 5.2 thus contains six data points corresponding to six equally spaced angles of attack, ranging from –4° and +16°.

The reduced approach, extensively described in Section 4.2.1, is applied to lower the computational costs of the campaign. Four highly efficient simulations, mounting only a limited number of propellers, replace each of the otherwise more time-consuming simulations featuring all 12 propellers. Fig. 5.1 illustrates the four setups involved in this numerical campaign: the first three layouts are those used to compute the lift and drag increments for the inboard propellers and extrapolate the unblown wing curves; the last one, on the other hand, provides the increment associated with the WTPs.

(a) layout prop2

(b) layout prop5

(c) layout prop2&5

(d) layout prop6

Fig. 5.1: Geometrical setups used in the numerical campaign.

Each of the cases in Tab. 5.2 thus includes four different sets of polars, one for each of the layouts used in the reduced approach, bringing the total to 36 subcases; Tab. 5.3 reports the corresponding identifiers used to discriminate between the simulations of the same case.

Polar ID	Operating propellers
prop2	2
prop5	5
prop2&5	2 and 5
prop6	6 (WTP)

Tab. 5.3: List of polars sets computed for each case.

The availability of lift and drag increments produced by individual propellers, instead of the overall variation produced by the complete blowing, represents an additional advantage of the reduced approach. Dealing with twisted wings, for example, does not require running several simulations with different values of twist. Given the system geometry, it is possible to determine the local tilt and AoA behind each propeller, individually compute their contributions starting from data collected using untwisted wing simulations matching the local parameters, and finally obtain the overall increments.

Ultimately, to further reduce the computational costs, the geometry considered for the simulations includes just the wings and the DEP system. Fig. 5.2 illustrates layout prop2&5 of one of the cases featuring zero propeller tilt. Tab. 5.4 provides all the geometrical details of the wing, which is basically an untwisted version of UNIFIER19 configuration C7A-HARW wing.

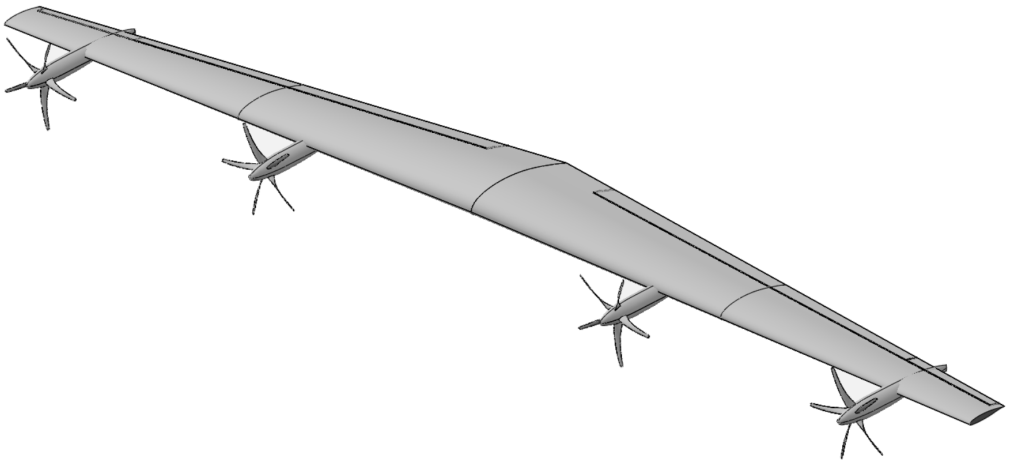

Fig. 5.2: OpenVSP model of layout prop2&5.

b	20.11 m
$\bar{c}$	1.54 m
S	28.90 m²
AR	14
Λ	0°
λ	0.37
Γ	−2°
α_t	0°
i_w	0°
Airfoil	LS(1)-0413 MOD
$(t/c)_r$	0.195
$(t/c)_t$	0.129

Tab. 5.4: Wing geometry for meta-model derivation.

5.1.3 Results of the numerical campaign

To take a look at all the raw data collected during the numerical campaign described in Section 5.1.2. the reader may refer to Appendix C.1. Fig. 5.3 shows an example of these raw polars, namely those of case MM.t0.J08. Lift and drag coefficients are again those acting on the fixed group, i.e., on the considered geometry without the propellers.

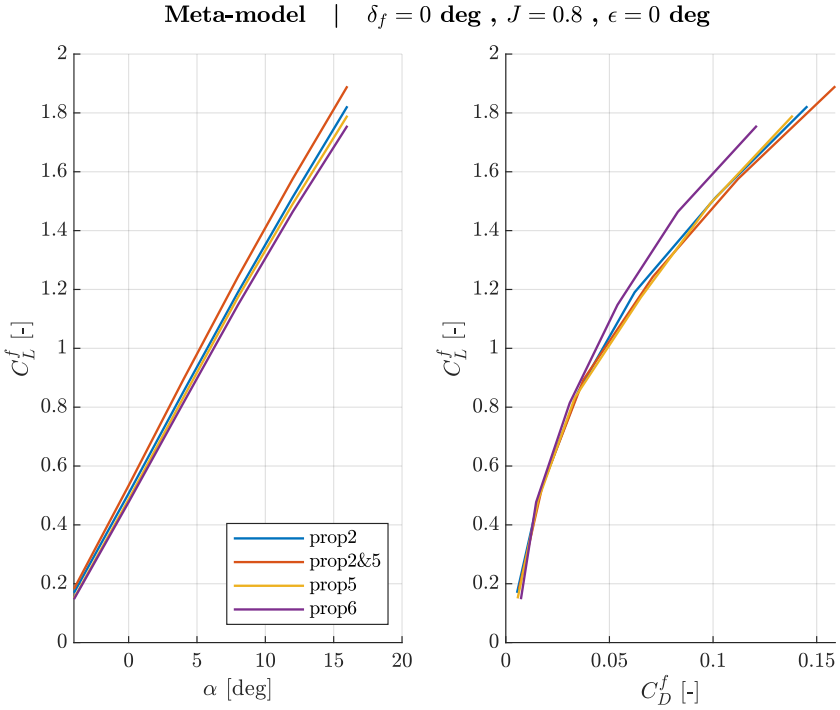

Fig. 5.3: Example of numerical campaign raw data (case MM.t0.J08).

Fig. 5.3 highlights some of the aspects already noted so far: for example, the WTPs (prop6 in the figure) exhibit a slightly lower C_L compared to other propellers due to the smaller blown surface; the induced drag, on the other hand, is significantly lower due to the WTP beneficial effect on the wingtip vortices.

Considering the relatively large size of the numerical campaign, which consists of 216 data points in total, it is legitimate to expect a certain number of corrupted results. These issues are easily spottable, inspecting the raw data plots; and rapidly solvable, replacing the faulty values with those coming from the interpolation of the good ones. The correction task is left entirely manual since it is a process that requires critical thinking and human judgment.

Going back to the considered numerical campaign, only 3 of the 36 generated sets of polars present some issues. Fig. 5.4 shows an example of a poorly converged polar, i.e., prop6 of case MM.t0.J16. At the highest considered advance ratio, blowing effects are negligible; all the polars in Fig. 5.4, as in all the other J16 cases shown in Appendix C, thus tend to coincide, no matter which propellers are operating. Spotting the inconsistencies in the polar associated with WTPs in Fig. 5.4, like in the other two affected polars not shown here for conciseness, is thus an easy task.

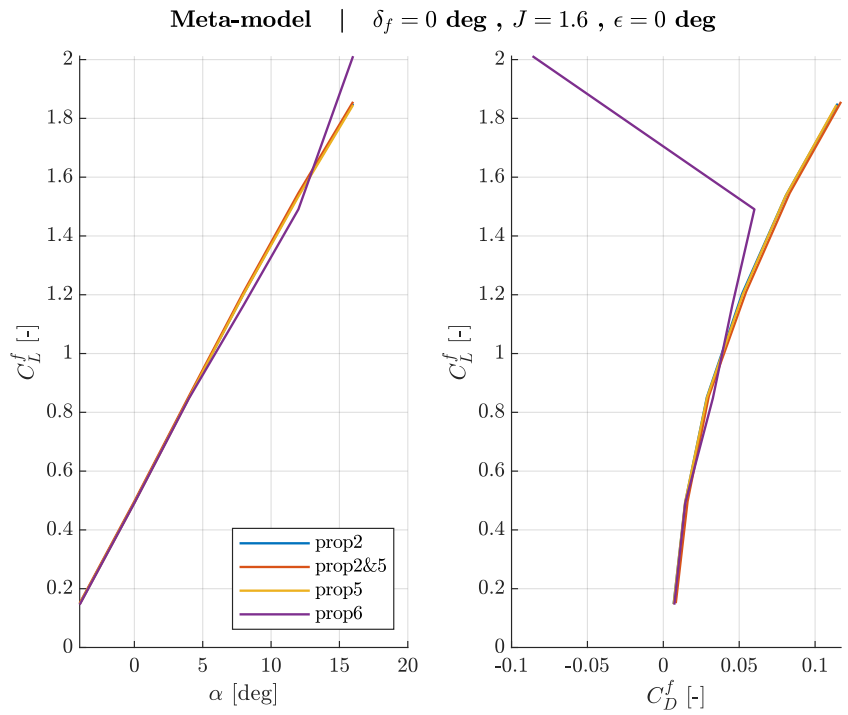

Fig. 5.4: Example of a poorly converged polar (case MM.t0.J16).

Following the correction of the corrupted data and the application of the reduced approach, it is possible to compute the lift and drag increments generated by each propeller for all the 54 test conditions, i.e., for all the possible combinations of advance ratio, propeller tilt, and angle of attack.

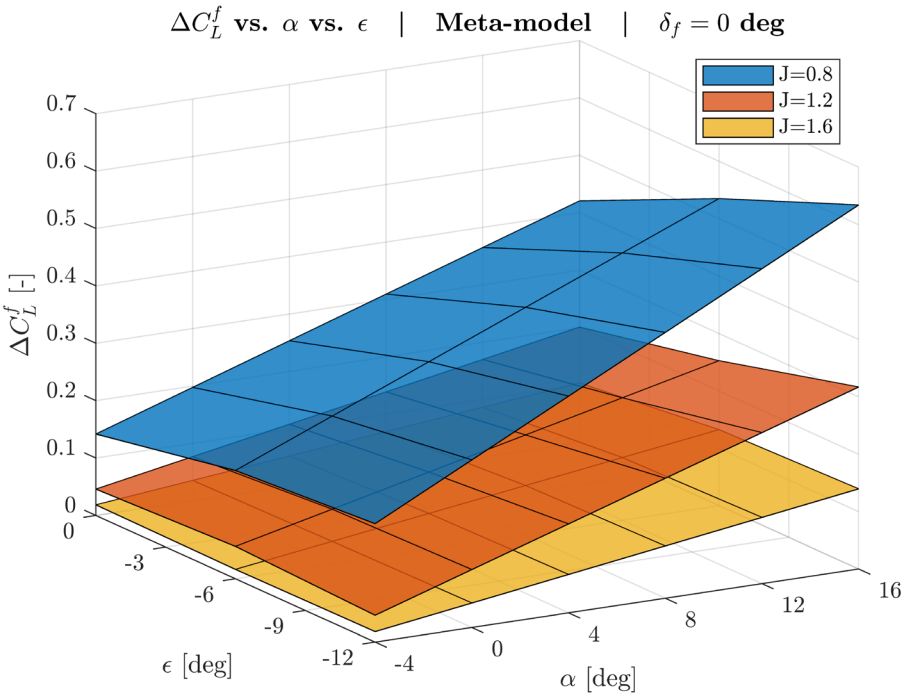

Fig. 5.5: Lift coefficient increment multi-dimensional map.

The so-formed dataset then represents a multi-dimensional map of the lift and drag increments, i.e., an object that, given its parameters, provides the value of these increments. Fig. 5.5 shows the blown wing lift coefficient increment in all 54 test conditions. The lift increments in a specific combination of ϵ, α, and J can then be computed through linear interpolation.

The code implemented in TITAN will eventually benefit from individual propeller contributions, composing the overall lift and drag increments given the system geometry. For the analysis presented in this chapter, however, the wing geometry is the one of Tab. 5.4; the overall increments at a specific test condition are thus simply the sum of all the propeller contributions at the same test condition.

The coefficients present in the dataset do not exhibit any specific irregularity, showing a relatively smooth transition when parameters change. Their increments, however, being only a fraction of the coefficients, may amplify even little variations; applying the usual approximations of 2D curves, i.e., C_L linear with α and C_D quadratic with C_L, significantly mitigates this feature, as clearly visible in all the figures shown here.

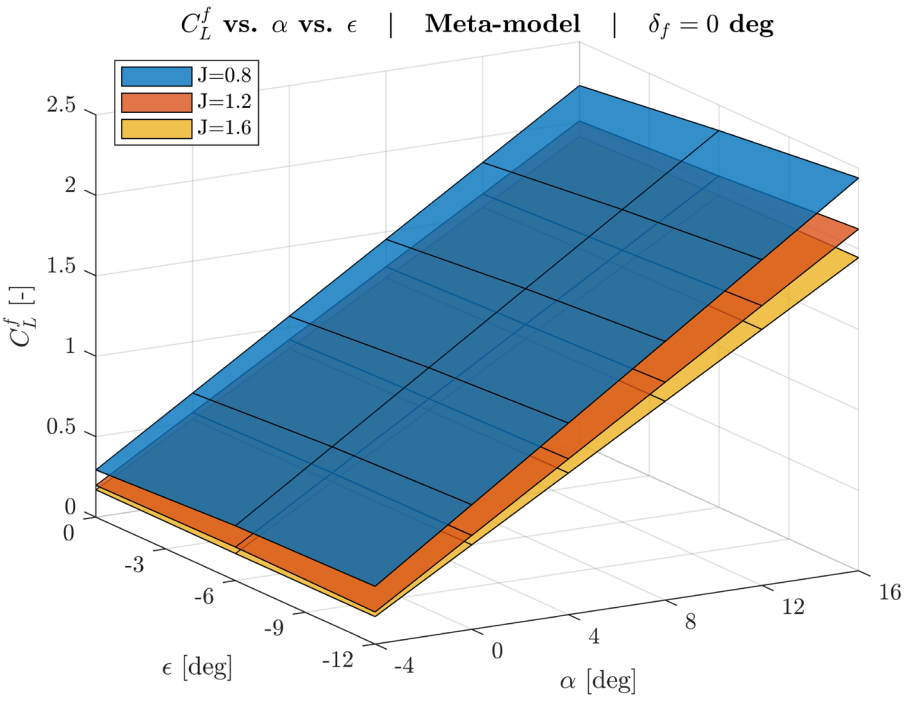

Fig. 5.6: Lift coefficient multi-dimensional map (same J on same layer).

Fig. 5.6 shows the blown wing lift coefficient in all 54 test conditions. Each layer corresponds to a different advance ratio and represents a sort of 3D version of the typical C_L vs. α curve. In this case the lift coefficient is plotted against both the AoA and the propeller tilt. Fig. 5.7 illustrates the same 54 lift coefficients, replacing the advance ratio with the propeller tilt and vice versa. The reduced separation between the three layers in Fig. 5.7, compared to that in Fig. 5.6, indicates a lower sensitivity to propeller tilt than to advance ratio, which becomes even negligible for $J = 1.6$. Although a fair comparison between the sensitivities may be impossible since advance ratio and propeller tilt are two totally different parameters, considering that the two selected

ranges try to cover as much as possible their plausible values, it is clear that changing the propeller RPM is more beneficial than changing their tilt angle. Moreover, since propeller RPM is an operative parameter, rather than a geometrical one like propeller tilt, it may provide additional design authority in the following design phases.

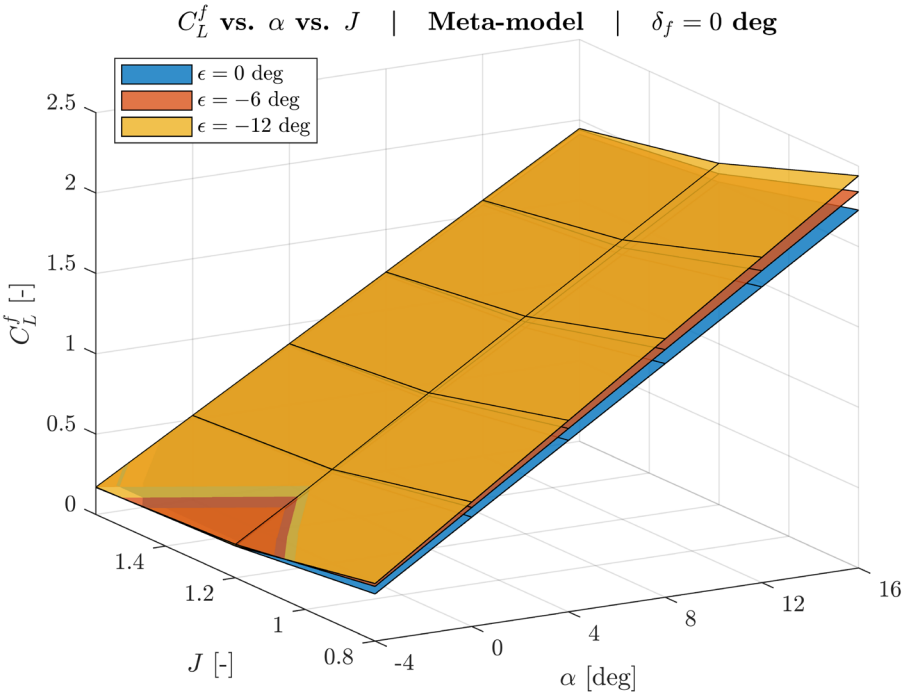

Fig. 5.7: Lift coefficient multi-dimensional map (same ϵ on same layer).

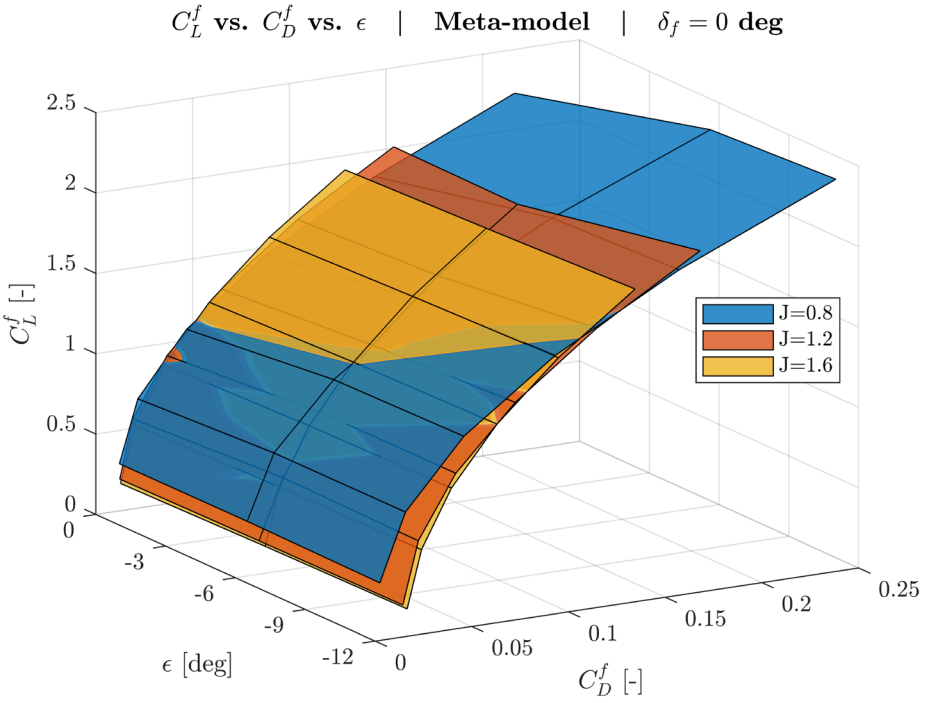

Fig. 5.8: Drag coefficients multi-dimensional map.

Fig. 5.8 illustrates a 3D version of the blown wing drag polar. The three layers, associated with the three different advance ratios, mutually intersect. A lower advance ratio, i.e., a more effective wing blowing, appears beneficial at low C_L, probably due to the advantages of the counter-rotating propellers layout, which is effective in reducing the minimum drag coefficient and increasing its corresponding C_L (see Section 3.3.2). On the other hand, a higher advance ratio appears advantageous at high C_L since the lower blowing effectiveness reduces the increase of drag. However, since lift augmentation is the primary goal of HLPs, the selection of a high J to contain drag is subordinate to the choice of a sufficiently low one to ensure the satisfaction of the C_L target.

Before giving more details about the lift and drag increments, it is worth recalling that the reduced approach provides both these increments and the unblown wing coefficients. Given the nature of this procedure, some variability in the unblown wing coefficients is forecastable since estimates come from independent simulations. Averaging all the unblown wing polars allows to consistently define the increments throughout the entire numerical campaign. In the end, however, the variability is much less than expected, especially across different tilt angles due to the reduced sensitivity. In Fig. 5.9, the dashed lines, which represent the unblown wing C_L vs. α curves, are almost coincident; this may suggest avoiding running simulations prop2&5 for all the tilt angles and computing the increments directly by subtracting the unblown wing coefficients, further reducing computational costs.

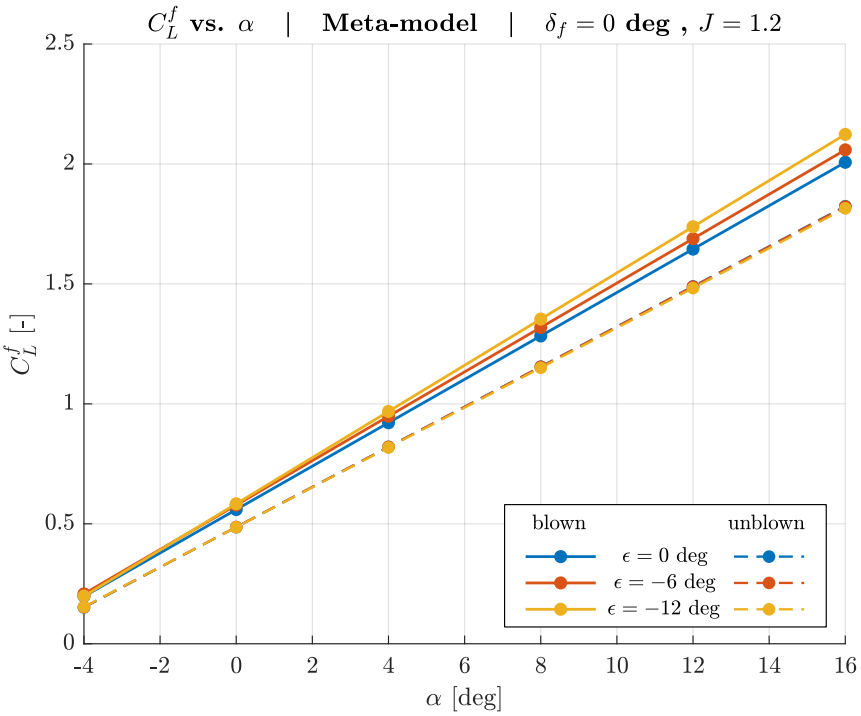

Fig. 5.9: Example of meta-model lift polars ($\delta_f = 0°$, $J = 1.2$).

The following figures provide more examples of lift and drag coefficient increments in various conditions. Fig. 5.10 and Fig. 5.12 show respectively the increments of the lift and the drag coefficients at different angles of attack, at a constant advance ratio equal to 0.8, for all the three considered values of propeller tilt. Fig. 5.11 and Fig. 5.13, instead, show again the previously

mentioned quantities but at a constant propeller tilt, equal to 0°, for all the three considered values of the advance ratio.

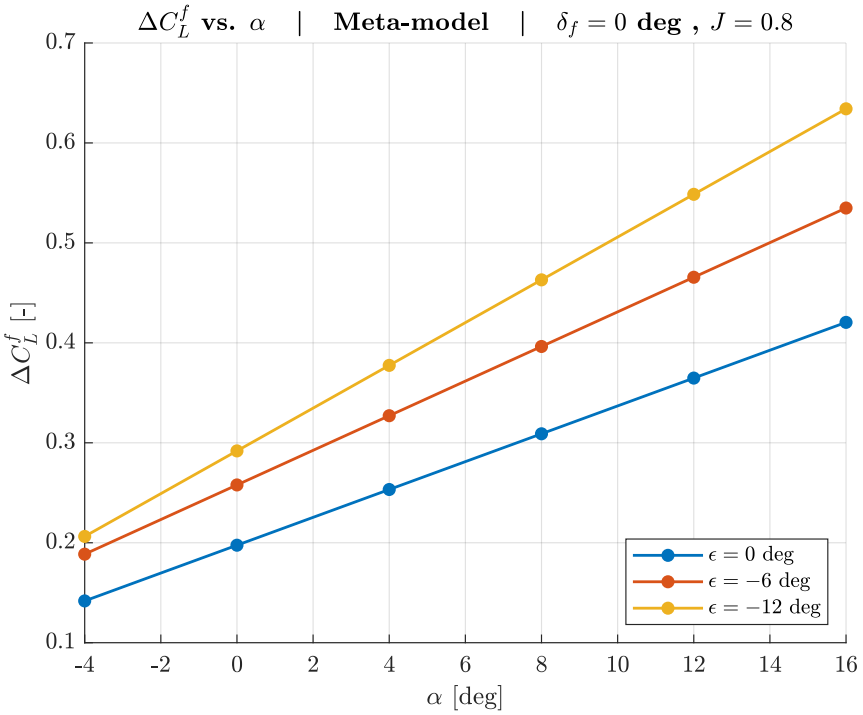

Fig. 5.10: Lift coefficient increment at a fixed advance ratio ($\delta_f = 0°$, $J = 0.8$).

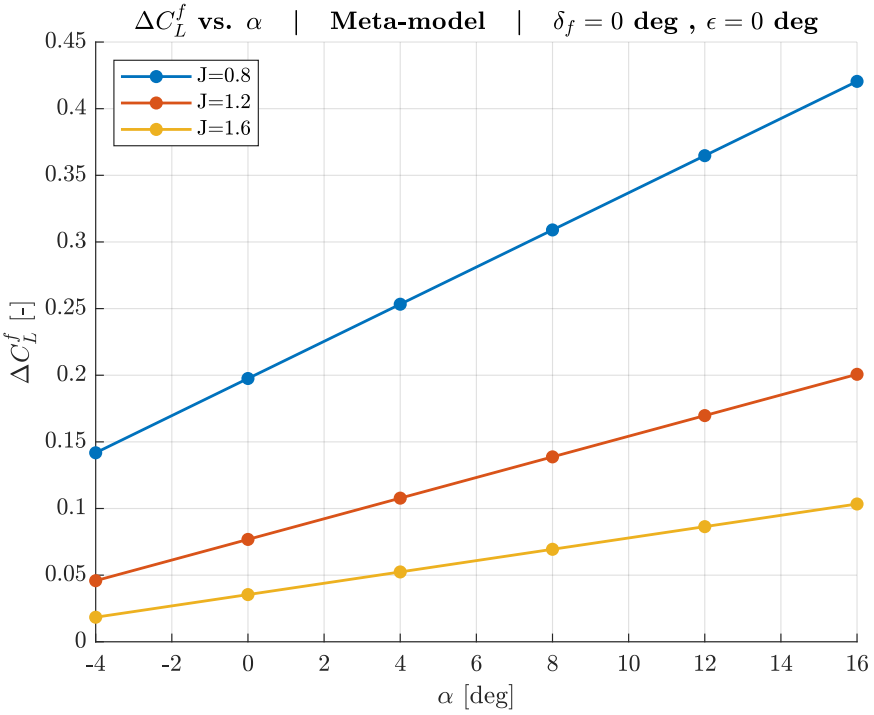

Fig. 5.11: Lift coefficient increment at a fixed propeller tilt ($\delta_f = 0°$, $\epsilon = 0°$).

Comparing the lift increments in Fig. 5.10 and Fig. 5.11, or even more looking at the drag increments in Fig. 5.12 and Fig. 5.13, recalls the different

sensitivities to propeller tilt and advance ratio. The range of increments covered by changing the former is significantly narrower than that covered by varying the latter, even recalling that the sensitivity to the propeller tilt is higher at $J = 0.8$. In Fig. 5.13, the yellow line, corresponding to $J = 1.6$, i.e., the condition where HLPs are less effective, is almost constant with the AoA and very close to the 12 nacelles drag contribution.

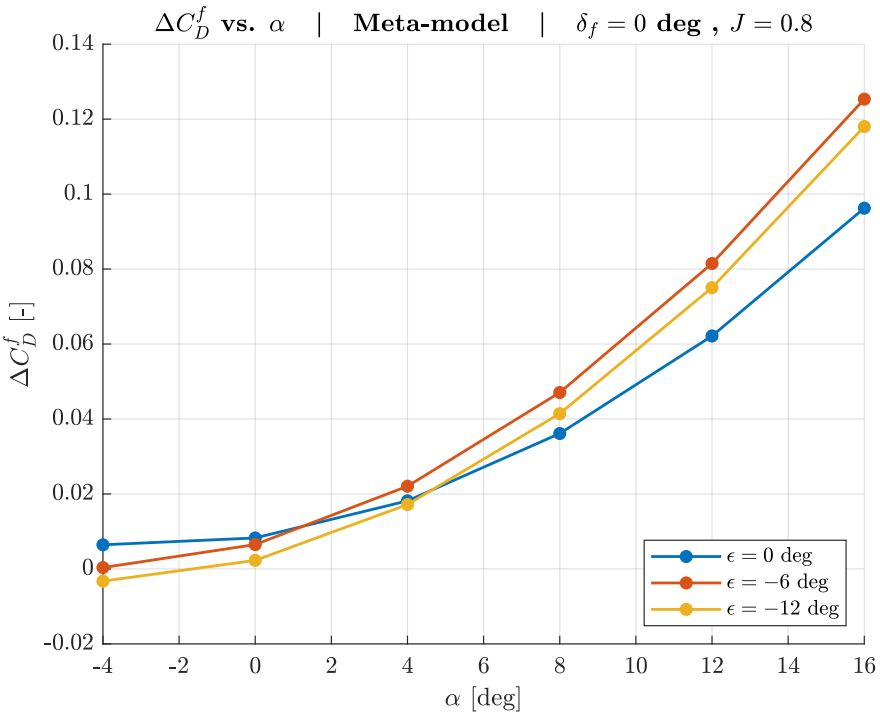

Fig. 5.12: Drag coefficient increment at a fixed advance ratio ($\delta_f = 0°$, $J = 0.8$).

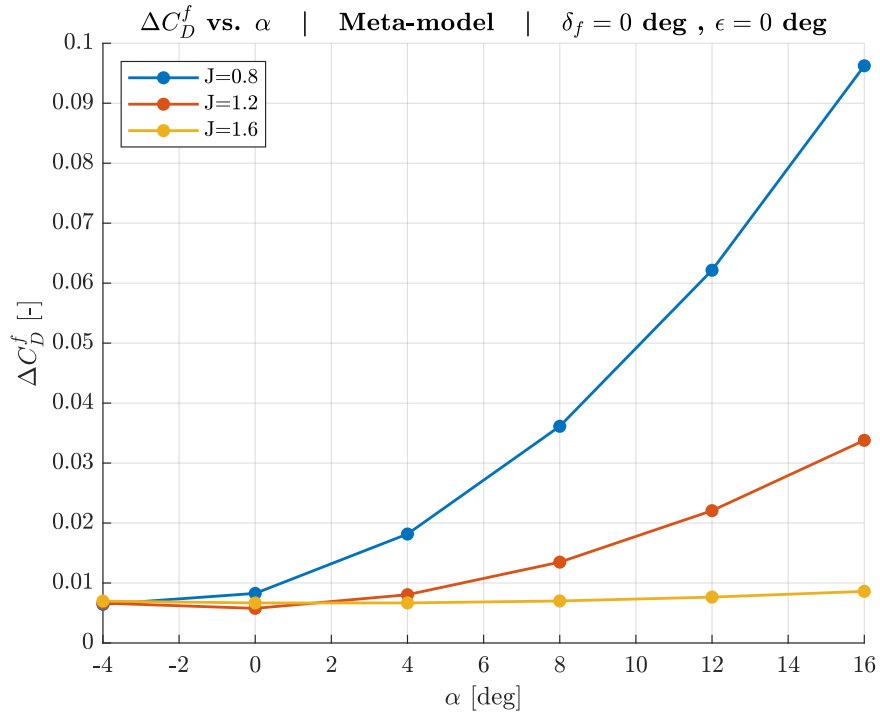

Fig. 5.13: Drag coefficient increment at a fixed propeller tilt ($\delta_f = 0°$, $\epsilon = 0°$).

Finally, Fig. 5.14 and Fig. 5.15 show the individual propeller contributions, IPC for brevity, composing the lift and drag increments in a specific condition, e.g., zero propeller tilt and an advance ratio of 0.8. No flap deflection is present, just as in all the figures above.

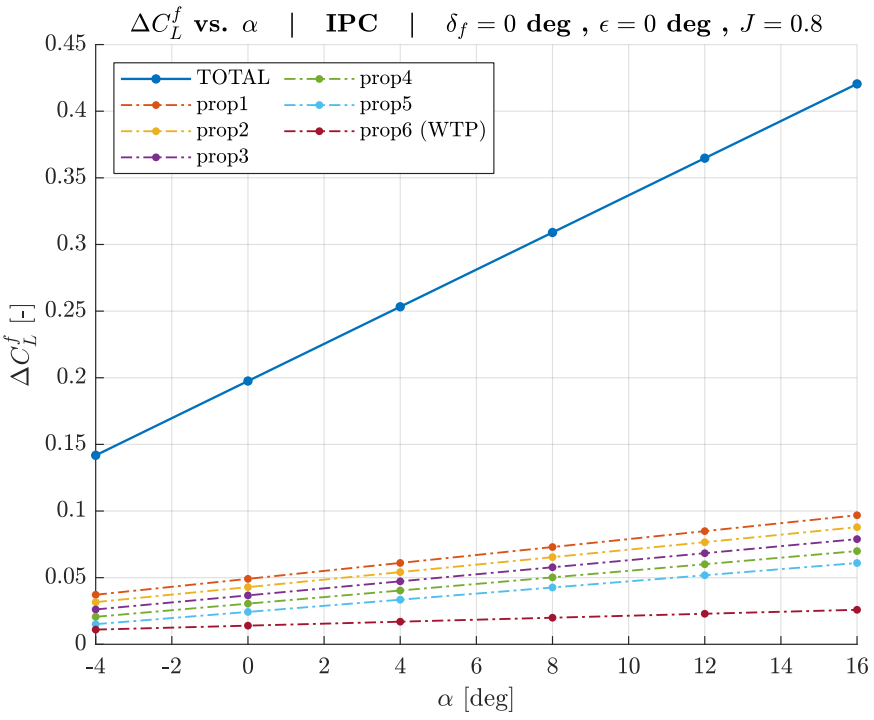

Fig. 5.14: Lift coefficient increment (IPC breakdown).

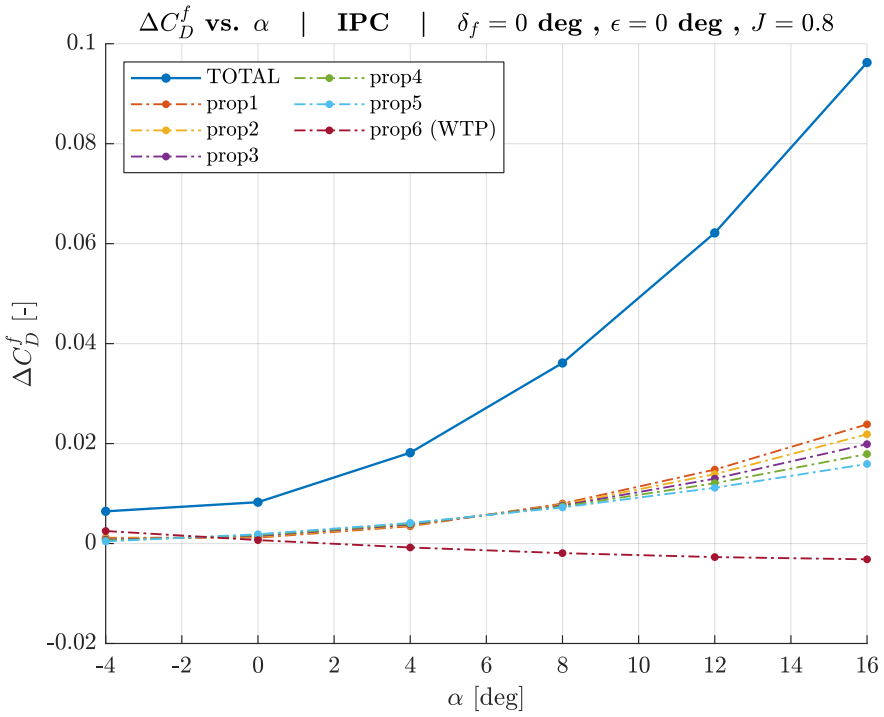

Fig. 5.15: Drag coefficient increment (IPC breakdown).

In both figures, the WTPs contributions are clearly distinguishable from the other propellers contributions: the lift increment provided by WTPs is almost negligible, while the drag increment is even slightly negative, proving WTP effectiveness in contrasting induced drag.

5.2 TITAN sizing procedure

TITAN is a tool for preliminary aircraft sizing developed at Politecnico di Milano. As shown in Fig. 5.16, it integrates Hyperion, a conceptual design procedure for hybrid aircraft, with Argos, responsible for the preliminary sizing of the main components of the airplane. For further details, the reader may refer to [29], which also describes the actual implementation of individual modules.

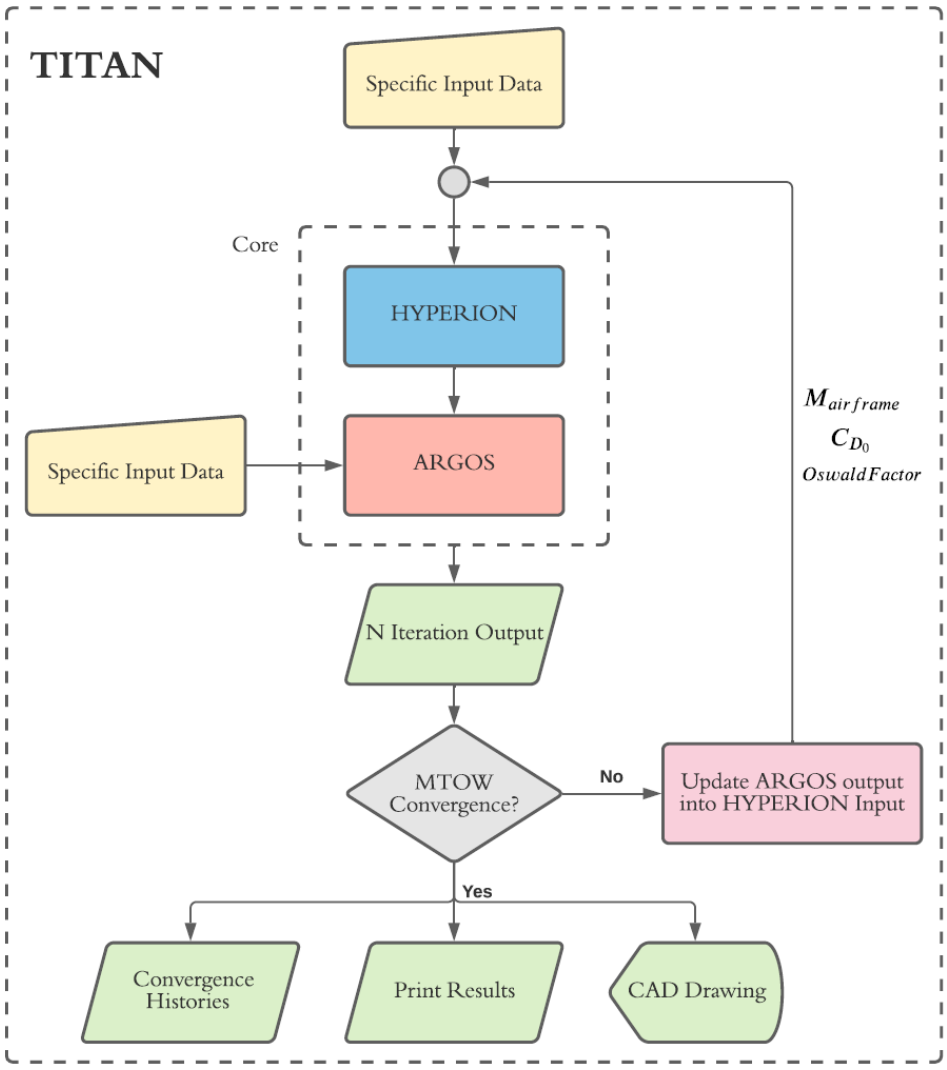

Fig. 5.16: TITAN architecture [29].

TITAN is a proven and reliable tool that integrates several procedures written over many years; therefore, preserving its architecture is crucial. The present work thus enforces a modular approach, featuring some plug-in

methods which add new aspects of the DEP system into the existing design loop.

5.2.1 Current architecture

Hyperion input file contains several parameters, like the maximum lift coefficients in all possible flap configurations; their values, however, despite being selected wisely, are merely assumptions. Verifying if these values are achievable, as well as sizing the individual components to match them, is then the main task of Argos.

Hyperion implements the approach proposed by De Vries [10], based in turn on the so-called Patterson's method [7], to estimate the increments of both C_L and C_D. On the other hand, Argos currently does not model the aero-propulsive interaction proper to a DEP aircraft. In other words, Hyperion models the effects of the HLPs while sizing the aircraft enforcing the typical operational constraints; Argos, however, cannot design the DEP system, and thus it implicitly assumes that the lift augmentation estimate of Hyperion is correct.

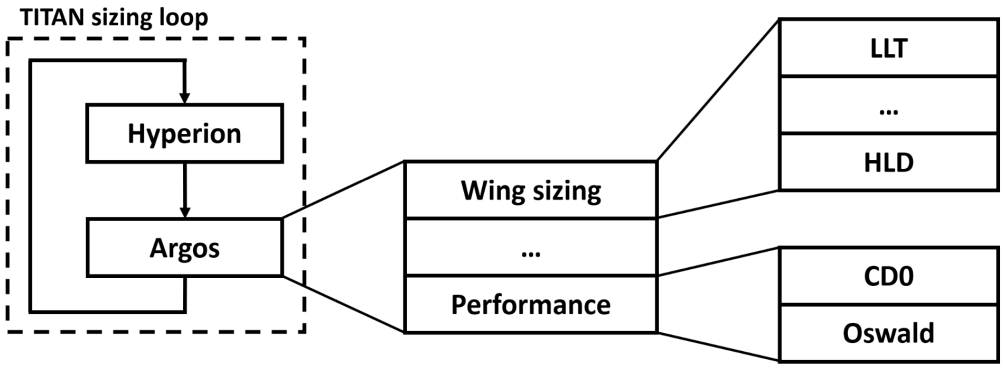

Fig. 5.17: Current Argos architecture.

Fig. 5.17 briefly presents the current architecture of Argos. Only those modules relevant for the meta-model development are listed. In detail:

- The **LLT module** sizes the wing selecting the optimal twist and taper to minimize the induced drag for cruise.
- The **HLD module** sizes the flaps to ensure that the unblown wing lift coefficient increments specified in the Hyperion input files are attainable.
- The **Performance module** estimates a parabolic polar, later fed to Hyperion for the next iteration.

5.2.2 Proposed architecture

Fig. 5.18 shows the proposed architecture of Argos, highlighting the changes with respect to its current version. To preserve modularity, TITAN integrates the new functions without replacing the existing ones. The sizing routine will run the new procedures only if a meta-model dataset is present and specified in TITAN main file; otherwise, it will simply run the code as before the introduction of these new features.

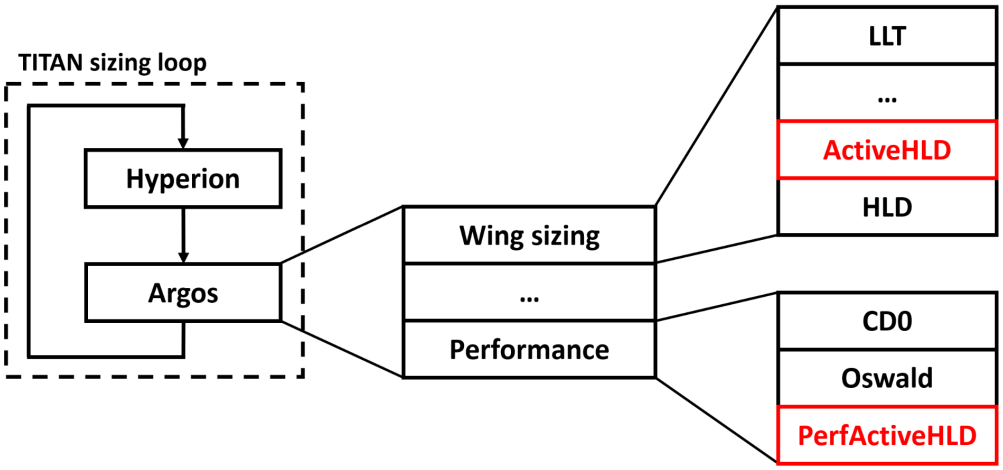

Fig. 5.18: Proposed Argos architecture.

The main additions to the current architecture of Argos are the two functions highlighted in red in Fig. 5.18:

- The **ActiveHLD module** computes the propeller operative settings, i.e., their RPM, to obtain the lift increments estimated by Patterson's method in Hyperion.
- The **PerfActiveHLD module**, given the HLP settings determined by ActiveHLD, updates the parabolic polars generated by the existing methods adding the contributions of the DEP system.

Section 6.1 provides further details regarding the implementation of the code, including the additional procedures not listed here but fundamental for the preprocessing of the numerical campaign results.

Chapter 6

Implementation and results

The present chapter provides all the details regarding the implementation into TITAN of the features briefly anticipated in Section 5.2.2. It also illustrates the results of the modified sizing procedure and compares them with those produced by the current version of Argos.

6.1 Proposed architecture implementation

This section presents the most significant changes introduced to Argos current architecture aiming to include the previously derived meta-model in TITAN. Discussing minor variations to the code made to load the dataset or print the additional outputs is not within the scope of this section.

6.1.1 Preprocessing routines

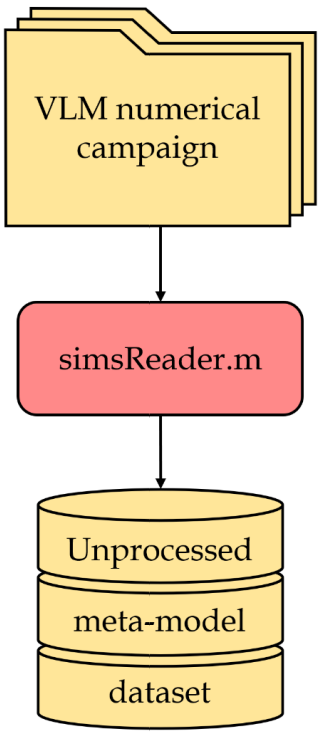

Fig. 6.1: Simulation result reader.

The first step of data processing consists of extracting the results of the numerical campaign from the simulations output files. Since all the studies presented in this thesis rely on the VSPAero VLM software, the code implemented here is consistent with how this tool saves its results. Reading data produced by other VLM codes will require changes to this script. Future numerical campaigns may investigate the effects of more parameters than those considered for the present dataset, e.g., the flap deflection; the user should then edit the preprocessing scripts to include those new quantities among those marked as *custom parameters*.

The reading time, i.e., even a few minutes if data points are very numerous, combined with the possibility to use different VLM tools, are the two reasons that led to implementing the reader in a separate script from the other preprocessing functions.

Fig. 6.1 illustrates the architecture of the simulation reader module. It inspects the folders containing the numerical campaign, extracts the required data from the output files of each simulation, averages the values on the last propeller revolution, and eventually saves all the results in a structured manner in a Matlab® MAT-file. The user can place *simReader.m* wherever is convenient, recalling to transfer the resulting MAT-file in the *VLMsims* folder inside TITAN main folder.

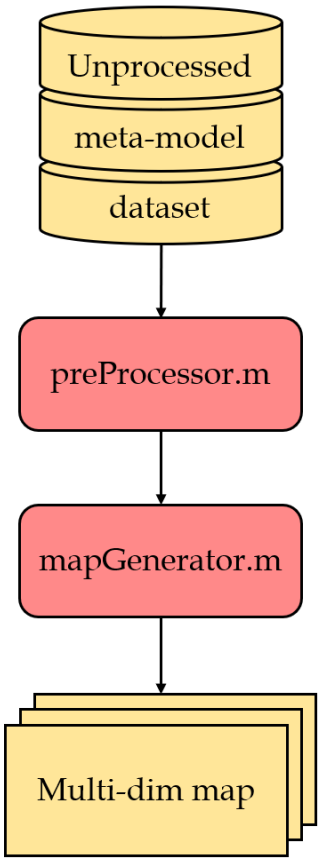

Fig. 6.2: Dataset preprocessor and multi-dimensional maps generator.

The unprocessed dataset, produced by *simReader.m*, contains the numerical campaign results in their raw form. Fig. 6.2 illustrates the procedure that

transforms those data into multi-dimensional maps usable by the sizing routine.

The first block, i.e., *preProcessor.m*, corrects the corrupted data points and applies the reduced method to extend the increments model to all the inboard propellers. Since the correction task is manual, the final user must edit the dedicated section of the script to remove the corrupted data points.

The second block, i.e., *mapGenerator.m*, finally turns the Matlab® struct containing the processed data into a series of multi-dimensional maps of quantities such as the lift and drag increments or the thrust coefficient. Those objects associate each combination of AoA, propeller ID, advance ratio, and tilt angle with a value of their output parameter. The procedure saves the multi-dimensional maps in a new MAT-file with the suffix *–P* added to its original name.

Concerning the thrust coefficient computation, the reduced approach is not applicable in the form described in Section 4.2.1 since there are no quantities analogous to the unblown lift or drag coefficients to determine. However, assuming even the thrust coefficient is linear with the spanwise position of the propeller, excluding the WTPs, it is possible to compute the C_T for all the inboard propellers starting from the same simulations used in the reduced approach.

All the procedures described above run only once to generate the required multi-dimensional maps; during the operative phase, it is sufficient to load the final MAT-file specifying its name in TITAN main script.

6.1.2 Lift augmentation module

The lift augmentation module, placed within the wing sizing section of Argos, computes the HLP settings, i.e., their RPM, to obtain the required lift increment predicted by Patterson's method in the Hyperion sizing loop. Fig. 6.3 illustrates in a very schematic manner the architecture of the lift augmentation module.

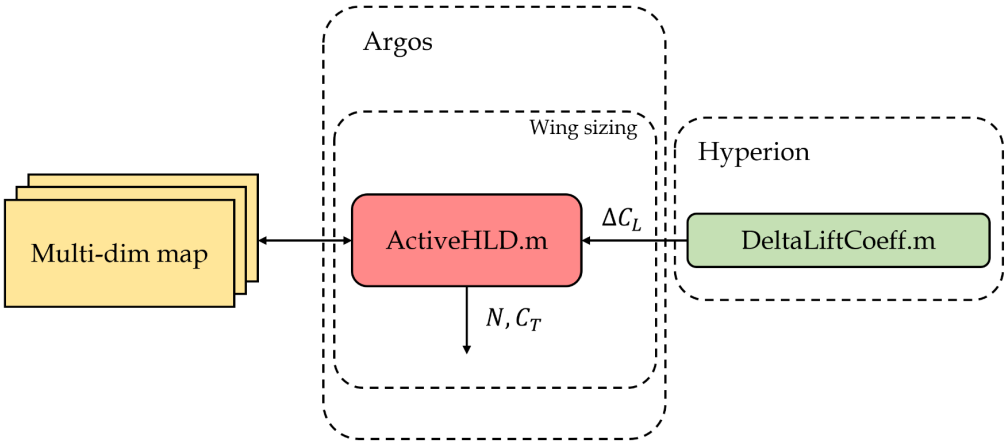

Fig. 6.3: Lift augmentation module.

The flight conditions where apply the procedure are: takeoff speed, landing speed, and stall speed, the latter considering all the three significant flap configurations. The meta-model dataset does not include any results collected on flapped layouts; the only condition that can directly apply the procedure is thus that at the stall speed with zero flap deflection. The other test points must

rely on a moderately strong assumption which is, anyway, already present in Patterson's approach. TITAN currently estimates the lift increment by applying Patterson's correction, which considers AoA and dynamic pressure variations, to the sectional lift coefficient. Downscaling the target lift increments according to the ratio between their corresponding C_{L_u} and the $C_{L_{max}}^{clean}$ allows to treat them as the lift increment at stall speed for the clean configuration. Further developments, described in Section 7.2.1, will eventually circumvent the issue thanks to a more extensive numerical campaign that includes simulations of the flapped layouts.

Going back to the actual implementation of *ActiveHLD.m*, it is possible to estimate the stall AoA starting from the unblown wing characteristics generated by exploiting the LLT. Given some more geometrical parameters also coming from the LLT module, *ActiveHLD.m* can compute the parameters required to apply the meta-model for each propeller.

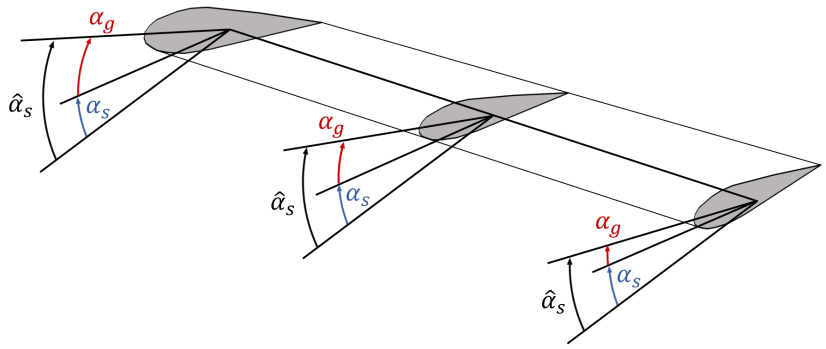

(a) local stall AoA

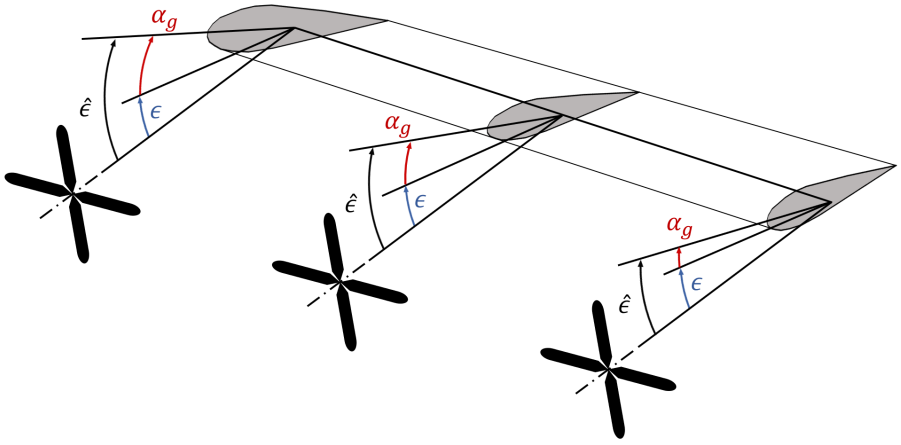

(b) local propeller tilt

Fig. 6.4: Local parameters computation.

Fig. 6.4a illustrates the concept of local stall AoA, i.e., the local AoA behind each propeller at which the entire aircraft reaches the stall. It is the sum of the stall AoA of the aircraft α_s, which is the same for all the propellers, and the angle between the local airfoil reference frame and the aircraft reference frame α_g, which varies according to twist. Its expression is the following:

$$\hat{\alpha}_s = \alpha_s + \alpha_g \tag{6.1}$$

On the other hand, Fig. 6.4b shows the concept of local propeller tilt, which has the following expression:

$$\hat{\epsilon} = \epsilon - \alpha_g \tag{6.2}$$

Similar to the stall AoA, the local propeller tilt is the sum of the global propeller tilt ϵ, defined in Hyperion input file, and the parameter accounting for the twist of the wing α_g. The minus sign is necessary since downtilt is negative by definition.

Once both the local AoA and the local tilt are known, it is possible to interpolate the meta-model dataset and extract a function of the lift increment that depends on a single variable, i.e., the advance ratio. Solving the equation for the target ΔC_L provides the required J, from which computing the propellers RPM.

Given the operative condition of the HLPs, the meta-model can also estimate the total thrust coefficient produced by the DEP system. The drag polar correction module will later take care of this data.

6.1.3 Drag polar correction module

The primary goal of this new function is to correct the drag polars taking into account the currently neglected blowing effects. Hyperion estimates the drag increments according to De Vries' approach, i.e., computing an increment for the friction drag and one for the induced drag. The former is almost negligible and only takes into account the higher dynamic pressure; the latter extends the original polar toward higher C_L without considering any change of the Oswald factor. The resulting curve is thus a mere extension of the unblown one over a broader range of lift coefficients.

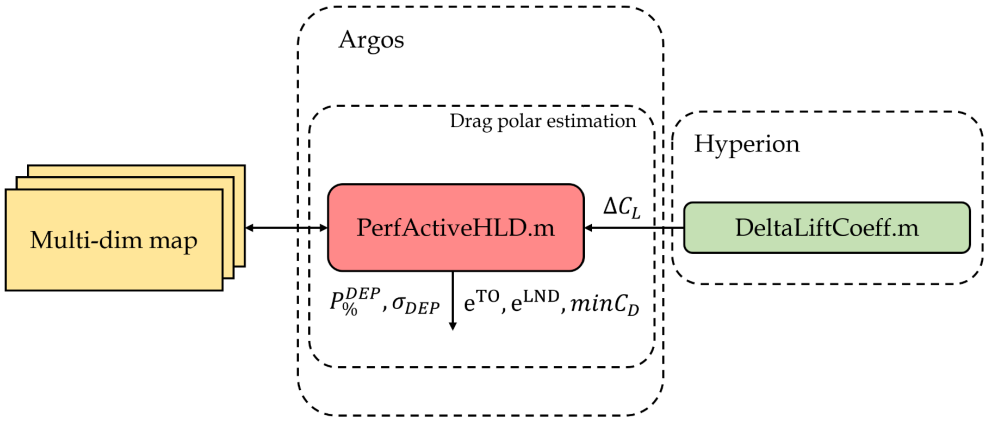

Fig. 6.5: Drag polar correction module.

Fig. 6.5 illustrates the architecture of the drag polar correction module, placed in the last section of Argos loop, i.e., the one dedicated to polar estimation.

PerfActiveHLD.m computes a correction for the clean configuration polar, later extended to the two flapped layouts. A procedure analogous to the one implemented in *ActiveHLD.m* computes the advance ratio required to obtain the lift increments estimated by Patterson's method. Once the parameters are known, the meta-model can provide the drag increments to correct the unblown polar. The function finally applies the usual parabolic approximation,

obtaining a correction for both the minimum drag coefficient and the Oswald factor. The former primarily depends on the nacelles drag contribution, which TITAN currently neglects; the latter contains the effects of the wing blowing, including the one of the WTPs. Minimum drag correction applies to the polars of all the three considered configurations; Oswald factor correction applies instead only to the flapped layouts since HLPs typically do not operate during the cruise phase. Further developments, described in Section 7.2.1, will eventually circumvent the issue thanks to a more extensive numerical campaign that includes simulations of the flapped layouts.

Being at the end of the functions cascade, when all the other parameters are already defined, allows *PerfActiveHLD.m* to take advantage of the DEP thrust coefficient previously computed by *ActiveHLD.m*, providing an estimate of DEP power ratio and DEP throttle parameter. For each of the five significant flight conditions considered in the lift augmentation module, the following formula provides an estimate of the DEP power ratio, i.e., the ratio between the DEP available power and the required power in the specified condition:

$$P_{\%}^{DEP} = \frac{P_a^{DEP}}{P_r} = \frac{T^{DEP}V}{DV} = \frac{2d^2}{SJ^2}\frac{C_T^{DEP}}{C_D} \tag{6.3}$$

The required power considers the updated drag polar and includes the contribution of flaps and landing gear when necessary. The equation below is the expression of the DEP throttle parameter, i.e., the ratio between the actual DEP shaft power in the specified flight condition and the MCP of the DEP system:

$$\sigma_{DEP} = \frac{T^{DEP}V}{\eta_p^{DEP}P_b^{DEP}} = \frac{\rho V^3 d^2 C_T^{DEP}}{J^2 \eta_p^{DEP} P_b^{DEP}} \tag{6.4}$$

The method assumes a propulsive efficiency of 0.6 for the HLPs, i.e., the value initially specified in Hyperion input file.

6.2 TITAN solutions comparison

This section finally presents the effects of the DEP meta-model on the solutions generated by TITAN, i.e., the aircraft sizing routine developed at Politecnico di Milano. The first subsection illustrates the reference solution for UNIFIER19 configuration C7A-HARW, obtained with the current version of TITAN. The second subsection, instead, shows the solution produced by the updated version, which implements the proposed architecture of Argos previously described.

6.2.1 Current architecture solution

As stated in Section 4.1, configuration C7A-HARW is a partially modified version of the original configuration C7A; the new design features a significant reduction of the wing surface, associated with a higher aspect ratio.

A reference TITAN solution for UNIFIER19 configuration C7A-HARW, which is necessary to quantify the impact the meta-model has on it, was initially unavailable. However, since a solution for the original C7A and the OpenVSP model of the modified C7A-HARW were available, sizing the latter in TITAN was relatively straightforward; only minor changes to Hyperion and Argos input files were necessary.

Single hop range	350 km
Number of hops	6
Cruise altitude	4000 ft
Cruise speed	141.4 kn
Diversion range	100 km
Loitering time	45 min

Tab. 6.1: Standard multi-hop mission used for the sizing of UNIFIER19.

The sizing mission is the standard multi-hop mission used for configuration C7A; Tab. 6.1 briefly summarizes its main parameters. The mission profile prescribes six hops of 350 km each, at 4000 ft and 141.4 kn; a 100 km diversion to an alternate airport and a loiter of 45 minutes follow the first hop. A complete list of all mission requirements and design constraints is available in [28].

Apart from updating the geometrical parameters according to the OpenVSP model, like the aspect ratio or the propeller tilt, to reduce the wing surface as required without having detrimental effects on the MTOM, both the wing loading and the maximum lift coefficients specified in the input files need to raise by 29.4%. The result is an aircraft that is only 1.5% heavier than the original C7A.

Fig. 6.6 compares the geometries of configuration C7A-HARW. Fig. 6.6a shows the OpenVSP model provided by PVS, which represents the final layout of UNIFIER19. Fig. 6.6b illustrates the geometry generated by TITAN. The empennage, a V-tail for the final layout and a conventional tail for the TITAN solution, represents the most evident discrepancy between the two geometries.

	Final	**TITAN (current)**
α_t	−3.0°	−7.1°
i_w	3.0°	6.0°
S	28.90 m²	28.29 m²
t/c	0.129 ÷ 0.195	0.163
λ	0.370	0.390
Γ	−2.0°	−1.1°

Tab. 6.2: Discrepancies between Final and TITAN geometries of UNIFIER19 configuration C7A-HARW.

Tab. 6.2 reports further discrepancies which are not appreciable by just looking at the figures. In general, the differences are not significant, especially considering that the final layout comes from a further design refinement, while the TITAN solution is the mere result of an automatic sizing procedure. The thickness ratio is an input for TITAN and not part of its solution since the sizing routine does not have control over its value. The t/c discrepancy is thus just

due to a limitation of Argos since the current LLT method is not able to model a wing featuring spanwise variable airfoils.

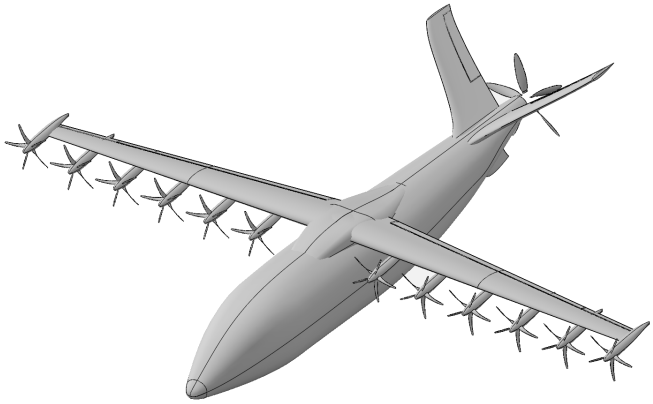

(a) Final geometry

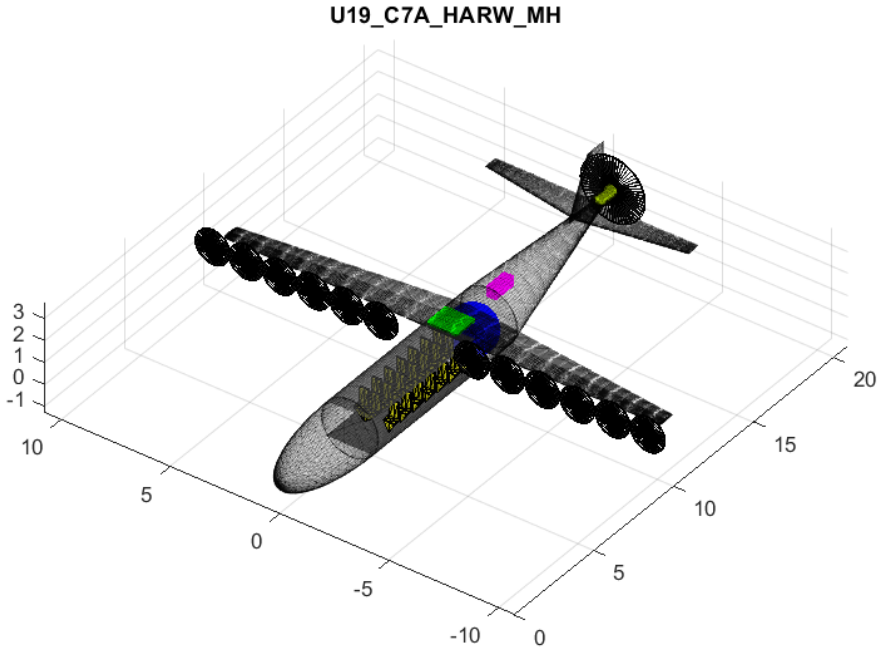

(b) TITAN geometry

Fig. 6.6: Comparison between Final and TITAN geometries of UNIFIER19 configuration C7A-HARW.

M_{TO}	8071.6 kg
S	28.29 m^2
P_b	1304.9 kW
P_b^{DEP}	652.5 kW
M_{LH_2}	372.1 kg

Tab. 6.3: TITAN solution for configuration C7A-HARW (current Argos architecture).

Tab. 6.3 summarises some of the most significant outputs TITAN provides at the end of the sizing process. The MTOM of configuration C7A-HARW, as already noted, is just 1.5% higher than the one of the original C7A. However, thanks to the optimized wing, the amount of liquid hydrogen required for the multi-hop mission is 1.0% lower. Finally, the shaft power of the DEP system is precisely half the total shaft power, as prescribed in Hyperion input file.

Tab. 6.4 reports the parameters describing the parabolic drag polars produced by TITAN for some significant flight conditions. Argos updates the estimate at the end of each iteration, feeding Hyperion with the latest results. However, the performance module implemented in Argos only corrects the Oswald factor associated with the clean configuration; those related to the flapped layouts remain constant and equal to the values assumed in the Hyperion input file.

	$minC_D$	e
Clean	0.0402	0.658
Takeoff	0.0415	0.800
Landing	0.0734	0.750

Tab. 6.4: Drag polar parameters considered by the current Argos architecture.

6.2.2 Proposed architecture solution

This section presents the solution for UNIFIER19 configuration C7A-HARW produced by the new TITAN version, which implements the proposed architecture extensively described in Section 6.1. The sizing mission remains the same, like any other requirement or constraint; both the Hyperion and the Argos input files are thus left untouched.

M_{TO}	8211.2 kg
S	28.74 m^2
P_b	1325.5 kW
P_b^{DEP}	662.8 kW
M_{LH_2}	424.5 kg

Tab. 6.5: TITAN solution for configuration C7A-HARW (proposed Argos architecture).

Tab. 6.5 briefly summarises the solution produced by the updated version of TITAN. The MTOM, the wing surface, and the shaft powers increase by approximately 1.6%, compared to those estimated by the current version of TITAN. On the other hand, the fuel mass raises significantly, i.e., by 14.1%; a more detailed analysis concerning mass increments is at the end of this section.

Tab. 6.6 presents the first contribution introduced by the meta-model implemented in the proposed architecture: an estimate, in some significant flight conditions, of the propeller settings required to achieve the lift increment promised by Patterson's method in Hyperion. As the considered condition becomes more challenging, i.e., requires a higher lift augmentation, propeller

RPM increases. This aspect is coherent with the fact that a higher RPM reduces the advance ratio and thus improves the blowing effectiveness. Apart from propeller speed, Tab. 6.6 also presents an estimate of the DEP throttle parameter and the DEP power ratio for all the considered flight conditions.

The methods introduced in the proposed architecture aim to compute the minimum propeller settings to obtain the desired lift augmentation; however, the actual settings may differ since they must consider other requirements. For example, motors typically operate at their maximum peak power during takeoff, i.e., at 125% of the MCP, instead of the 37% required to increase lift. Future developments may implement DEP control strategies and compute the actual propeller settings considering those further constraints.

	N	σ_{DEP}	$P_{\%}^{DEP}$
@ stall (clean)	1285 RPM	28%	30%
@ TO speed	1299 RPM	37%	39%
@ LND speed	1315 RPM	41%	37%
@ stall (TO)	1390 RPM	51%	60%
@ stall (LND)	1573 RPM	86%	95%

Tab. 6.6: HLP settings to obtain the desired lift increments in some flight conditions.

The throttle parameter is the ratio between DEP shaft power and DEP maximum continuous power. The fact that it always remains below 86% confirms that the DEP system can provide the required lift augmentation in all the considered conditions, preserving a margin of at least 14% with respect to the maximum continuous power. Given the uncertainty of the unvalidated UNIFIER19 thrust coefficient estimates, reducing this already small margin by optimizing the mass of the DEP motors is left to future developments.

The DEP power ratio is the ratio between the DEP available power and the total required power in a specific flight condition; recall that required power only includes the energy dissipated through aerodynamic drag and neglects any other contribution. Since HLPs generally operate at a high regime during landing, when significant lift augmentation is required, but considering that excess power is highly undesirable in this phase, power management represents a concern for DEP aircraft, already addressed by Patterson in [16]; drastic solutions may include airbrakes or other drag augmentation devices. The proposed architecture of Argos does not deal extensively with this issue; however, it verifies that $P_{\%}^{DEP}$ never exceeds 100%, i.e., that the DEP system never produces an undesirable excess power.

Tab. 6.7 presents the parameters describing the parabolic polar computed by TITAN and used to simulate the mission profile and estimate the aircraft performance. The 12 HLP nacelles introduce a parasite drag penalty of 0.0087, present in the polars of all the three considered configurations. On the other hand, the wing blowing, including the effect of the WTPs, reduces the induced drag and raises the Oswald factor. Since the DEP system of UNIFIER19 does not operate during the cruise phase, the Oswald factor correction only applies to the polars of the flapped configurations; the clean layout still presents the same e estimated by the current version of TITAN.

	$minC_D$	e
Clean	0.0489	0.658
Takeoff	0.0503	0.876
Landing	0.0821	0.826

Tab. 6.7: Drag polar parameters corrected with the proposed Argos architecture.

One of the main outputs of aircraft sizing routines is the so-called mass breakdown, i.e., an estimate of the masses of the individual aircraft components. Therefore, it is worth noting how the changes introduced in the present thesis modify this result. After examing the complete mass breakdown, it is possible to divide the items into four categories, depending on the impact the changes produce on their masses. The four categories are:

- **Crew + Payload**: Hyperion input file fixes the weights of those items that thus remain unchanged.
- **Structure + Systems**: it groups all the structural components and the onboard systems like the wing, the fuselage, the landing gear, the electrical system, etc. The changes have a limited impact on their masses.
- **LH2 related**: it comprises all the items concerning liquid hydrogen, including the fuel tank, the PGS, and the fuel itself. The changes introduce significant penalties to their masses.
- **Battery**: is the only component whose mass reduces thanks to the changes introduced with the proposed architecture.

Tab. 6.8 quantifies the mass increment breakdown, reporting the absolute and the relative variations between the results of the current TITAN version and the one proposed in this thesis. Fig. 6.7 helps to visualize the increments illustrating these relative variations.

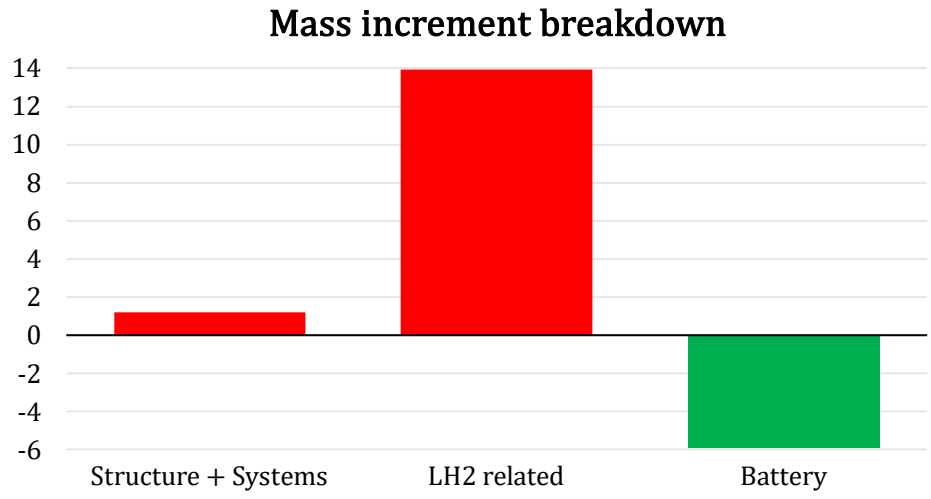

Fig. 6.7: Mass increment breakdown.

	Current	Proposed	Variation	
	[kg]	[kg]	[kg]	[%]
Structure + Systems	4086.7	4136.1	49.4	1.2
Crew + Payload	2380.0	2380.0	0.0	0.0
LH2 related	938.4	1069.3	130.9	13.9
Battery	681.7	641.3	−40.4	−5.9
MTOM	8086.8	8226.7	139.9	1.7

Tab. 6.8: Mass increment breakdown.

The current version of TITAN completely neglects the drag contribution of the HLP nacelles; this translates into a moderate underestimation of the energy consumption, which ultimately leads to the 13.9% increment of the *LH2 related* masses when passing from the current to the proposed version of TITAN. The required power increment, associated with the higher drag, raises not only the weight of the hydrogen and its tank but also the mass of the power generation system, which has to turn the fuel into electric energy at a higher pace. Since all these components present weight increments between 12% and 16%, they all fall within the same category, named *LH2 related* after them.

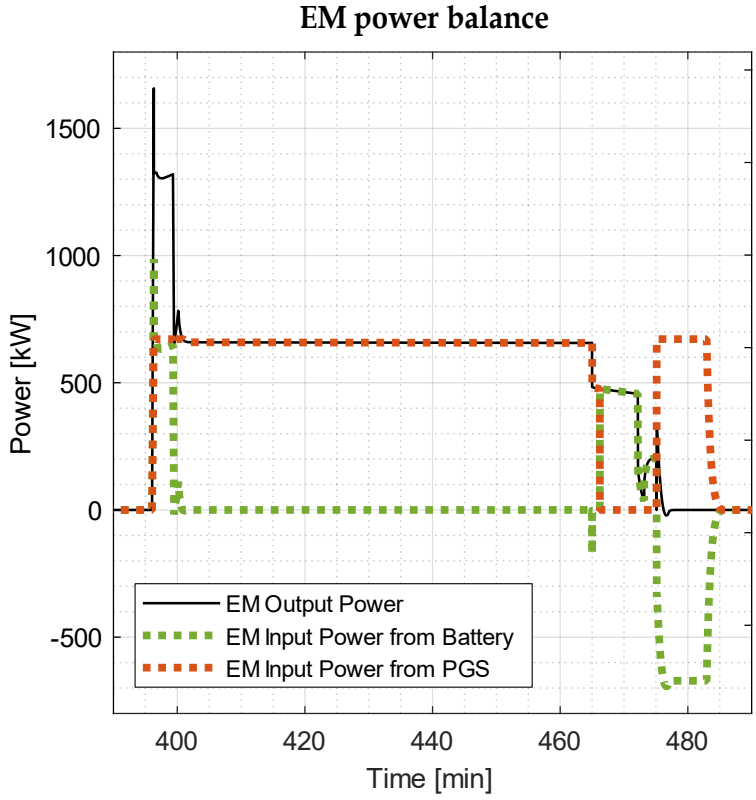

Fig. 6.8: EM power balance of UNIFIER19 configuration C7A-HARW (proposed Argos architecture).

On the other hand, a more powerful PGS, combined with the higher Oswald factor computed by the new procedure considering the blowing effects of the HLPs, reduces the power the battery has to deliver during takeoff, thus lowering its mass by about 6%. To better explain this last aspect, Fig. 6.8 shows the power balance of UNIFIER19 electric motors during the 4th hop of the considered mission profile. The power required during the cruise phase, which corresponds to the central portion of the timeline, clearly sizes the PGS, which keeps running at full throttle for a quiet extended time while the power delivered to the EM by the battery is zero. On the other hand, the joint supply by both PGS and battery provides the power peak on the right of the timeline, corresponding to takeoff and climb. Any combination of a lower demand peak and a higher PGS power output will thus lead to a lighter and less powerful battery.

The reduction of the battery mass cannot counteract the *LH2 related* increment; the final result is thus a slight increase of all the structural and system weights: 1.2% considering the entire *Structure+System* category and up to 2.8% considering individual components.

The overall mass increment, i.e., the increment of the MTOM, is 1.7%. The current version of TITAN is thus slightly less conservative than the proposed one, which is coherent with the drag contribution of the HLP nacelles, so far neglected by the sizing routine.

Chapter 7

Conclusions and Future Developments

The present chapter drafts the conclusion of this thesis and proposes some ideas for future developments of the work performed so far.

7.1 Conclusions

This section addresses the three objectives initially defined in Section 1.2 by presenting the main results and findings obtained during the activity for writing this thesis. Each of the following subsections approaches one of the three objectives.

7.1.1 Validation of a mid-fidelity method

The thesis started with a survey of low- and mid-fidelity methods suitable to include DEP aero-propulsive interaction in an existing preliminary aircraft sizing tool. The Vortex Lattice Method was the ultimate choice, offering a good compromise between accuracy and rapidity. VSPAero, in particular, was the selected tool since it also provides estimates of the parasite drag, but any other VLM solver may be suitable for the task if adequately validated.

Concerning propeller modeling, the purely VLM approach, which implements the actual blade geometry, soon proved its superiority over the actuator disk approach. The former can capture the complete coupling between the wing and the propellers, despite being significantly slower than the latter.

Validation, carried out against experimental data collected in [22], showed that the selected methodology provides sufficiently accurate results for its integration within a preliminary sizing routine. Further studies analyzed the capability of the purely VLM approach to deal with setups featuring multiple, overlapping, or counter-rotating propellers. The high computational cost associated with MPC simulations suggested developing a reduced approach to lower the computational costs of an extended numerical campaign while preserving the accuracy of the original simulations.

7.1.2 Development of a DEP meta-model

The satisfactory results of the purely VLM approach for all the tested conditions and setups suggested developing the DEP meta-model relying on this

methodology. The dimensional analysis of a generic force coefficient provided a consistent framework for the construction of the meta-model dataset.

The selection of UNIFIER19 configuration C7A-HARW as the reference geometry for the numerical campaign reduces the design space to three parameters: the AoA, the propeller tilt, and the advance ratio. The dataset, made of 216 data points divided into 36 raw data curves, generates nine sets of polars representing the multi-dimensional maps of increments and coefficients. Correcting the few corrupted data points requires human judgment and is thus left manual.

The reduced approach, presented in Section 4.2.1, proved its effectiveness in lowering the computational costs of the numerical campaign by about 50% without compromising the accuracy. Given the negligible dispersion of the unblown polars extrapolated from simulations featuring the same propeller tilt, a further reduction of the costs is achievable by scrapping some of the cases exclusively used for the extrapolation (prop2&5).

7.1.3 Integration of the developed meta-model

The developed meta-model is successfully implemented in TITAN, the preliminary aircraft sizing routine of Politecnico di Milano. Preprocessing tools, able to deal even with future and more extended numerical campaigns, were also developed. The proposed architecture integrates the following main features: the computation of HLP settings to obtain the desired lift augmentation; and the estimation of corrected drag polars that considers the presence of the DEP system. The results confirm that the ranges selected for the meta-model parameters are adequate, neither too narrow nor too broad; they cover all the design space without, at the same time, wasting resources in the construction of a pointlessly large map.

UNIFIER19 configuration C7A-HARW is the setup selected for the test; TITAN sizes the aircraft both with and without the meta-model. The solution produced by the updated version exhibits a MTOM increment of 1.7%, mainly related to the drag contribution of the DEP nacelles, previously neglected by Argos.

The presented approach allows running simulations in advance without any noticeable increase in the sizing loop computational costs. The method is thus suitable for including a mid-fidelity model of the DEP aero-propulsive interaction in the design process while preserving the rapidity required for a preliminary sizing tool.

The ideas implemented in this thesis are relatively few, considering the potential, possibly exploitable by future developments, offered by the meta-model concept in general. Section 7.2 eventually presents more proposals to improve this approach by implementing new features, expanding the dataset, etc.

7.2 Future developments

This section includes some ideas about future developments of the present thesis. The first proposal concerns additional features for TITAN, unluckily not developed due to the lack of time to run the new numerical campaign. The second proposal is for a function dedicated to DEP motor scheduling. The third idea is an automatic procedure to set up the OpenVSP geometrical models and

the VSPAero simulations, increasing the efficiency of the currently most time-consuming phase of the entire process.

7.2.1 Other proposed architectures

The proposed architecture implemented in this thesis considers separately the lift increments induced by flap deflection and HLP blowing effects. A more comprehensive approach may consider the overall lift increment computed running simulations of blown flapped wing.

The HLD feature embedded in VSPAero models flaps as simple Plain flaps. The possibility of modeling flaps in other VLM tools, or the feasibility of implementing more complex geometries, such as Fowler flaps, should be the objectives of a future study.

Fig. 7.1 highlights in red the additional functions with respect to the current Argos architecture required to implement the second proposed approach. In details:

- The **OverallHLD module** replaces the ActiveHLD and the HLD functions present in the first proposed architecture. The procedure returns the combination of propeller settings and flap deflection to match the required lift increment.
- The **PerfOverallHLD module** replaces the PerfActiveHLD module introduced in the first proposed architecture. Instead of extending the clean configuration results to flapped layouts, this procedure computes the drag polar corrections on the actual flapped geometry, thus already including the additional parasite C_D.

When the required dataset is unavailable, the new functions will just bypass the new features and call the old routines.

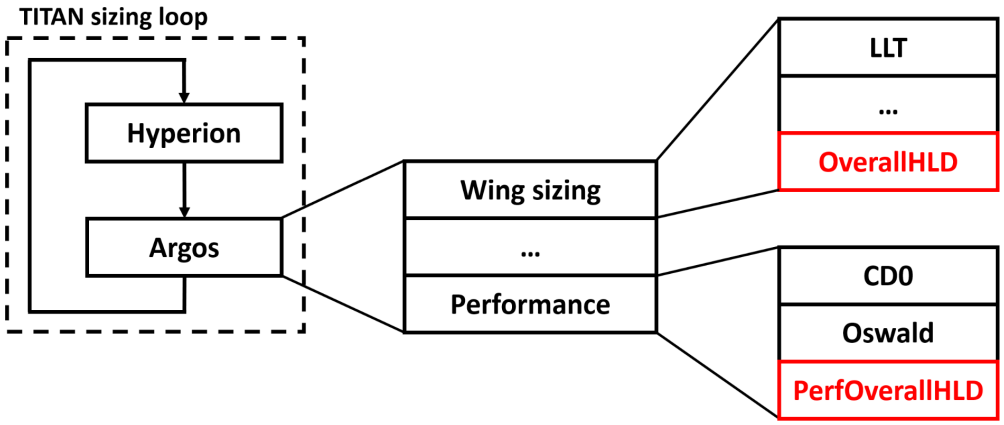

Fig. 7.1: Proposed Argos architecture #2.

The major drawback of such an approach is the extent of the numerical campaign required to run it, which discouraged its implementation in little the time left for this thesis. Adding the flap deflection δ_f to the parameters to vary during the study dramatically impacts the number of the simulations: two values of δ_f, plus the clean configuration, will make the campaign three times larger.

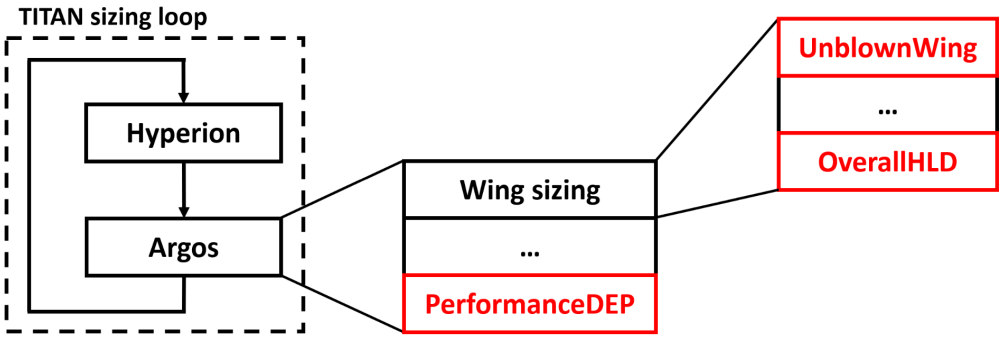

Fig. 7.2: Proposed Argos architecture #3.

The third proposed architecture, shown in Fig. 7.2, represents the last step of the Argos evolution envisioned during this thesis. Currently, the unblown wing aerodynamic modeling relies entirely on low-order methods, such as the Lifting Line Theory for lift, and basic algebraic procedures for C_{D_0} and the Oswald factor estimation. The additional procedures with respect to the current Argos architecture, highlighted in red in Fig. 7.2, are the following:

- The **UnblownWing module** sizes the wing selecting the optimal twist and taper to minimize the induced drag for cruise. It replaces the LLT module relying on a multi-dimensional map derived from a dedicated VLM numerical campaign of the unblown wing. This function will allow modeling more complex wing geometries than those supported by the current implementation of LLT, like those featuring different airfoils across the wing span.
- The **OverallHLD module** is identical to the one described above for the second proposed architecture.
- The **PerformanceDEP module** entirely replaces the several functions which currently estimate each parameter of the parabolic drag polar separately. If the unblown layout used for the simulations does not include other components than the wing, the estimate of their parasite drag contributions still relies on the old method.

As for the previous approach, when the required dataset is unavailable, the new functions will bypass the new features and call the old routines. Given the rapidity of steady VLM simulations, it is possible to run a relatively extended numerical campaign involving several design parameters not considered so far, like twist, taper, etc. If the unblown simulations include the entire geometry of the aircraft instead of the isolated wing, and the selected VLM tool can also estimate parasite drag, just as VSPAero, the new performance module will be able to compute an estimate of the overall polar curve.

7.2.2 DEP motors scheduling

The changes to Argos architecture proposed in this thesis aim to provide a bunch of meaningful information also useful for DEP motors scheduling, like the minimum RPM required to produce the desired lift increments, DEP power ratio, and DEP throttle parameter. However, the actual scheduling is a complex multidisciplinary task that lies outside the scope of the present thesis and needs to address also safety concerns. For example, the DEP system should prevent

sudden changes in lift augmentation; or avoid conditions of excess power during critical phases such as landing.

The architecture of the presented meta-model offers the possibility to implement functions that enforce those constraints and produce detailed scheduling for DEP motors during takeoff, climb, approach, or landing. To achieve the required confidence in the thrust coefficients estimate, the writer suggests performing a dedicated validation on the UNIFIER19 propellers before investing any effort in developing the code.

7.2.3 Automatic simulations setup

Setting up all the simulations required by the numerical campaign is currently one of the most demanding tasks of the whole process; the procedure is entirely manual and can only partially benefit from some common-sense practices. Once a single simulation is fully ready, applying the few required changes to all its clones is pretty repetitive and straightforward, although time-consuming.

Given the ranges of the parameters to vary in the study, it is possible to speed up this phase, coding an automatic procedure that generates and sets up all the simulations. OpenVSP, i.e., the VLM software used in this thesis, includes an API written in C++ that exposes all of the functionality of the GUI to a programming interface. For further details and documentation about the API, the reader may refer to [30]. This automatic procedure will thus be able to set up both the OpenVSP models and the VSPAero simulations. Combined with the routines already implemented to run the numerical campaign and subsequently read its results, it will completely automatize the dataset construction. The author is not aware of analogous API availability for other VLM tools.

Bibliography

[1] *NASA Advanced Air Transport Technology (AATT) webpage.* URL: https://www.nasa.gov/aeroresearch/programs/aavp/aatt/.

[2] *Clean Aviation webpage.* URL: https://clean-aviation.eu/.

[3] Ole Pfeifle, Stefan Notter, Walter Fichter, Dominique P Bergmann, Jan Denzel and Strohmayer Andreas. "Verifying the Effect of Wingtip Propellers on Drag Through In-Flight Measurements". In: *Journal of Aircraft,* pp. 1-10, 2021.

[4] *NASA X-57 Maxwell webpage.* URL: https://www.nasa.gov/specials/X57/.

[5] *Lilium Air Mobility webpage.* URL: https://lilium.com/.

[6] Melvin H Snyder Jr and Glen W Zumwalt. "Effects of wingtip-mounted propellers on wing lift and induced drag". In: *Journal of Aircraft,* pp. 392-397, 1969.

[7] Michael D Patterson. "Conceptual design of high-lift propeller systems for small electric aircraft". PhD Thesis. Georgia Institute of Technology, 2016.

[8] Rob McDonald, Brandon Litherland, Justin Gravett, J.R. Gloudemans, Mark Moore, Andy Hahn, Bill Fredericks and Alex Gary. *Open Vehicle Sketch Pad (OpenVSP).* URL: http://openvsp.org/.

[9] Alessandro Sgueglia, Peter Schmollgruber, Nathalie Bartoli, Olivier Atinault, Emmanuel Benard and Joseph Morlier. "Exploration and sizing of a large passenger aircraft with distributed ducted electric fans". In: *2018 AIAA Aerospace Sciences Meeting,* p. 1745, 2018.

[10] Reynard de Vries, Malcom Brown and Roelof Vos. "Preliminary Sizing Method for Hybrid-Electric Distributed-Propulsion Aircraft". In: *Journal of Aircraft,* pp. 2172-2188, 2019.

[11] Juan P Ruscio, Joel Jezegou, Emmanuel Benard, Angel Pacheco Gomez, Paul Laonet and Raquel Alonso Castilla. "Hybrid electric distributed propulsion overall aircraft design process and models for general aviation (FAST GA)". In: *IOP Conference Series: Materials Science and Engineering,* 2021.

[12] Danilo Ciliberti, Francesco Orefice, Pierluigi Della Vecchia, Fabrizio Nicolosi and Salvatore Corcione. "An Approach To Preliminary Sizing Of Turbo-Electric Aircraft With Distributed Propulsion". In: *AIDAA XXV International Congress,* 2019.

[13] *PyTornado theory introduction webpage.* URL: `https://pytornado.readthedocs.io/en/latest/theory/`.

[14] Leo L M Veldhuis. "Review of propeller-wing aerodynamic interference". In: *24th international congress of aeronautical sciences,* 2004.

[15] Kevin R Moore and Andrew Ning. "Distributed electric propulsion effects on existing aircraft through multidisciplinary optimization". In: *2018 AIAA/ASCE/AHS/ASC Structures, Structural Dynamics, and Materials Conference,* p. 1652, 2018.

[16] Michael D Patterson, Matthew J Daskilewicz and Brian J German. "Conceptual design of electric aircraft with distributed propellers: multidisciplinary analysis needs and aerodynamic modeling development". In: *52nd Aerospace sciences meeting,* p. 0534, 2014.

[17] Nikolai Herzog, Andreas Reeh, Andreas Kümmel and Christian Breitsamter. "Analysis of Distributed Electric Propulsion on Commuter Aircraft". In: *AIAA Scitech 2021 Forum,* p. 1199, 2021.

[18] Nicholas K Borer, Michael D Patterson, Jeffrey K Viken, Mark D Moore, Sean Clarke, Matthew E Redifer, Robert J Christie, Alex M Stoll, Arthur Dubois, JoeBen Bevirt, Andrew R Gibson, Trevor J Foster and Philip G Osterkamp. "Design and performance of the NASA SCEPTOR distributed electric propulsion flight demonstrator". In: *16th AIAA Aviation Technology, Integration, and Operations Conference,* p. 3920, 2016.

[19] Racheal M Erhard, Matthew A Clarke and Juan J Alonso. "A low-cost aero-propulsive analysis of distributed electric propulsion aircraft". In: *AIAA Scitech 2021 Forum,* p. 1200, 2021.

[20] Alessandro Bacchini, Enrico Cestino and Giulio Romeo. "A reduced order model to estimating propeller/wing interaction in solar powered aircraft preliminary design". In: *7th EASN international conference, Innovation in European Aeronautics Research,* 2017.

[21] Davide Montagnani, Matteo Tugnoli and Federico Fonte. DUST Theory Manual. Politecnico di Milano, 2020.

[22] Tomas Sinnige, Nando van Arnhem, Tom C A Stokkermans, Eitelberg Georg and Leo L M Veldhuis. "Wingtip-Mounted Propellers: Aerodynamic Analysis of Interaction Effects and Comparison with Conventional Layout". In: *Journal of Aircraft,* pp. 295-312, 2019.

[23] Nando van Arnhem, Sinnige Tomas, Tom C A Stokkermans, Georg Eitelberg and Leo L M Veldhuis. "Aerodynamic interaction effects of tip-mounted propellers installed on the horizontal tailplane". In: *2018 AIAA Aerospace Sciences Meeting,* p. 2052, 2018.

[24] Roger Willemsen. "A sensitivity study on the aerodynamic performance of a wingtip-mounted tractor propeller-wing system". MSc Thesis. Delft University of Technology, 2020.

[25] *A400M webpage.* URL: `https://www.airbus.com/en/products-services/defence/military-aircraft/a400m`.

[26] *UNIFIER19 webpage.* URL: `https://www.unifier19.eu/`.

[27] *Pipistrel AIrcraft webpage.* URL: https://www.pipistrel-aircraft.com/.

[28] UNIFIER19. *D2.2: Final concurrent design report.* 2021. URL: https://www.unifier19.eu/wp-content/uploads/2021/07/D2.2_Final_concurrent_design_report_Open.pdf.

[29] "A Framework for Hybrid-Electric". MSc Thesis. Politecnico di Milano, 2020.

[30] *OpenVSP API webpage.* URL: http://openvsp.org/api_docs/latest/.

Appendix A

Additional validation results

A.1. Considerations about the OpenVSP model

The experimental setup used by Sinnige, illustrated in Fig. A.1a, features a significantly large nacelle mounted on a relatively small wing.

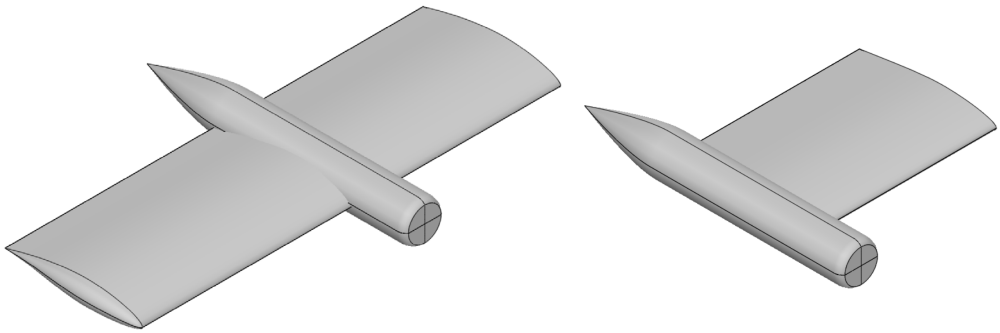

(a) Sinnige (b) Willemsen

Fig. A.1: OpenVSP model of Sinnige's and Willemsen's setups.

Many VLM procedures do not consider the nacelles at all. However, the contribution of such large objects may be relevant in terms of both drag and lift. In his MSc thesis [24], Willemsen quantified these contributions on a setup built using the same modular wing used by Sinnige and tested in the same wind tunnel. The assembly, represented in Fig. A.1b, consisted of a symmetric airfoil wing section possibly followed by the nacelle. The outboard wing part visible in Fig. A.1a was instead not present.

	$minC_D$ [–]	C_{L_α} [deg^{-1}]
Isolated Wing	0.0075	0.0524
Wing + Nacelle	0.0169	0.0720

Tab. A.1: Comparison of Willemsen's setups.

Tab. A.1 reports the minimum drag coefficient and the lift curve slope for both the setups considered by Willemsen, while Fig. A.2 shows the corresponding drag polars. The main effect of the nacelle is the increase of drag, well summarized by a $minC_D$ which is 125% higher than for the isolated wing. The large nacelle also produces a significant increment of the lift curve slope: +37.4%; this last aspect reflects in the concavity of the polars in Fig. A.2.

Despite Sinnige's reference surface being more than double Willemsen's one, the effects of the nacelle are still significant on the coefficients of the former. Considering these conclusions, all OpenVSP models included nacelles from the beginning.

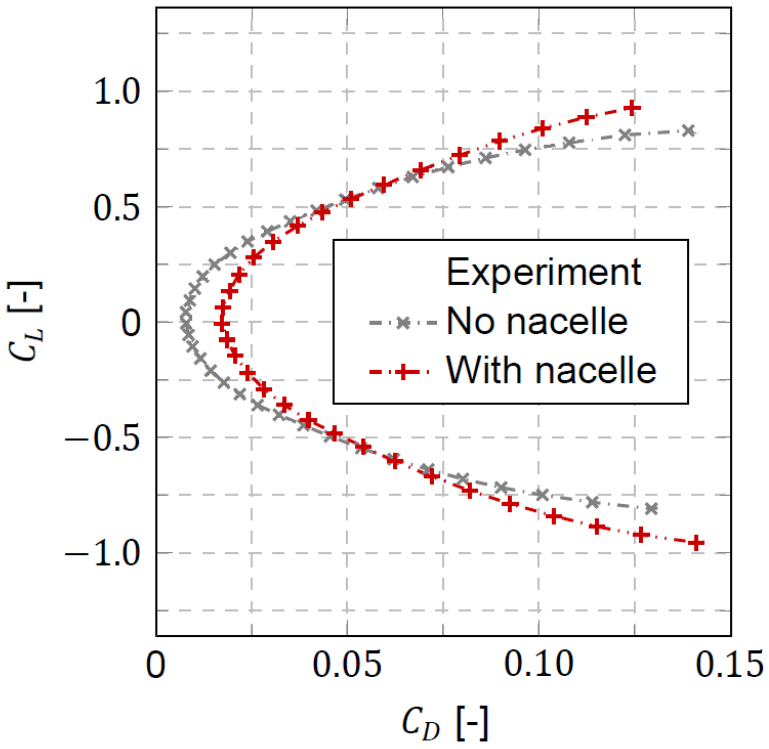

Fig. A.2: Drag polars of Willemsen's setups [24].

A.2. Dimensional polars

This section presents the dimensional forces acting on Sinnige's setup, measured or computed at different angles of attack, ranging from –6° to +8°. All the data refers to complete system forces, containing the contributions of the wing, the propeller, and the nacelle. VLM simulations use a full-span symmetric model of Sinnige's setup. On the other hand, experimental data, measured on the half-span wing, need to be multiplied by 2. Patterson's increments, computed for a single propeller and multiplied by 2, are added to the full-span wing experimental data.

The significant discrepancies between experimental and numerical polars at $J = 0.7$, visible in Fig. A.6, are directly related to those between experimental and numerical thrust. The proper data reduction, illustrated in Section 2.2.4, allows mitigating these deviations, which are no longer present in the curves presented in Section 2.2.5.

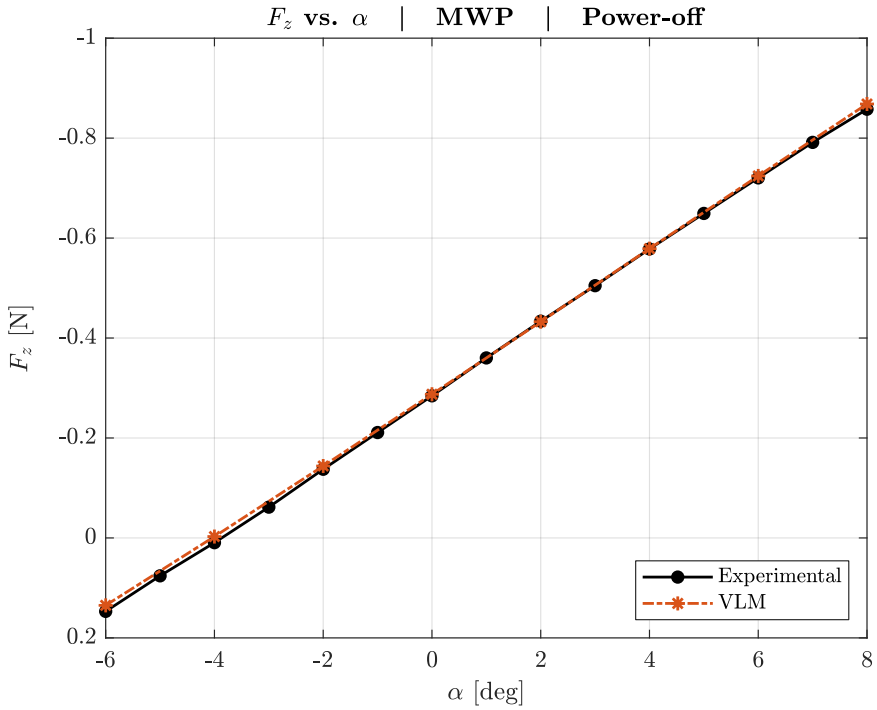

Fig. A.3: Experimental and numerical dimensional lift polars (prop-off).

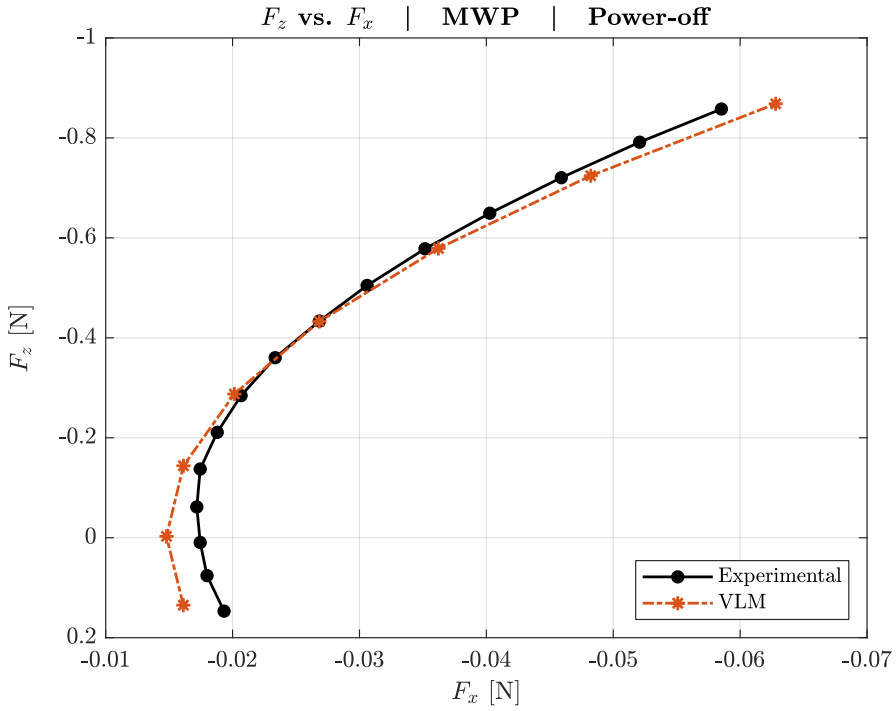

Fig. A.4: Experimental and numerical dimensional drag polars (prop-off).

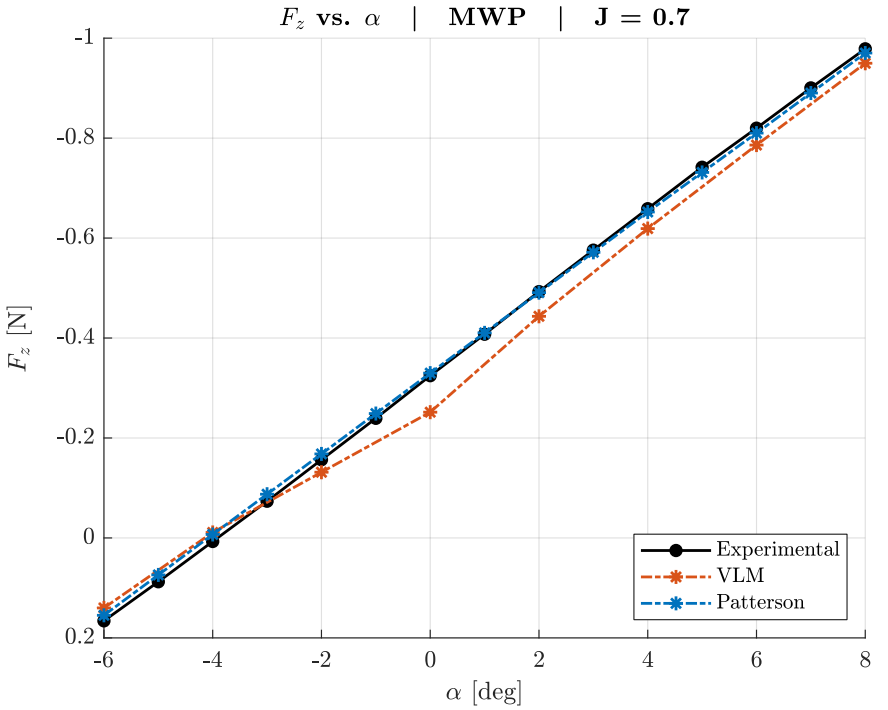

Fig. A.5: Experimental and numerical dimensional lift polars ($J = 0.7$).

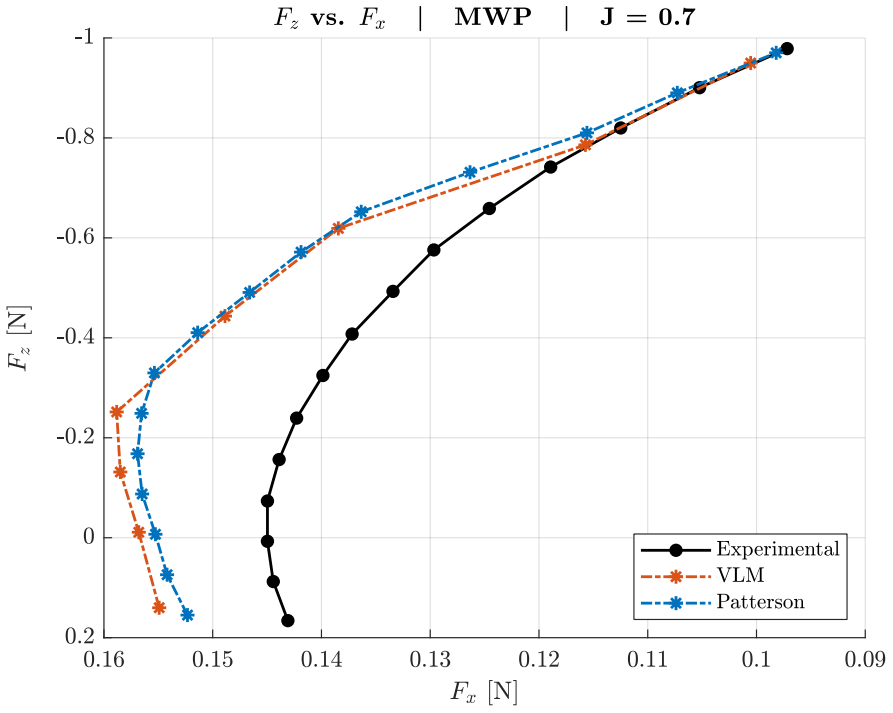

Fig. A.6: Experimental and numerical dimensional drag polars ($J = 0.7$).

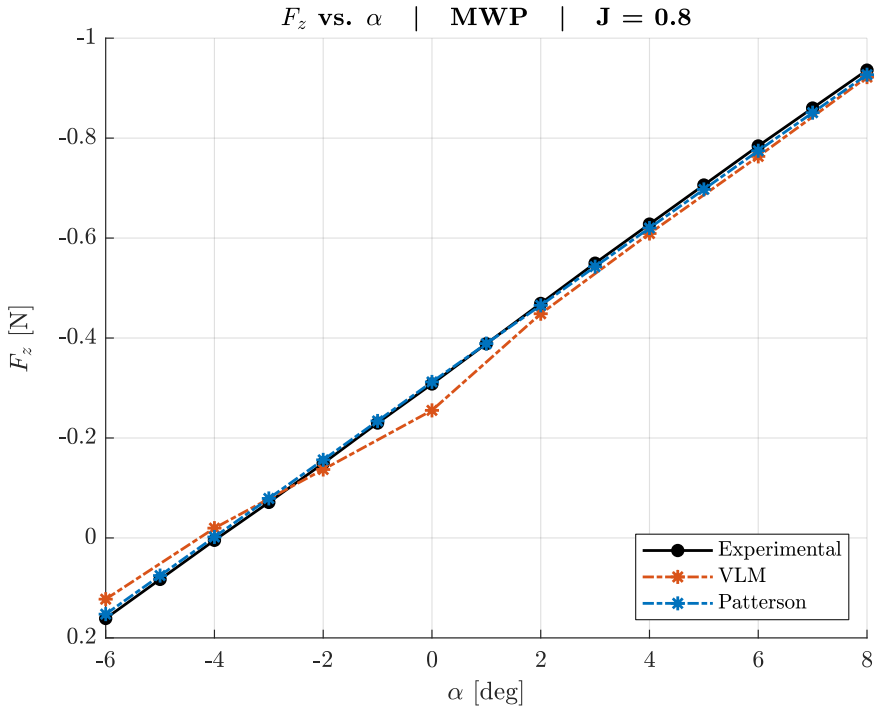

Fig. A.7: Experimental and numerical dimensional lift polars ($J = 0.8$).

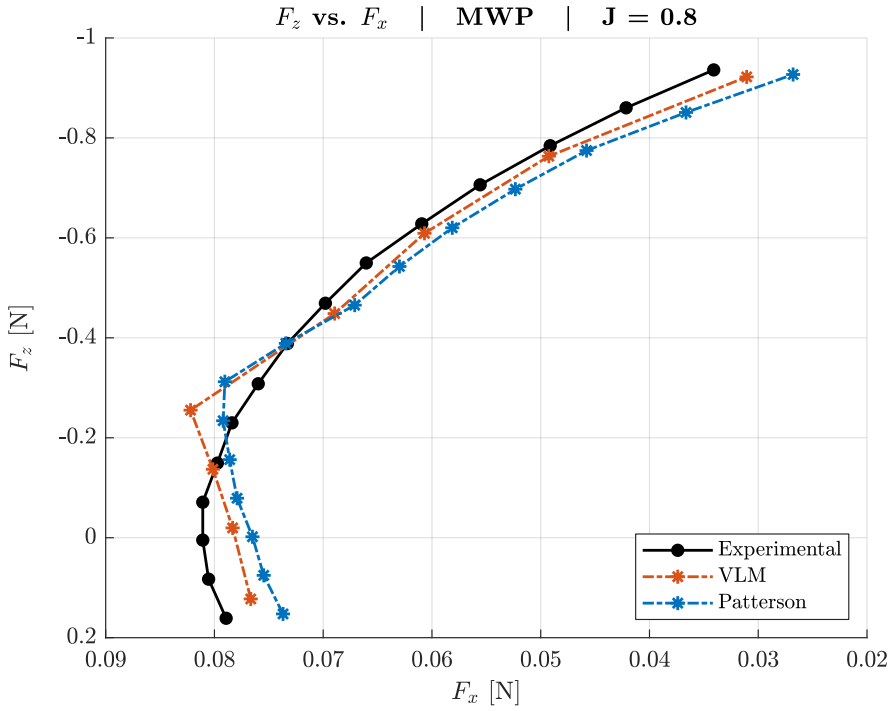

Fig. A.8: Experimental and numerical dimensional drag polars ($J = 0.8$).

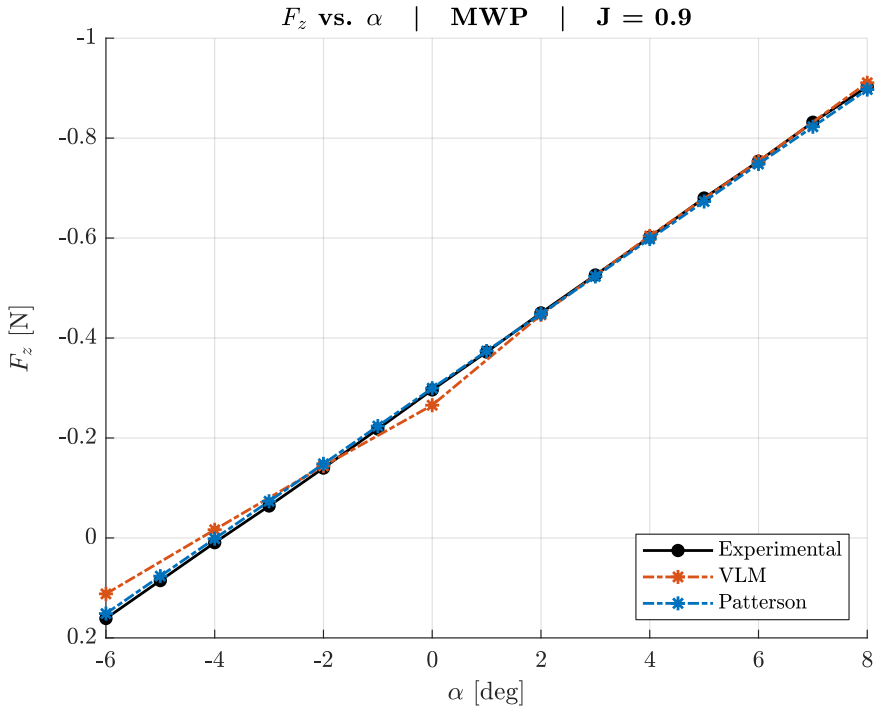

Fig. A.9: Experimental and numerical dimensional lift polars ($J = 0.9$).

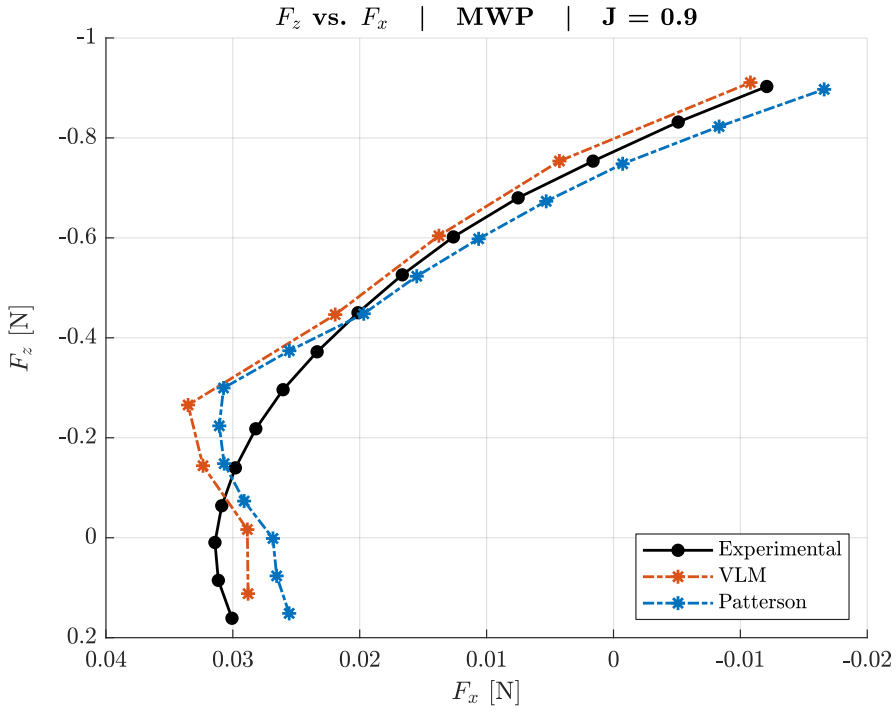

Fig. A.10: Experimental and numerical dimensional drag polars ($J = 0.9$).

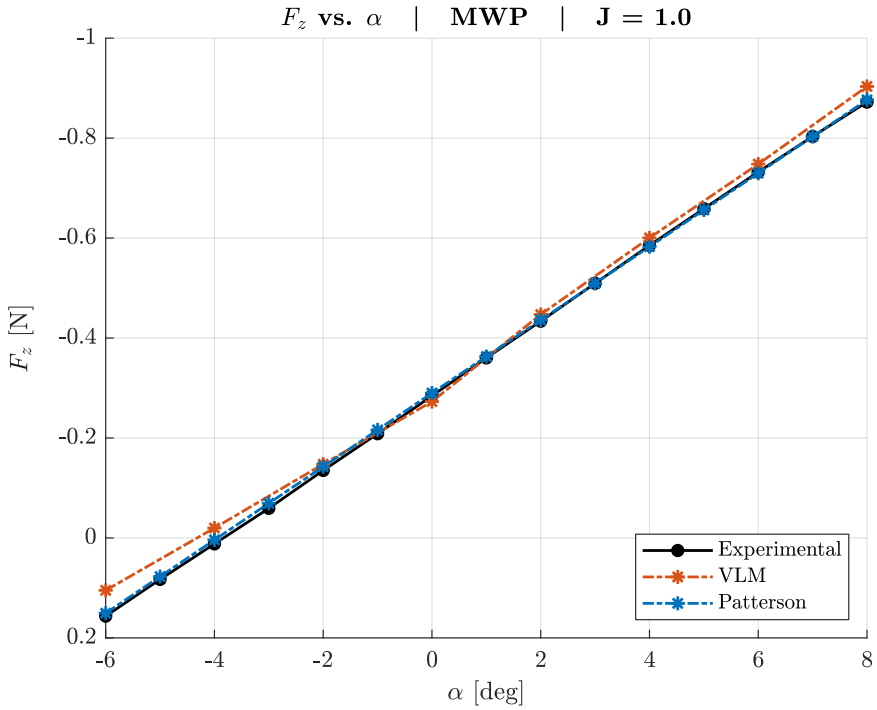

Fig. A.11: Experimental and numerical dimensional lift polars ($J = 1.0$).

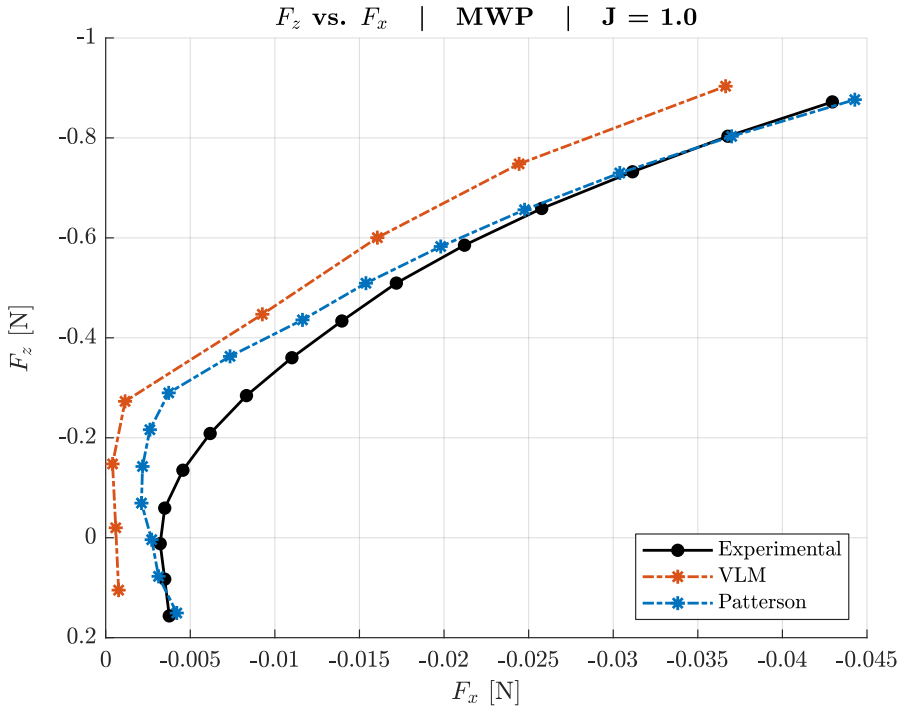

Fig. A.12: Experimental and numerical dimensional drag polars ($J = 1.0$).

Appendix B

Multiple Propeller Case

B.1. Models for coefficients deviations

Section 3.1.2 identified some models for the relative deviations of the lift and drag coefficients produced by the propellers blowing the wing. Section 3.1.3 recomputed the parameters of these models to provide the variations with respect to the unblown wing polars. It is worth recalling that all the curves used in the derivation were analytic. The following equations report their expressions:

$$C_L = C_{L_\alpha}(\alpha - \alpha_0) \tag{B.1}$$

$$C_D = minC_D + K\left(C_L - C_{L_{minC_D}}\right)^2 \tag{B.2}$$

Moreover, being identified using only the discrepancies at positive angles of attack, the presented models are valid on a limited portion of the AoA range. This fact, however, does not represent a significant limit since the wing airfoils rarely operate at a negative α.

For the lift coefficient increment, the selected model is a zero-degree polynomial, i.e., a constant value. The following paragraphs try to justify this choice starting from the analytic expression of the lift relative increment shown by the equation below:

$$\Delta C_L = \frac{C_{L_2} - C_{L_1}}{\left|C_{L_1}\right|} = \frac{C_{L_{\alpha_2}}(\alpha - \alpha_{0_2}) - C_{L_{\alpha_1}}(\alpha - \alpha_{0_1})}{\left|C_{L_{\alpha_1}}(\alpha - \alpha_{0_1})\right|} \tag{B.3}$$

The next equation is the simplified form of Eq. (B.3), obtained by rearranging it and considering that the zero-lift AoA deviation is almost negligible in the multiple propeller case. The resulting equation is a piecewise constant function of α.

$$\Delta C_L \cong \frac{(C_{L_{\alpha_2}} - C_{L_{\alpha_1}})(\alpha - \alpha_0)}{\left|C_{L_{\alpha_1}}(\alpha - \alpha_0)\right|} = \begin{cases} k & for\ \alpha > \alpha_0 \\ -k & for\ \alpha < \alpha_0 \end{cases} \tag{B.4}$$

The plots of Fig. B.1 graphically illustrate step-by-step the concepts described above. Fig. B.1a shows two analytic lift polars: C_{L_1} and C_{L_2}, with the former representing the reference one. The difference between the two incident straight lines, represented by the yellow curve in Fig. B.1b, is also linear. Since the zero-lift AoA is the same for both curves, also the lift deviation intersects

the zero-lift axis in α_0. Dividing $C_{L_1} - C_{L_2}$ by the absolute value of C_{L_1} the result is the already described piecewise constant function, represented in Fig. B.1c.

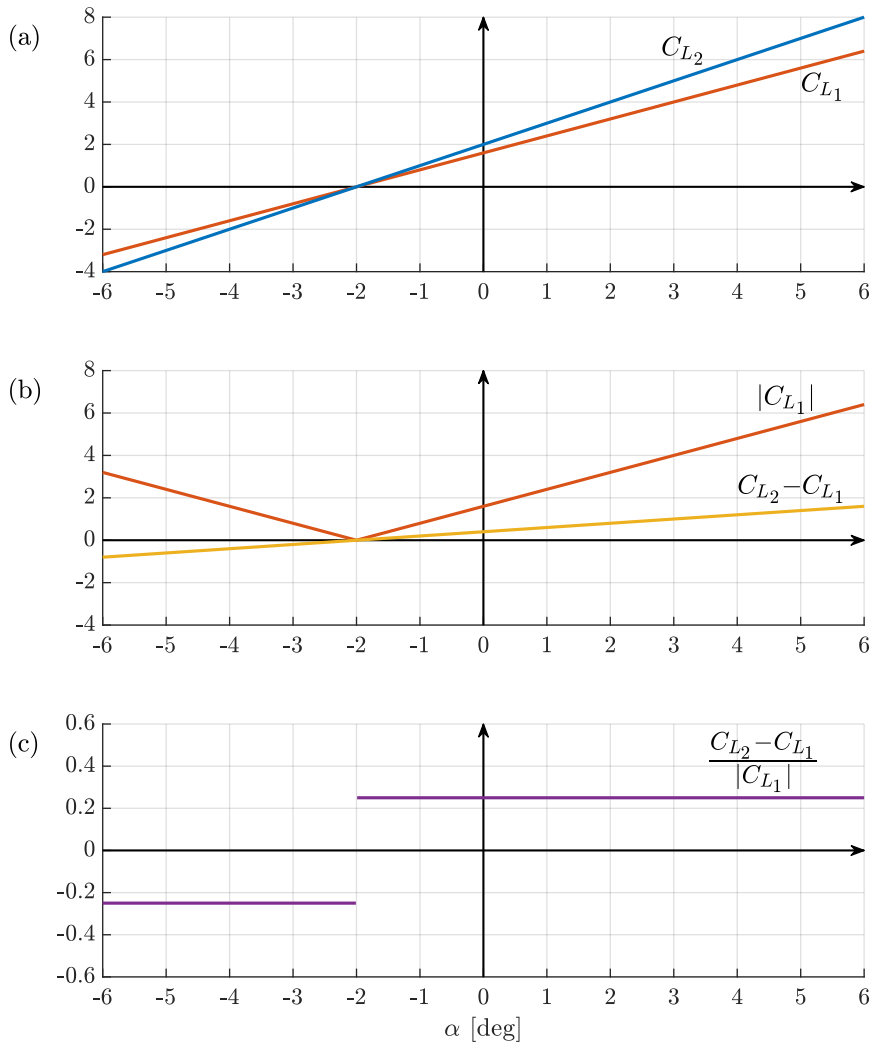

Fig. B.1: Simplified model for the relative deviation of the lift coefficient.

Although this is only an ideal scenario, since the assumptions formulated above are not far from the truth, a zero-degree polynomial is sufficient to approximate the relative lift increment in the range of positive angles of attack.

Concerning the drag coefficient increment, the selected model is a second-degree polynomial, i.e., a quadratic function of α. The following equation is the analytic expression of the drag relative increment obtained applying its formula:

$$\Delta C_D = \frac{C_{D_2} - C_{D_1}}{C_{D_1}} = k \frac{\alpha^2 + n_1\alpha + n_0}{\alpha^2 + m_1\alpha + m_0} \tag{B.5}$$

the absolute value operator at the denominator is unnecessary since the drag coefficient is positive by definition.

Even exploiting the simplification of the multiple propeller case, i.e., considering negligible both the minimum drag and concavity variations, it is

not possible to obtain any significantly simpler form of the rational function of Eq. (B.5).

The plots of Fig. B.2 graphically illustrate step-by-step the computation of the relative increment that led to the selected quadratic model. Fig. B.2a shows two analytic drag polars: C_{D_1} and C_{D_2}, with the former representing the reference one. The difference between the two parabolas, despite being linear with C_L thanks to the assumptions of negligible K and $minC_D$ variations, is quadratic with α, as shown by Fig. B.2b. The resulting drag relative increment, already expressed by Eq. (B.5), is finally depicted in Fig. B.2c.

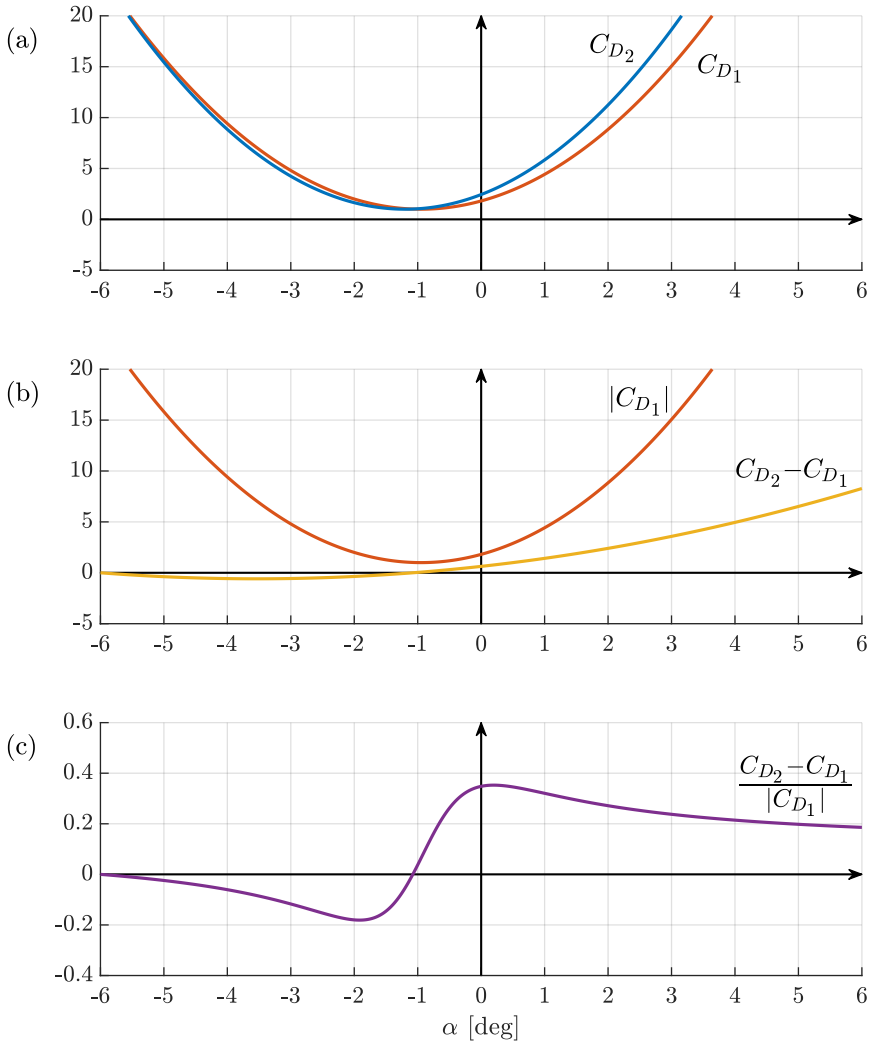

Fig. B.2: Simplified model for the relative deviation of the drag coefficient.

The actual behavior of the relative increment of the drag coefficient depends on the exact values of the parameters of the polars. The curve shown in Fig. B.2c does not resemble the deviations observed on the multiple propeller setup. In that case, the function was smoother, i.e., monotonic and without any concavity change, at least for the positive angles of attack. A simple quadratic model was then sufficient to approximate the drag relative increment.

Appendix C

Numerical campaign

C.1. Reduced approach raw data

The meta-model dataset, generated through the numerical campaign presented in Section 5.1.2, consists of 216 data points arranged in 36 sets of polars, one for each of the four layouts of the nine cases listed in Tab. 5.2. The present section shows the collected data in their raw form; 3 out of the 36 polars exhibit some kind of issue, visible in Fig. C.2, Fig. C.8, and Fig. C.9. Section 5.1.3 illustrates the procedure applied to deal with the corrupted data points.

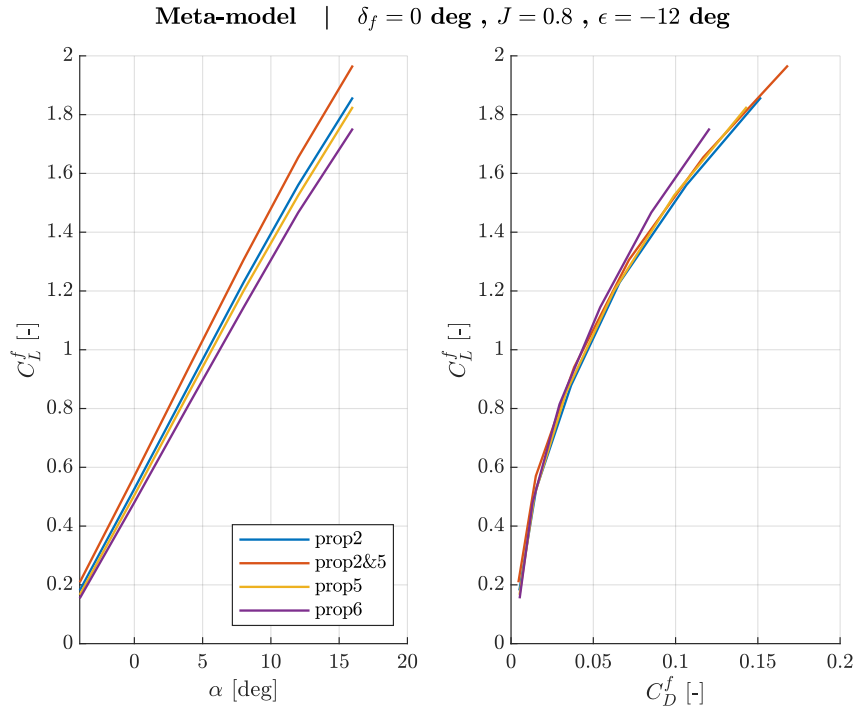

Fig. C.1: Numerical campaign raw polars ($\epsilon = -12°$, $J = 0.8$, $\delta_f = 0°$).

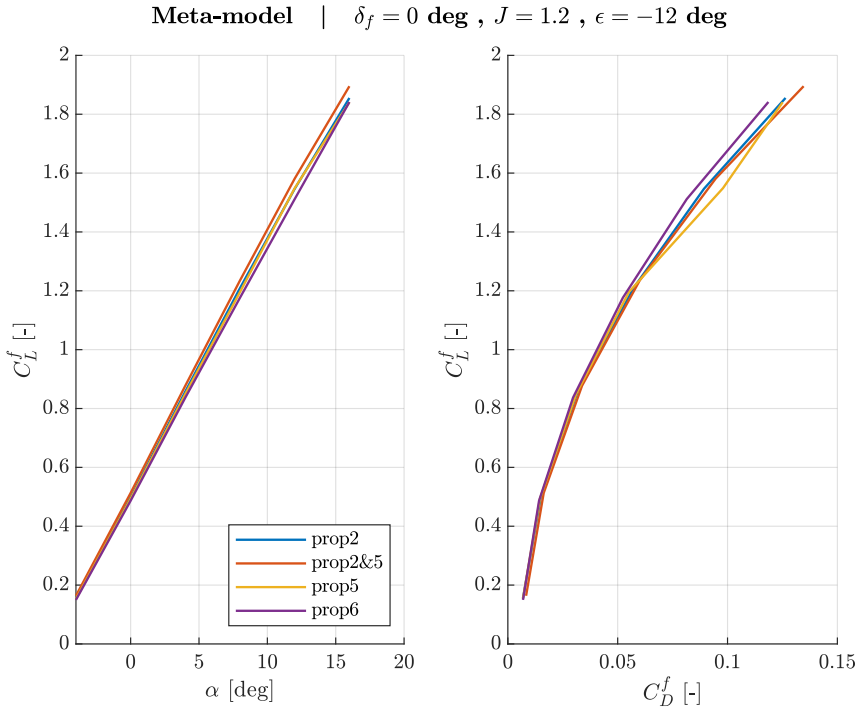

Fig. C.2: Numerical campaign raw polars ($\epsilon = -12°$, $J = 1.2$, $\delta_f = 0°$).

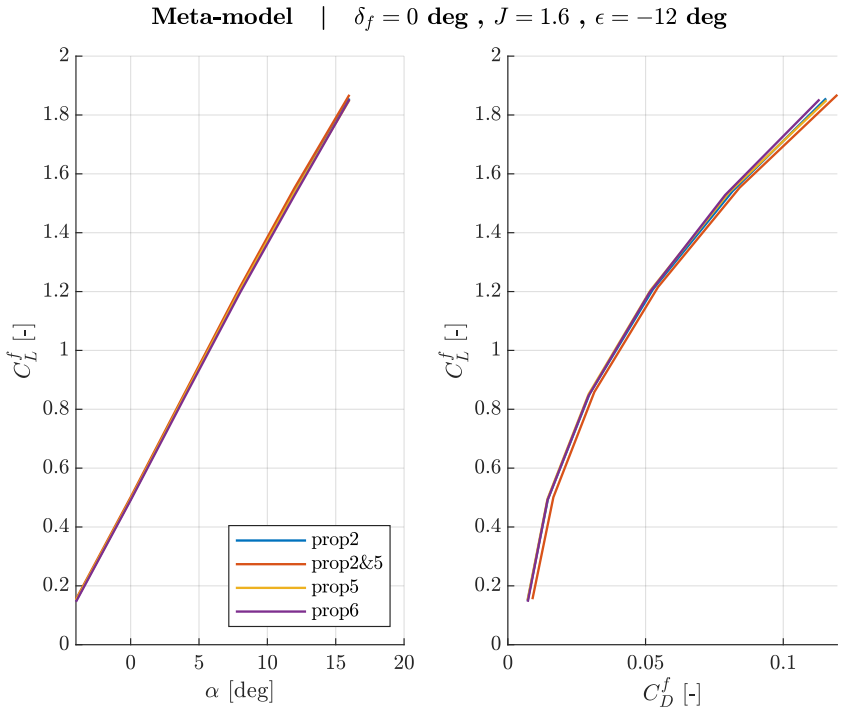

Fig. C.3: Numerical campaign raw polars ($\epsilon = -12°$, $J = 1.6$, $\delta_f = 0°$).

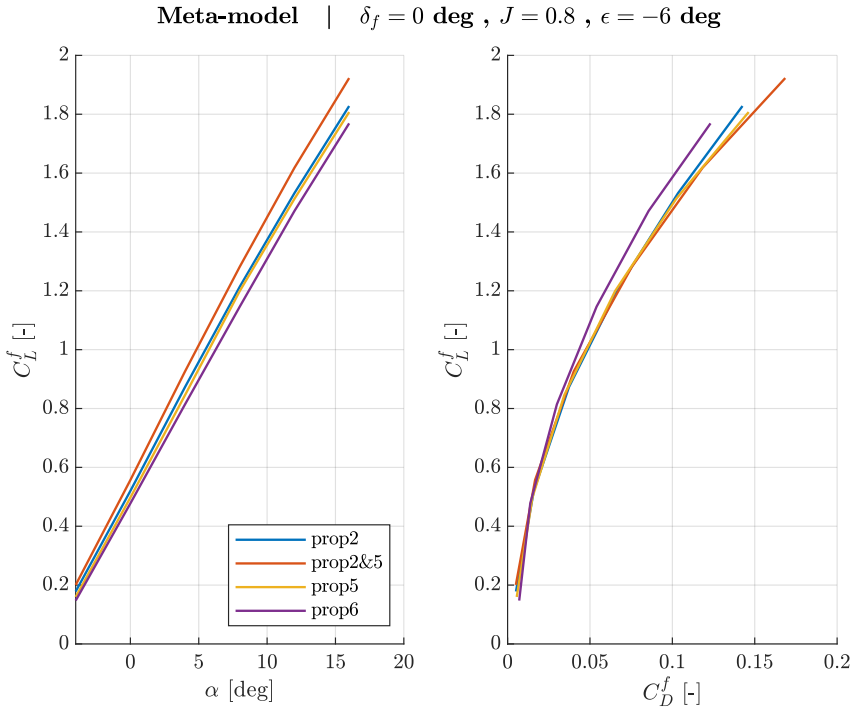

Fig. C.4: Numerical campaign raw polars ($\epsilon = -6°$, $J = 0.8$, $\delta_f = 0°$).

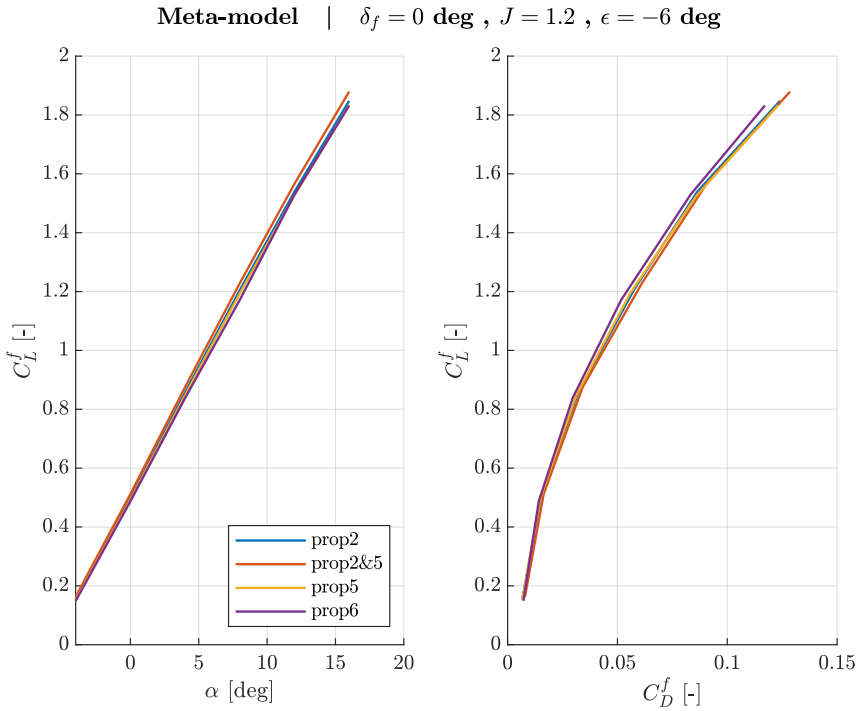

Fig. C.5: Numerical campaign raw polars ($\epsilon = -6°$, $J = 1.2$, $\delta_f = 0°$).

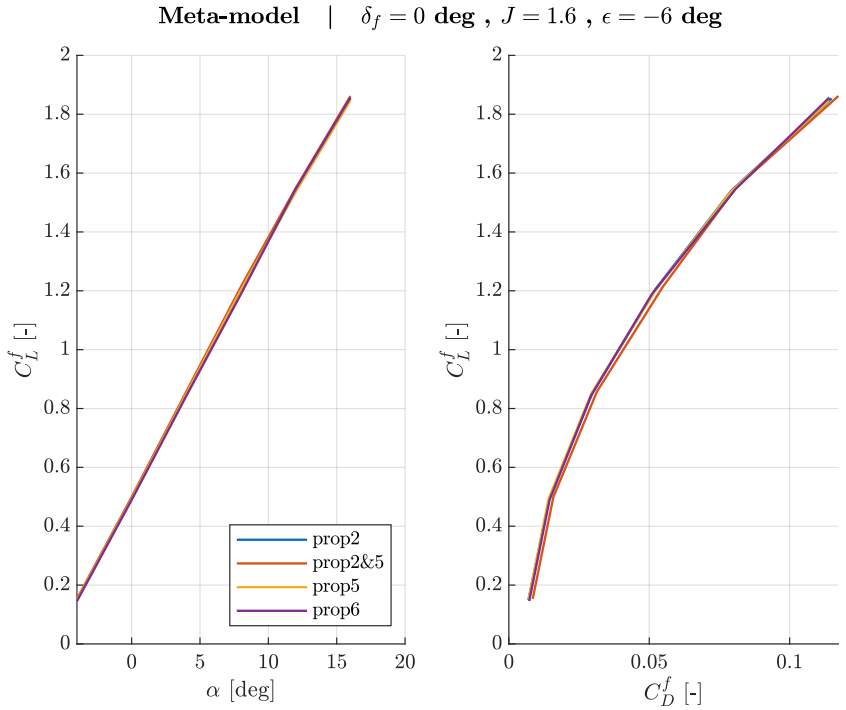

Fig. C.6: Numerical campaign raw polars ($\epsilon = -6°$, $J = 1.6$, $\delta_f = 0°$).

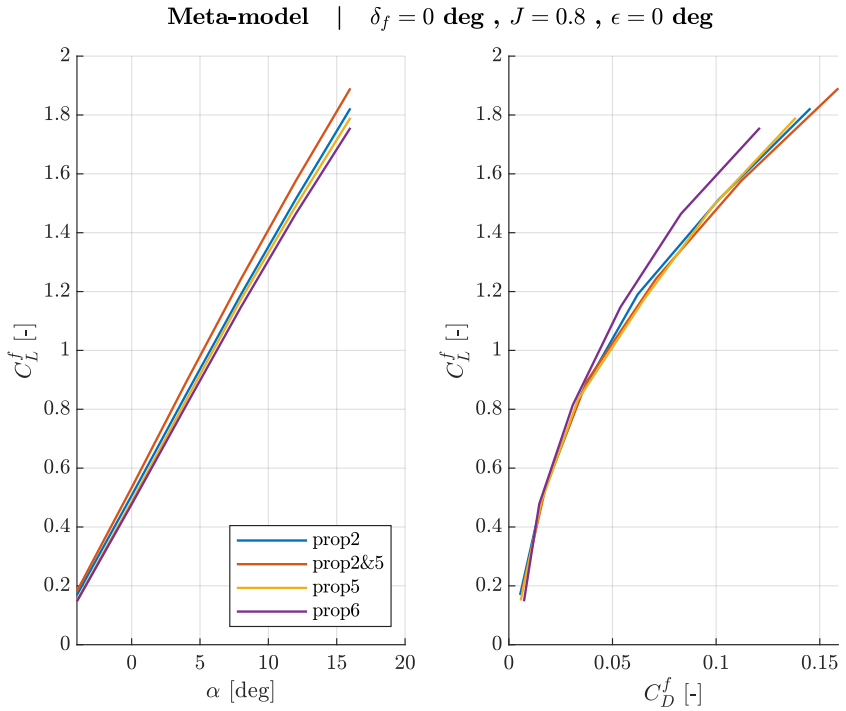

Fig. C.7: Numerical campaign raw polars ($\epsilon = 0°$, $J = 0.8$, $\delta_f = 0°$).

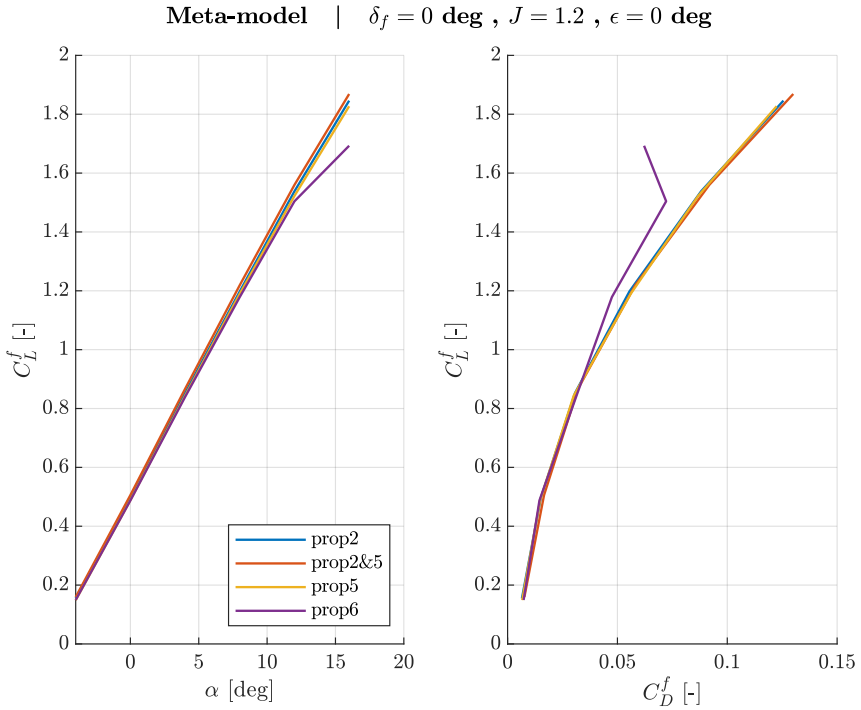

Fig. C.8: Numerical campaign raw polars ($\epsilon = 0°$, $J = 1.2$, $\delta_f = 0°$).

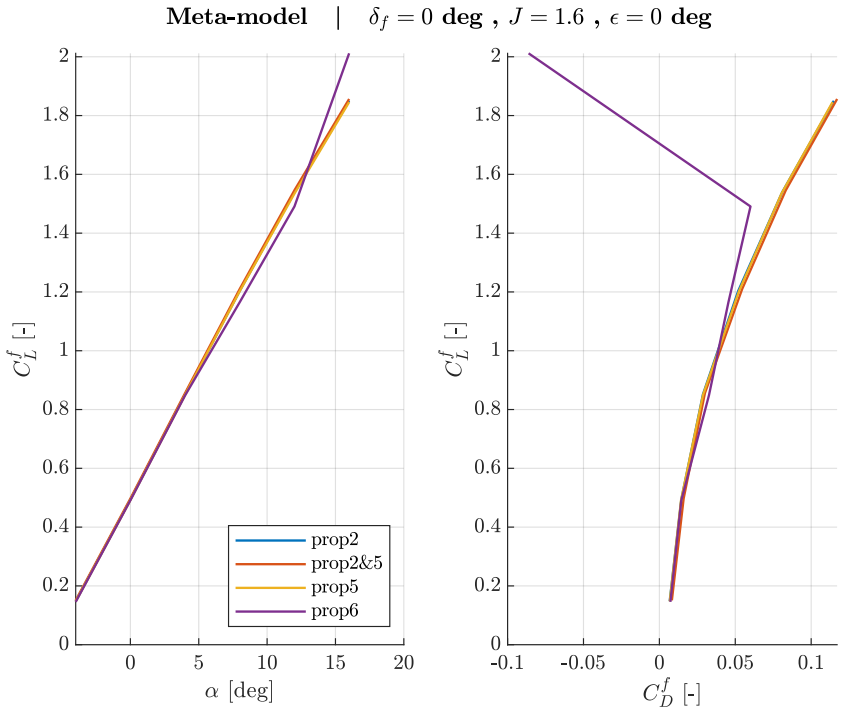

Fig. C.9: Numerical campaign raw polars ($\epsilon = 0°$, $J = 1.6$, $\delta_f = 0°$).